High Resolution Spectroscopy of Open Shell Clusters

A thesis submitted for the degree of Doctor of Philosophy at the University of Oxford

by

Christopher Roger Dennis

Jesus College

Trinity Term 1997

Abstract

High Resolution Spectroscopy of Open-Shell Clusters

A thesis submitted for the degree of Doctor of Philosophy at the University of Oxford

Christopher Roger Dennis
Jesus College
Trinity Term, 1997

The microwave spectrum of the open-shell van der Waals complex NO-HF has been recorded in the region 6-20GHz using a pulsed nozzle Fourier transform microwave spectrometer. This is the first observation of the microwave spectrum of a open-shell van der Waals complex between two molecules. The spectrum exhibits a rich hyperfine structure with the observation of intermolecular hyperfine interactions in an isolated system providing a sensitive probe of electron transfer in the complex.

The spectrum consists of four fine structure transitions $\frac{5}{2}$(e)$-\frac{3}{2}$(e), $\frac{3}{2}$(e)$-\frac{1}{2}$(e), $\frac{5}{2}$(f)$-\frac{3}{2}$(f), $\frac{3}{2}$(f)$-\frac{1}{2}$(f) which have been fitted to a semi-rigid Hamiltonian developed to include the effects of the orbital and spin angular momenta of the unpaired electron on NO. A new treatment to account for the intermolecular hyperfine interaction was developed. The structure of the complex has been determined and is significantly bent with an angle of between 37° and 49° between the NO internuclear axis and the a-axis of the complex. The Renner-Teller parameter, ϵ_2, is very large and negative having the value of -10 449.32(4)GHz indicating that configuration with the unpaired electron in the plane of the complex is more stable.

The analysis of the hyperfine interactions of the hydrogen and fluorine nuclei uses two constants for each nucleus, one for the spatial relationship between the magnetic moments of the unpaired electron and the nuclear magnetic moment and a Fermi-contact term.

The Fermi-contact term for hydrogen is the first strong evidence of intermolecular charge transfer in an isolated van der Waals molecule.

Acknowledgements

My biggest thanks must go to Dr Brian Howard who has supported me throughout my work in Oxford. His boundless enthusiasm for everything motivates us all. Dr Chris Whitham for helping to teach me the spectrometer and providing an experienced person to talk to when I needed it. Kevin Valentine for the various improved electronic circuits that he built for the spectrometer.

The many people that have passed through the group while I have been in the PTCL, for making the lab an interesting and stimulating place to work. Particular mention must go to Matthew Brookes, Russell Low and never forgetting Danny Hughes.

My parents for helping me through many years at school and university. They encouraged me into chemistry and have understood when I haven't phoned home for a while. My sisters for being there when I need them.

I must thank my friends Meirion, Steve, James and Bryan for making the time outside the lab most interesting. Meirion particularly for sharing a flat with me for two years and putting up with my music filtered through the floor. Finally Oxford University Cycling Club for showing me more of the surrounding countryside and teaching me the pleasures of riding time trials.

Contents

1 Introduction **1**
1.1 Introduction . . . 1
1.1.1 Microwave Spectroscopy . . . 3
1.1.2 Infrared Spectroscopy . . . 4
1.1.3 Electronic Spectroscopy . . . 4
1.2 Open Shell Complexes . . . 6

2 Experimental **11**
2.1 Introduction . . . 11
2.2 Fabry-Perot Cavity . . . 13
2.2.1 Q-Factor . . . 16
2.3 Supersonic Expansions . . . 17
2.4 Antennas . . . 20
2.4.1 Coaxial Aerial . . . 20
2.4.2 Gordon Coupler . . . 21
2.5 Line Shapes . . . 22
2.6 Interaction of radiation with matter . . . 24
2.7 Sensitivity . . . 26
2.8 Microwave Circuits . . . 27
2.8.1 18-26GHz Homodyne Microwave Circuit . . . 27
2.8.2 Heterodyne Detection Circuit . . . 28
2.8.3 27.5 MHz Heterodyne Detection Circuit . . . 30
2.9 Timing . . . 35
2.10 Data Collection . . . 39
2.11 Signal Processing . . . 39
2.12 Automation . . . 41
2.13 Helmholtz Coils . . . 42
2.14 Double Resonance . . . 44
2.15 Vacuum system . . . 46

3 Fine Structure Hamiltonian **51**
3.1 Introduction . . . 51
3.2 Basis Set . . . 53

3.2.1 Symmetry with respect to space fixed inversion . . . 55
3.3 The Molecular Hamiltonian . . . 57
3.4 Rotational Hamiltonian . . . 57
3.5 Spin-Orbit Hamiltonian . . . 59
3.6 Quenching . . . 59
3.7 Terms Off-Diagonal in Orbital Angular Momentum . . . 61
3.8 The Fine Structure Matrix . . . 62

4 Hyperfine Interactions **67**
4.1 Nitrogen Magnetic Hyperfine . . . 68
4.1.1 Nuclear Spin-Orbit Interaction . . . 71
4.2 Fermi Contact Interaction . . . 72
4.3 Spin-Spin Dipolar Interaction . . . 72
4.4 The Electric Quadrupole Interaction. . . . 74
4.5 Hydrogen and Fluorine Hyperfine . . . 78
4.5.1 Hydrogen Coupling . . . 79
4.5.2 Fluorine Coupling . . . 80
4.6 Magnetic hyperfine parameters for hydrogen and fluorine . . . 80
4.7 Nuclear Spin-Spin Interaction . . . 84

5 Results **88**
5.1 Introduction . . . 88
5.2 Experimental . . . 90
5.3 Results . . . 90
5.3.1 12GHz; J=$\frac{3}{2}$(f)-$\frac{1}{2}$(f) Transitions . . . 93
5.3.2 7GHz; J=$\frac{3}{2}$(e)-$\frac{1}{2}$(e) and 14GHz; J=$\frac{5}{2}$(e)-$\frac{3}{2}$(e) Transitions . . . 101
5.3.3 18.9GHz; J=$\frac{5}{2}$(f)-$\frac{3}{2}$(f) Transitions . . . 105
5.4 Independent Hyperfine Fitting . . . 105
5.5 Parallel and Perpendicular Components . . . 115
5.6 The unusual energy level pattern of the $\frac{1}{2}$(e) State . . . 116
5.7 The Least Squares Fitting Program . . . 118
5.8 Results of the Least Squares Fitting . . . 120
5.8.1 Angular Fitting . . . 122
5.9 Discussion of Fitted Constants . . . 123
5.9.1 Fine Structure . . . 123
5.9.2 Hyperfine Constants . . . 127
5.10 Charge Transfer Effects . . . 131
5.11 Ab-Initio . . . 133
5.12 Conclusion . . . 137

A Fine Structure Matrix Elements **140**
A.1 Rotational and Spin-Orbit Hamiltonian . . . 141
A.1.1 Diagonal in Electronic State . . . 141
A.1.2 Off-Diagonal in Electronic State . . . 142

B Hyperfine Matrix Elements **143**
B.1 Magnetic Hyperfine 143
B.2 Electric Quadrupole 145
B.3 Matrix Elements for Hydrogen and Fluorine 146
B.3.1 $q_2 = 0$, $\delta_{\Lambda,\Lambda'}$ 146
B.3.2 $q_2 = 0$, $\delta_{\Lambda,\Lambda'\pm 2}$ 147
B.3.3 Perpendicular 148
B.3.4 $q_2 = \pm 2$ 149

C Standard Angular Momentum Transformations **150**
C.0.5 Dot Product 150
C.1 Wigner-Eckart Theorem 150

D The Microwave Spectrum of NO-HF **151**
D.1 f-states 151
D.2 e-states 155
D.3 Infrared Spectra 159

E Ar-OCS **160**

Chapter 1

Introduction

"The time has come," the Walrus said.
"to talk of many things."
-L. Carroll

1.1 Introduction

A van der Waals cluster is a small aggregation of at least two atoms or molecules held together by intermolecular forces, often referred to as a van der Waals complex. The forces which hold the clusters together are much smaller than those of a conventional chemical bond The binding energies reflect this being approximately 1% of a chemical bonding energy or about kT at room temperature, and can vary from 7.1cm^{-1} in Ne-HF[1] to 1062cm^{-1} in $(HF)_2$.[2, 3]

Van der Waals complexes are of great interest because they provide an intimate probe of intermolecular forces, an understanding of this is vital in many areas of physics and chemistry, for example, the bulk properties of matter, colloidal properties, surface binding, and the tertiary structure of proteins.[4] The effects of intermolecular forces can be observed in measurements of macroscopic physical properties like the temperature dependence of the second viral coefficient of gases.[5] These forces control the course of chemical reactions and there is interest in creating van der Waals complexes of reactive partners in the hope that they will exhibit a bound state on the reaction coordinate.[6]

The forces which generate van der Waals complexes are weak so at ambient temperatures there will only be very small concentrations of complexes. It is thus necessary to operate at a reduced temperature to achieve the requisite numbers of complexes for spectroscopy. This is achieved either by directly cooling a bulk sample of gas, or using a pulsed or continuous supersonic expansion.

The bulk method was first used for observing van der Waals molecules by Welsh et al[7, 8] when seeking evidence of complex formation via changes in collision induced broadening. They saw sharp lines and concluded that these were spectra of $(H_2)_2$. The bulk method requires a large sample of gas through which the incident radiation is passed many times achieving path lengths of between 20 and 200 m[9] because of the small concentrations of complexes present.

A supersonic nozzle uses a small orifice and allows a gas mixture to expand through that orifice into an evacuated chamber. In a pulsed supersonic nozzle a simple solenoid arrangement controls the flow by sealing and unsealing the orifice with a teflon poppet. The expansion acts to cool the molecules and promote complex formation. The compression of the Boltzmann distribution into a smaller number of states implies increased sensitivity as well as the reduction of spectral congestion facilitating assignment. It is capable of achieving very low effective temperature and has become ubiquitous in physical chemistry. It offers many possibilities that are not available to bulk methods, for example, slit nozzles, electric discharges, photolysis and gas mixing arrangements.

Bulk sample methods are good for taking spectra of very weakly bound complexes and at higher temperatures than supersonic expansions allowing the measurement of higher rotational levels. Bulk samples are disadvantaged by the fact that to form complexes relatively higher pressures are used than in a jet and the higher temperature can render the spectra congested and difficult to analyze. In supersonic expansions the fact that the gas is expanding into a vacuum allows the attainment of very low background pressures and hence little pressure broadening. The ability to achieve very low temperatures can be a disadvantage when it quenches features of the spectrum. The two methods can complement one another very effectively, for example, when a bulk spectrum is too complex to assign the simpler spectrum from a supersonic expansion may provide the necessary data to assign the bulk spectrum.

A gamut of spectroscopic techniques are available for the analysis of the properties of complexes which provide varied information on physical properties of complexes.

1.1.1 Microwave Spectroscopy

The first microwave technique extensively applied to the spectroscopy of van der Waals complexes was molecular beam electric resonance(MBERS).[10, 11] Rabi spectroscopy in which a beam of molecules is passed through an inhomogeneous electric field, a region of microwave radiation, and another inhomogeneous electric field. The electric fields deflect the course of molecules in states which exhibit a Stark effect. There is a stop wire which prevents molecules which are undeflected from reaching the detector. There are two modes of operation, one in which the two electric fields are identical but opposite and molecules in a particular state are focussed onto the detector. If microwave radiation induces a transition the second field does not focus the molecules onto the detector and there is a decrease in the observed flux of molecules. Alternatively the fields are different and the microwave radiation causes the molecules to move into the state that is focussed by the second field so that an increase in signal is observed.

The frequency range in which the spectrometers can operate is broad, starting at radio frequencies and extending far into the microwave. Good product selection is guaranteed because the molecules are usually detected by a mass spectrometer . The exciting radiation field applied can be broad banded allowing rapid scanning for transitions. However the system will only work if molecules have an electric dipole moment and states with the correct field dependence. The spectrometer can be used to determine the magnitudes of electric dipole moments.

This technique has been almost completely superseded by pulsed nozzle, Fourier transform microwave spectroscopy(FTMW),[12, 13] even though it has a number of advantages. In FTMW a pulse of gas mixture is expanded into a resonant cavity to which is applied a pulse of microwave radiation exciting the molecules within the system coherently. The decay of the macroscopic electric dipole thus created is then detected, and subsequently Fourier transformed to give a frequency spectrum. FTMW is a high resolution and sensitive technique permitting easy observation of magnetic hyperfine and electric quadrupole effects within complexes.[14] The major weakness is that because a resonant cavity is used it has an inherently narrow bandwidth and

searching for signals of new species is a laborious process. It is still unable to match MBERS in the frequency range that it is able to cover mainly being used only in the range 6-26GHz with up to 40GHz possible with some systems.

1.1.2 Infrared Spectroscopy

Infrared spectroscopy[15] is a probe of the rovibrational modes of a complex. It is applicable to most classes of complexes because a majority of molecules have at least one infrared active vibrational mode. The frequency region around an infrared active mode of one of the monomers is examined because the frequency of the monomer mode is slightly shifted on complexation.

A popular source of radiation is typically a diode laser which is a liquid helium or nitrogen cooled solid state device that produces tunable infrared radiation over a narrow range necessitating several diodes to cover different monomer modes. The diodes can be used with bulk samples and pinhole or slit supersonic nozzles. Other sources include colour centre lasers or difference frequency generation. Detection is by another liquid nitrogen cooled solid state device which produces a signal proportional to the incident radiation.

Experiments have been carried out in the far infrared(FIR) which probe the van der Waals mode of a complex directly revealing the subtle features of van der Waals forces, for example, the Π and the Σ bends of Ar-HCl have been observed.[16] The major difficulty is the generation of the far infrared radiation by complex schemes utilising the mixing of the output of a FIR laser with microwave radiation to create sidebands.

Infrared spectroscopy determines the vibrational and rotational constants of the complexes and if predissociation is seen then the binding energy of the complexes can be calculated. It is restricted by the low sensitivity requiring long paths to achieve sufficient absorption and it is not capable of resolving the finest features of the spectra such as hyperfine effects.

1.1.3 Electronic Spectroscopy

There is a variety of methods used to determine the electronic structures of complexes. Electronic spectroscopy is characterised by its high sensitvity because detectors, e.g. photomultiplier

tubes, exist that can count single photons. Generally it is not possible to resolve features in the spectra due to hyperfine effects. A problem for smaller van der Waals complexes is the lack of a strong chromophore so electronic spectroscopy is often applied to complexes with aromatic molecules, although the first complexes whose electronic spectra were measured were those involving iodine and rare gases.[17]

In laser induced fluorescence(LIF) a laser is used to excite the molecules via a strongly allowed electronic transition into an excited electronic state. The molecules in this state can decay via internal conversion and intersystem crossing into other states and emit radiation by fluorescence. The emitted radiation is collected perpendicular to the exciting beam and is dispersed to give a spectrum. An alternative is to measure the fluorescence as the exciting frequency is swept to find the positions of energy levels in absorption. The resultant spectrum contains information on both the rotational and vibrational modes of the complex. Complexes that have been studied in this way include Ar-OH/D[18, 19]

In resonance enhanced multiphoton ionisation(REMPI) laser radiation is incident with a beam of molecules in an interaction region. The absorption of two or more photons causes ionisation. The ions generated are accelerated away by an electric field and the number of ions incident on a detector are measured. If a time of flight tube is used then mass selection is possible. The laser frequency is swept and when there is a coincidence between the frequency of the light and the energy of a state that lies in between the ground state and ionisation there is an increase in the ion signal. The spectrum thus obtained can resolve vibrational and rotational features in the spectrum. This method is used mainly on complexes of aromatic molecules[20, 21]

Finally there is ZEKE spectroscopy where the electrons are excited by ultraviolet radiation to a point just below the ionisation threshold. Such states are referred to as Rydberg states. The molecules can then be ionised by the application of an electric field and the electron count can be measured. The main area of application is again the aromatic complexes[22, 23]

1.2 Open Shell Complexes

Interest in open-shell complexes, where one of the species has an unpaired electron, has increased in recent years because the spectra of such species are more difficult to analyze but yield more information about the nature of the interactions within a complex. They offer the opportunity to observe interactions that lie part way between the purely physical forces in closed shell complexes and a full chemical bond, e.g. $(NO)_2$ which shows a pairing of the lone electrons on each of the NO moieties.[24–29] The radical components usually possess orbital and spin angular momenta, with partial quenching of the orbital motion. The electron orbital and spin angular momenta can couple to nuclear spins to give magnetic hyperfine and electric quadrupole effects.

Open-shell species have a tendency to be very reactive with very short lifetimes. There are are some stable radicals(O_2, NO_2, and NO) and they are all being studied in a variety of complexes. Previously they have been avoided because of the difficulties involved in the analysis. Now complexes of the stable radicals provide a testing ground for the development of the analytical methods which can then be extended to the less stable radicals. The reactive species can be generated in a number of ways but for the study of van der Waals complexes of open-shell species two methods are used, pulsed nozzle electric discharge[30, 31] and photolysis.[32–35] In the pulsed nozzle electric discharge a pair of electrodes are constructed into the orifice of the nozzle, separated by an insulator. A high electric potential is applied to the electrodes so that when gas from the pulse passes between them an electric discharge is set up which ionizes species in the expansion creating radicals. For photolysis a laser beam is passed either just over the front of the pulsed nozzle aperture or through a storage region behind the pulse nozzle causing ionization and fragmentation in the sample which is quenched during the expansion to generate complexes.

The first truly open-shell complex to be studied in detail was Ar-NO[36–39] using MBERS with resolution of the hyperfine structure of the nitrogen nucleus in NO. The analysis presented many problems at the time because nothing like it had been seen before. The rationalization of the structure of the spectrum was an important step in understanding the rotational spectra of complexes involving $^2\Pi$ states. Subsequently other complexes of similar electronic structure have been studied most particularly the hydroxyl and SH radical rare gas complexes,

Ar-OH/D,[18, 40, 40–44] Kr-OH/D,[45] Ne-OH,[46, 47] Ar-SH.[48–50] Most of these studies use electronic spectroscopy which does not reveal as much about the interactions within the complexes as microwave spectroscopy.

Other types of complex that have been studied are those of oxygen which has a $^3\Sigma_g^-$ ground state. The spectrum of the Ar-O_2[51–53] complex has been observed in the infrared and is very different from the spectrum of pure O_2. The changes in the spectra are attributed to partial quenching of the free rotations of the O_2 by the anisotropic intermolecular potential function. The $(O_2)_2$ complex has also been observed[54] although the rotational structure of the infrared bands was not resolved. Recently other oxygen complexes have been studied including O_2-N_2O,[55] O_2-OCS[56] and SO_2-O_2[57] although only O_2-N_2O is analysed.

The final category of open-shell complexes are the rare gas NO_2 where the rare gas is argon, krypton[58, 59] or xenon.[60] The microwave spectra here resolve the hyperfine splittings where a large Fermi contact interaction is seen coupling the electron spin to the nuclear spin before coupling to the rotational angular momentum. The rare gas nucleus sits above the plane of the NO_2 between the two oxygen atoms.

References

[1] C. M. Lovejoy, D. J. Nesbitt. *J. Chem. Phys.*, **94**, 208, (1991).

[2] D. C. Dayton, K. W. Jucks, R. E. Miller. *J. Chem. Phys.*, **90**, 2631, (1989).

[3] E. J. Bohac, M. D. Marshall, R. E. Miller. *J. Chem. Phys.*, **96**, 6681, (1992).

[4] G. C. Maitland, M. Rigby, E. B. Smith, W. A. Wakeham. *Intermolecular Forces*. Clarendon Press, Oxford, (1981).

[5] R. J. Le Roy, J. S. Carley. *Adv. Chem. Phys.*, **42**, 353, (1980).

[6] J. Z. Gillies, C. W. Gillies, R. D. Suenram, F. J. Lovas. *J. Am. Chem. Soc.*, **110**, 7991, (1988).

[7] A. Watanabe, H. L. Welsh. *Phys. Rev. Lett.*, **13**, 810, (1964).

[8] A. Kudian, H. L. Welsh, A. Watanabe. *J. Chem. Phys.*, **42**, 3397, (1965).

[9] A. R. W. McKellar. *Faraday Discuss.*, **97**, 69, (1994).

[10] C. H. Townes, A. L. Schawlow. *Microwave Spectroscopy*. McGraw-Hill, New York, (1955).

[11] N. F. Ramsey. *Molecular Beams*. Oxford University Press, New York, (1985).

[12] T. J. Balle, W. H. Flygare. *Rev. Sci. Instrum.*, **52**, 33, (1981).

[13] E. J. Campbell, L. W. Buxton, T. J. Balle, W. H. Flygare. *J. Chem. Phys.*, **74**, 813, (1981).

[14] A. Bauder. *J. Mol. Struct.*, **108**, 33, (1997).

[15] D. J. Nesbitt. *Chem. Rev.*, **88**, 843, (1988).

[16] K. L. Busarow, G. A. Blake, K. B. Laughlin, R. C. Cohen, Y. T. Lee, R. J. Saykally. *J. Chem. Phys.*, **89**, 1268, (1988).

[17] D. H. Levy, ed. R. G. Wolley. *Quantum Dynamics of Molecules*. Plenum Press, New York, (1980).

[18] B. Chang, L. Yu, D. Cullin, B. Rehfuss, J. Williamson, T. A. Miller, W. M. Fawzy, X. Zheng, S. Fei, M. Heaven. *J. Chem. Phys.*, **95**, 7087, (1991).

[19] M. I. Lester, S. E. Choi, L. C. Giancarlo, R. W. Randall. *Faraday Discus.*, **97**, 21, (1994).

[20] S. Kendler, Y. Haas. *J. Phys. Chem. A*, **101**, 2578, (1997).

[21] R. A. Weersink, S. C. Wallace. *J. Phys. Chem.*, **98**, 10710, (1994).

[22] J. G. Jäckel, R. Schmid, H. Jones, T. Nakanaga. *Chem. Phys.*, **215**, 291, (1997).

[23] O. Dopfer, M. Melf, K. Müller-Dethlefs. *Chem. Phys.*, **207**, 437, (1996).

[24] C. M. Western, P. R. R. Landridge-Smith, B. J. Howard, S. E. Novick. *Mol. Phys.*, **44**, 145, (1981).

[25] P. Brechignac, S. D. Benedictus, N. Halberstadt, B. J. Whitaker, S. Arriller. *J. Chem. Phys.*, **83**, 2064, (1985).

[26] S. G. Kukolich. *J. Am. Chem. Soc.*, **104**, 4715, (1982).

[27] M. P. Casassa, J. C. Stephenson, D. S. King. *J. Chem. Phys*, **85**, 2333, (1986).

[28] M. P. Casassa, A. M. Woodward, J. C. Stephenson, D. S. King. *J. Chem. Phys*, **85**, 6235, (1986).

[29] Y. Matsumoto, Y. Oshima, M Takami. *J. Chem. Phys.*, **92**, 6235, (1986).

[30] Y. Endo, H. Kohguih, Y. Oshima. *Faraday Discuss.*, **97**, 341, (1994).

[31] Y. Oshima, M. Iida, Y. Endo. *J. Chem. Phys.*, **95**, 7001, (1995).

[32] K. Lui, R. G. MacDonald, A. F. Wagner. *Int. Rev. Phys. Chem.*, **9**, 187, (1990).

[33] A. M. Ellis, E. S. J. Robles, T. A. Miller. *J. Chem. Phys.*, **97**, 5809, (1993).

[34] M. T. Berry, M. R. Brustein, M. I. Lester. *J. Chem. Phys.*, **90**, 5878, (1989).

[35] S. Fei, X. Zheng, M. C. Heaven. *J. Chem. Phys.*, **89**, 1655, (1988).

[36] P. D. A. Mills, C. M. Western, B. J. Howard. *J. Phys. Chem.*, **90**, 2991, (1986).

[37] J. C. Miller, W. C. Cheng. *J. Phys. Chem.*, **89**, 1647, (1985).

[38] K. Sato, Y. Achiba, H. Nakamura, K. Kimura. *J. Chem. Phys.*, **85**, 4951, (1986).

[39] J. C. Miller. *J. Chem. Phys.*, **90**, 4031, (1989).

[40] M. T. Berry, M. R. Brustein, M. I. Lester, C. Chakravarty, D. C. Clary. *Chem. Phys. Lett.*, **178**, 301, (1991).

[41] B. C. Chang, L. Yu, D. Cullin, B. Rehfusss, J. Williamson. *J. Chem. Phys.*, **95**, 7086, (1991).

[42] W. M. Fawzy, M. C. Heaven. *J. Chem. Phys.*, **89**, 7030, (1988).

[43] S. K. Kularni, Y. Lin, M. C. Heaven. *Chem. Phys. Lett.*, **95**, 597, (1990).

[44] Y. Oshima, M. Iida, Y. Endo. *J. Chem. Phys.*, **95**, 7001, (1990).

[45] S. Fei, X. Zheng, M. C. Heaven. *J. Chem. Phys.*, **97**, 1655, (1992).

[46] B. Chang, J. R. Dunlop, T. A. Miller. *Chem. Phys. Lett.*, **207**, 55, (1993).

[47] B. Chang, J. R. Dunlop, J. M. Williamson, T. A. Miller, M. C. Heaven. *Chem. Phys. Lett.*, **207**, 62, (1993).

[48] M. Yang, A. P. Salzberg, B. Chang, C. C. Carter, T. A. Miller. *J. Chem. Phys.*, **98**, 4301, (1993).

[49] C. C. Carter, T. A. Miller. *J. Chem. Phys.*, **107**, 3447, (1997).

[50] M. C. Yang, C. C. Carter, T. A. Miller. *J. Chem. Phys.*, **107**, 3437, (1997).

[51] G. Henderson, G. E. Ewing. *J. Chem. Phys.*, **59**, 2280, (1973).

[52] J. Tennyson, J. Mettes. *Chem. Phys.*, **76**, 195, (1983).

[53] A. Van der Avoird. *J. Chem. Phys.*, **79**, 1170, (1983).

[54] C. A. Long, G. E. Ewing. *J. Chem. Phys.*, **58**, 4824, (1973).

[55] H. Qian, D. Seccombe, B. J. Howard. *J. Chem. Phys.*, **107**, 7658, (1997).

[56] S. Blake. *Part II Thesis*. Oxford University, (1995).

[57] A. R. Hight-Walker, G. T. Fraser, J. T. Hougen, C. Lugez, R. D. Suenram. *Electron-spin and tunneling effects in the microwave spectrum of SO_2-O_2*. 52nd Ohio State University International Symposium on Molecular Spectroscopy, (1997).

[58] R. J. Low, C. J. Whitham, T. D. Varberg, B. J. Howard. *Chem. Phys. Lett.*, **222**, 443, (1994).

[59] R. J. Low. *D.Phil. Thesis*. Oxford University, (1995).

[60] C. J. Whitham. *Private Communication*. (1997).

Chapter 2

Experimental

Dans les champs de l'observation le hasard
ne favorise que les esprits préparés.

Where observation is concerned chance
favours only the prepared mind.
Louis Pasteur

2.1 Introduction

The technique of pulsed nozzle Fourier transform microwave spectroscopy(FTMW) was developed by Flygare[1] and coworkers in the late seventies specifically as a method for investigating the rotational spectra of weakly bound complexes.

The method makes a clear departure from previous microwave techniques because it uses a gas expansion into a resonant cavity compared to static gas samples contained in a section of waveguide. The Fourier transform microwave method has a number of advantages over a waveguide procedure in that it is able to sample a band of frequencies of width 1-2MHz in one spectrum. It has low Doppler broadening improving resolution and effective complex formation enhancing sensitivity because of the properties of expansions from pulsed nozzles. High electromagnetic fields can also be achieved within the spectrometer because of the use of a resonant Fabry-Perot cavity.

The microwave spectrometer used in Oxford is basically the same as that designed by Flygare except where enhancements have been made to take advantage of improvements in technology[2–9]

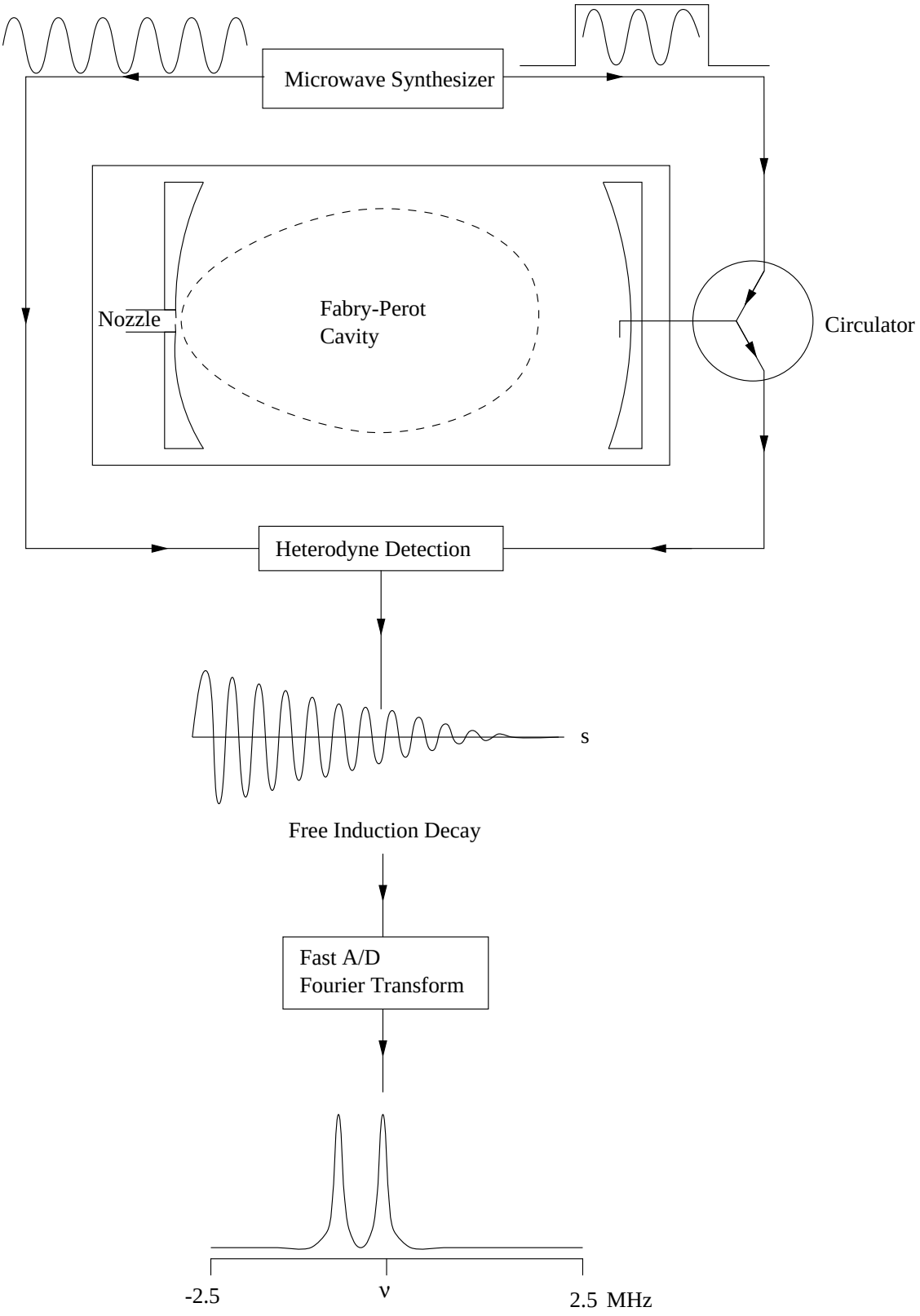

Figure 2.1: A schematic diagram of the Fourier transform microwave spectrometer showing its basic components and operations.

including computation and automation.

A simplified diagram of the spectrometer is shown in Figure 2.1. The basic chain of events in the spectrometer is initiated by the opening of the pulsed nozzle for approximately 500μs allowing gas to expand into a vacuum chamber between a pair of large mirrors. A microwave pulse of width 1-2μs is applied between these mirrors, timed to maximise interaction with the molecules in the expansion. After a short delay to allow the exciting radiation to die away, the emission from the molecules excited by the applied radiation is detected and digitized by a fast A/D card in a computer. The free induction decay thus recorded can be Fourier transformed to give a spectrum. The free induction decay can be taken many times over and added together to allow weak signals to be observed. The nozzle is only opened on alternate cycles so that the spectra in the absence of gas may be subtracted to remove any characteristic absorption of the cavity or microwave circuit.

In this chapter the component parts which together comprise the spectrometer will be described.

2.2 Fabry-Perot Cavity

A fundamental part of the spectrometer is the Fabry-Perot cavity which consists of a pair of spherical aluminium mirrors, radius of curvature 70cm, in a near confocal arrangement. The properties of a system of this type are a capacity for high energy storage at specific frequencies and a spatial characteristic which proves beneficial to spectroscopy. These properties have been investigated[10–12] for several different mirror configurations including circular and rectangular plane mirrors with a view to possible applications in masers. These studies concluded that the Fabry-Perot cavity is characterised by a discrete set of normal modes. The dominant mode has a field intensity which falls to low values at the edges of the mirror.

The stable modes of the resonator can be approximately expressed as a series of Hermite-Gaussian polynomials, which are denoted by TEM_{mnq} where m and n indicate the order of the Hermite polynomials and q is the number of half wavelengths between the reflectors. The linear polarization patterns for the lowest order TEM modes illustrating the position of the field nodes

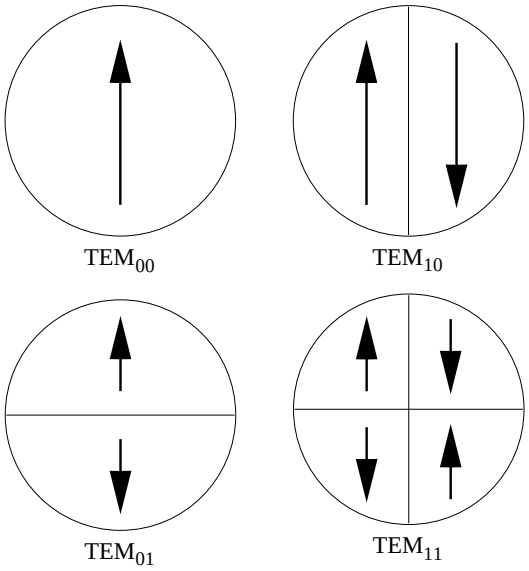

Figure 2.2: Schematic linear polarisation and field node patterns for the lowest order TEM modes of a Fabry-Perot Cavity

are shown in Figure 2.2. A mode can in part be characterised by the beam waist, which is the point at which the field intensity falls to $\frac{1}{e}$ of the equivalent axial value, see Figure 2.3. For the gas expansion, the beam waist excludes molecules which have a high velocity component perpendicular to the axis of the cavity from interaction with radiation.

The resonant frequencies of the cavity are given by the equation

$$\nu_0 = \frac{c}{2d}\left(q + \frac{1}{\pi}(m+n+1)\cos^{-1}\left(1-\frac{d}{R}\right)\right) \tag{2.1}$$

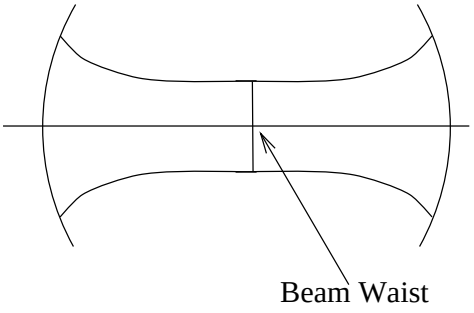

Figure 2.3: Illustration of the cavity-beam waist

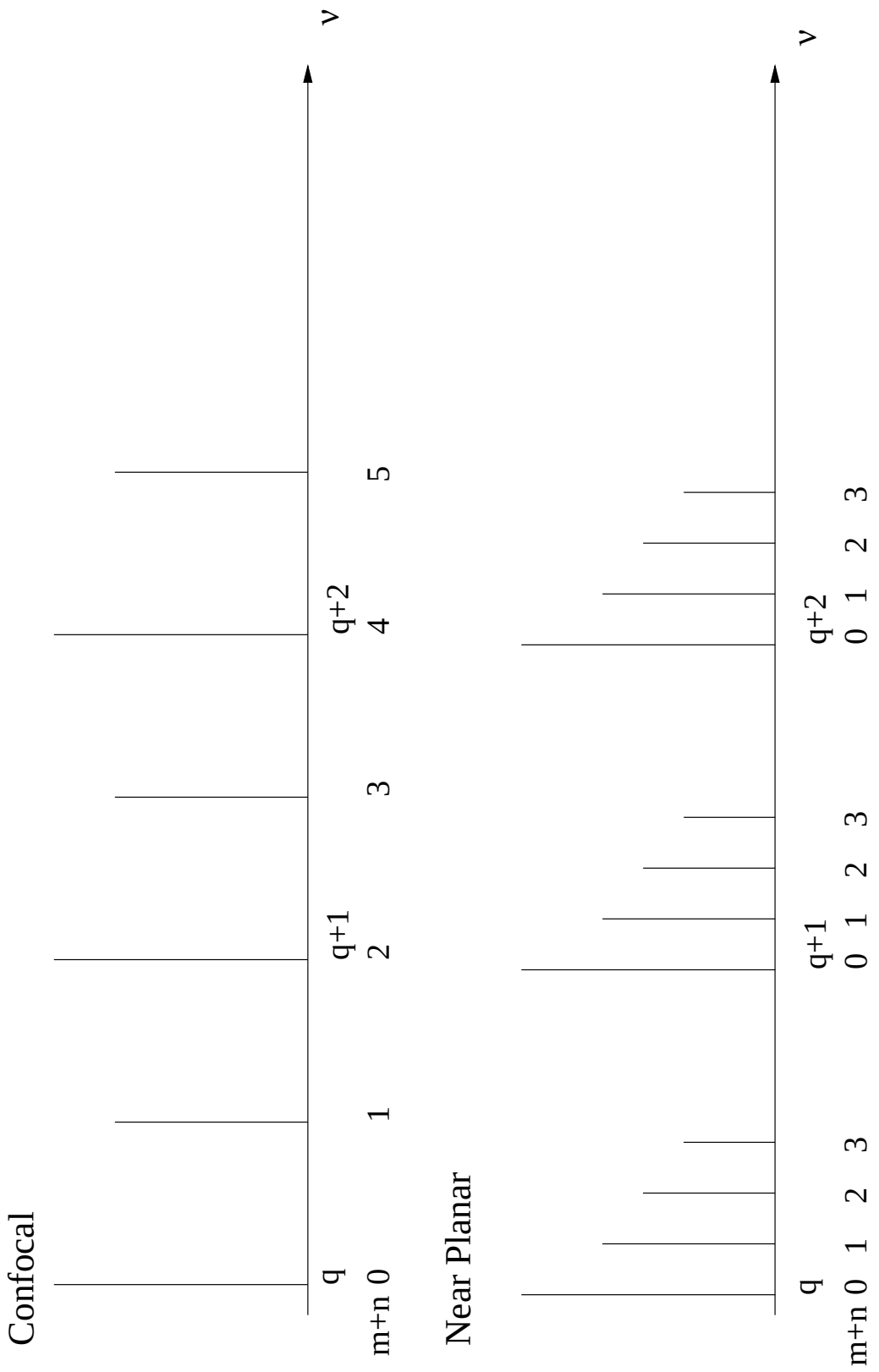

Figure 2.4: Distributions of resonant frequencies in a Fabry-Perot cavity for confocal and near planar($R \gg d$) arrangements of mirrors

for a system with mirrors of equal radius of curvature, R, and separation, d, which for a confocal system of radius 50cm gives

$$\nu_0 = \frac{c}{2d}\left(q + \frac{1}{2}(m+n+1)\right) \tag{2.2}$$

There are thus a series of modes separated by $\frac{c}{2d}$ for q and $\frac{c}{4d}$ for m and n. For any given higher resonance there will be a number of permutations of m,n and q which can form that frequency. We require that m and n are zero to give the maximum field density along the axis of the cavity where the expansion of molecules will be. The fundamental mode has the smallest spot size on the mirror, and thus the lowest diffractive losses for finite sized mirrors. It is also possible to use an annulus of microwave absorbent foam[13] on the mirror to suppress the higher order modes.

By going to a near confocal system $d \approx 60$cm and $R = 50$cm the non-fundamental modes separate from the fundamental modes to allow the selection of the fundamental TEM_{00} mode.

$$\nu_0 = \frac{c}{2d}\big(q + 0.564(m+n+1)\big) \tag{2.3}$$

The fundamental will be separated from the basic mode by approximately 140MHz. An example of the distribution of the modes by frequency is given in Figure 2.4

2.2.1 Q-Factor

The effectiveness of the cavity in storing energy can be quantified in a term known as the Q(quality) factor, which is

$$Q = \omega\left(\frac{\text{energy stored}}{\text{energy lost per cycle}}\right) \tag{2.4}$$

where ω is 2π. Q is shown to be related to the energy loss of the system which can occur by two different methods.

- The diffractive loss due to radiation spilling over the edges of the mirror, which has been shown to be lowest for the fundamental mode and minimized further by the use of a confocal mirror system.[10–12]

- The reflective loss due to imperfections in the surface of the mirror and penetration into the surface of the mirror.

If we consider only the loss due to surface effects and expression for Q is obtained.

$$Q = \frac{d}{2\delta} \tag{2.5}$$

where d is the separation between the mirrors and δ is the skin depth, which is the distance below the surface of the mirror travelled by the radiation at which the amplitude of the radiation has fallen to $\frac{1}{e}$ of its value at the surface.

Q can also be related to the width of the cavity resonance(full width at half maximum), $\Delta\nu_{\frac{1}{2}}$,

$$\Delta\nu_{\frac{1}{2}} = \frac{\nu}{Q} = \frac{1}{2\pi\tau_c} \tag{2.6}$$

where τ_c is the time constant for the cavity, which is the time it taken for the energy stored within the cavity to fall to $\frac{1}{e}$ of its initial value. The cavity bandwidth at 10GHz is $\sim$200kHz giving a Q of 5×10^4 and τ_c of 1μs. The observed Q is diminished by the coupling of radiation into the cavity by the antenna.

2.3 Supersonic Expansions

The complexes themselves are produced by a supersonic expansion from a pulsed solenoid valve mounted in one of the mirrors. Expansions of this type have become increasingly popular as a tool for studying molecular systems. The expansion generates a beam of molecules with low effective temperature and a narrow velocity distribution.

The expansion is an adiabatic free expansion of gas through a nozzle converting the random thermal motion into directed mass flow. For a supersonic expansion[14]

$$\lambda \ll D \tag{2.7}$$

where λ is the mean free path of the gas behind the nozzle and D is the nozzle diameter. This relationship ensures that large numbers of collisions take place in the nozzle. The mean free path of a gas is given by

$$\lambda = \frac{kT}{\sqrt{2}\sigma p_0} \tag{2.8}$$

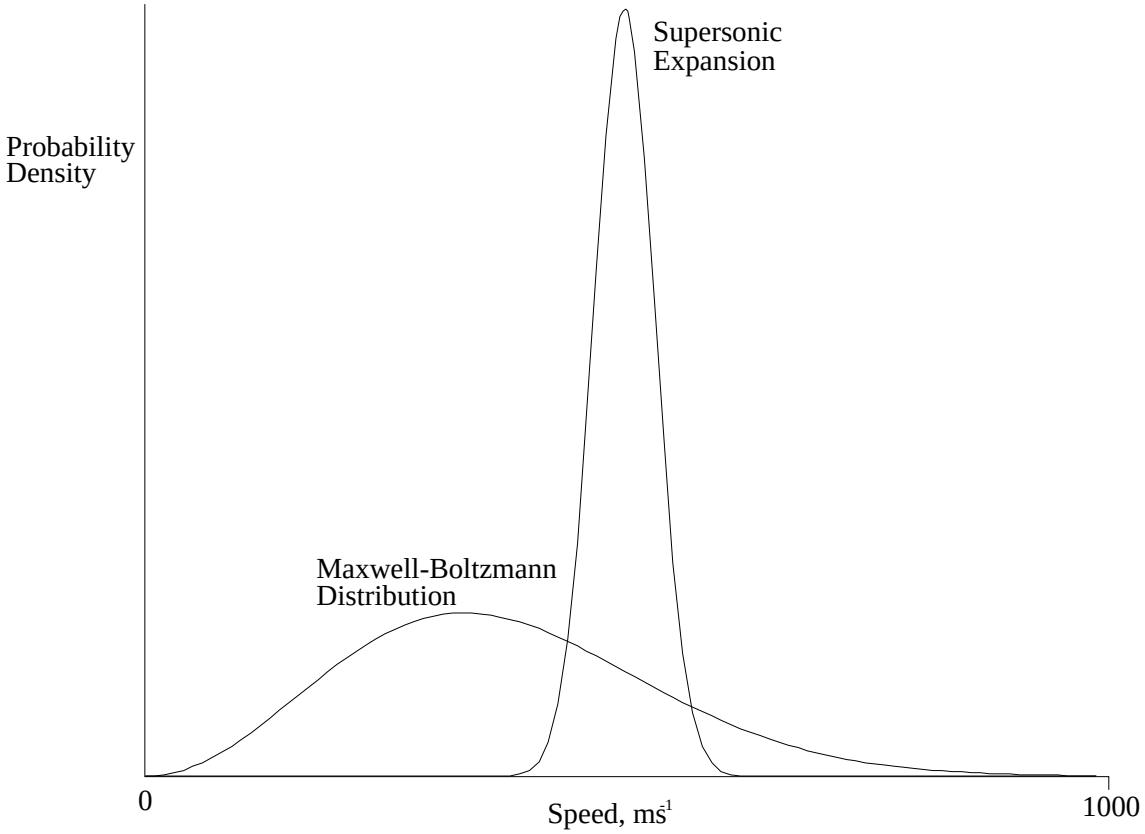

Figure 2.5: Probability Density Functions of argon for a Maxwell-Boltzmann distribution at 298K and a supersonic expansion initially at 298K attaining a final temperature of 5K.

where k is Boltzmann's constant, T is the temperature, σ is the collision cross-section and p_0 is the pressure, and the velocity distribution behind the nozzle can be modelled by a Maxwell distribution.

$$f(\nu) = 4\pi\left(\frac{m}{2\pi kT}\right)\nu^2 \exp\left(-\frac{m\nu^2}{2kT}\right) \tag{2.9}$$

which has an average velocity of

$$\nu_{av} = \left(\frac{8kT}{\pi m}\right)^{\frac{1}{2}} \tag{2.10}$$

where m is the mass of the particle. The translational temperature of a gas can be described in terms of the width of the velocity distribution of the molecules. This temperature is the one contained in the Maxwell distribution. A reduction in the width of the velocity distribution thus

implies a reduction in the translational temperature of the gas.

During the expansion many binary collisions occur at a rate related to the initial pressure and it is these collisions which narrow the velocity distribution and cause the cooling of the rotational and vibrational modes. Indeed it is believed that rotational relaxation will be so efficient that the rotational temperature will not differ much from the translational temperature of the expansion.[15] An examination of Figure 2.5 which shows the different widths of the velocity distributions for a Maxwell-Boltzmann distribution and a supersonic expansion. Once the expansion is a few nozzle diameters from the orifice then density of the expanding gas has reduced so that no further collisions take place and a collision free region is entered.

The ratio of the initial temperature, T_0, and final temperature, T, are given by

$$\left(\frac{T}{T_0}\right) = \left(1 + \frac{\gamma - 1}{2} M^2\right)^{-1} \tag{2.11}$$

where γ is the ratio of the heat capacities, and M is the Mach number and may be approximated by[16]

$$M = A \left(\frac{X}{D}\right)^{\gamma - 1} \tag{2.12}$$

where X is the distance from the nozzle and D is the nozzle diameter. A is a constant that depends on γ and is 3.26 for a monatomic gas. The flow velocity of the expansion at a point a few nozzle diameters from the nozzle is greater than that of the local speed of sound, hence the appellation, supersonic.

The collisions that take place during the expansion also provide the means by which complexes can be produced. Once the expansion has reached the point at which the thermal energy drops below the binding energy of the cluster, complex formation may take place. The mechanism for the formation of clusters has been considered extensively and it is generally recognised that the initial dimerization and perhaps several subsequent steps in the growth towards a critical size of nucleus must involve a third body.[17, 18] The third body provides a sink for the excess kinetic energy of the collision to stabilise the complex. Three body collisions are only feasible in the early stages of the expansion while the density of the gas is still high. After the expansion has travelled a few nozzle diameters from the nozzle the expansion enters a collision free region

in which a complex can exist indefinitely, or at least sufficiently long for spectroscopy to be performed.

The properties of the expansion can be varied to favour formation of particular sizes of clusters[19] because cluster formation depends on the number of collisions. A higher stagnation pressure behind the nozzle increases the number of collisions and thus enhances the likelihood of higher clusters.

2.4 Antennas

In the construction of the cavity a method is required for the transference of the microwave radiation from the circuit to the cavity. This is achieved by an antenna inserted at the centre of one of the mirrors. Two types of antenna are used dependent on the frequency region involved, from 6-18GHz a coaxial aerial is used and from 18-26GHz a Gordon Coupler is used.

The reciprocity theorem states effectively that the optimum position for coupling power into the cavity is also the optimum position for coupling power out of the cavity.[20] The same antenna can thus be used for both supplying radiation to the cavity and measuring the decaying radiation from the molecular systems.

In order to transfer the maximum power to the cavity without getting reflected waves from the interface between the cavity and the transmission line, the impedance of the cavity and antenna should be matched.

2.4.1 Coaxial Aerial

The coaxial antenna is constructed by stripping the outer conductor and dielectric from a section at the end of a coaxial cable and bending the inner core to approximately 90° relative to the main cable to form one half of a conventional dipole.[21] An aerial of this type provides broadbanded coverage of the frequency region 6-18GHz. The radiative pattern of such an aerial is functionally similar to that of a dipole which matches well with the fundamental mode of the cavity.

The coupling to the cavity can be adjusted in two ways

1. By variation of the position of the antenna relative to the mirror which can be used to optimise impedance matching. Calculations[22] indicate that the optimum distance between the mirror and the antenna is ~ 0.1 of a wavelength.

2. By variation of the length of the antenna, which should be approximately one half wavelength, to give the best coupling by producing a node at each end of the aerial. If the

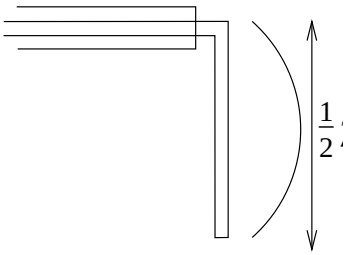

Figure 2.6: Schematic diagram of the form of the wave produced on a half-wave aerial.

aerial is longer that this more energy is distributed into lobes of the radiation pattern at high angles, which tends to place more power into higher order modes of the Fabry-Perot cavity which have less favourable interactions with the supersonic expansion.

At 10GHz the wavelength is approximately 3cm which implies that the length of the aerial is required to be about 1.5cm.

2.4.2 Gordon Coupler

At 18GHz the losses associated with coaxial cable start to become significant and it is necessary to change the circuit components to waveguide. A different method of coupling is required to connect waveguide to the cavity, and this is provided by the Gordon Coupler,[23–27] illustrated in Figure 2.7. It consists of a section of waveguide which is tapered to beyond cutoff. A waveguide has a characteristic frequency below which radiation will not propagate, referred to as the cutoff frequency. The characteristic frequency is inversely related to the dimensions of the waveguide so as the dimensions of the waveguide decreases the cutoff frequency increases,[28] preventing the microwave radiation propagating. A dielectric plunger constructed of Teflon is inserted into the waveguide which brings the waveguide back below cutoff. The plunger is attached to a threaded

rod that can be used to move the dielectric. By altering the position of the dielectric the coupling to the cavity can be changed and thus optimised.

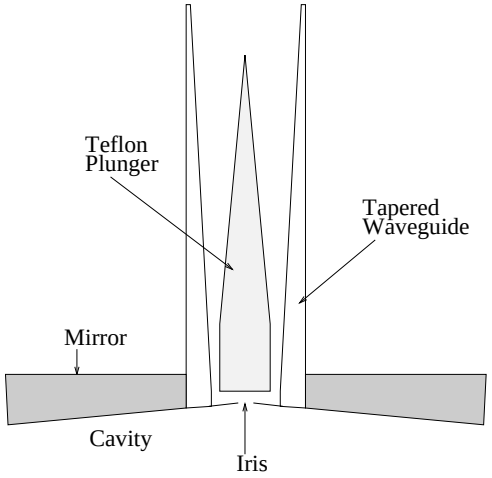

Figure 2.7: Gordon Coupler

Two Gordon couplers have been built to cover the range 18-26GHz because each coupler has a range of ∼4GHz. Each of the couplers has two irises because the iris needs to be tuned by altering its diameter and thickness[29] and covers a narrower frequency range than the coupler itself.

2.5 Line Shapes

A significant aspect of any experiment which must be taken into consideration is the line shape that is generated and the factors which contribute to it. The line width is an indicator of how accurately a transition can be measured and how easily it can be separated from another transition nearby. Experimental line widths are approximately 10kHz.

In the most basic theoretical terms you would expect the transition to be an infinitely narrow line, a delta function, representing the difference in energy between the two states. However, there are number of experimental factors which influence the final line contour. The most fundamental is called the natural line width which is the minimum line width that could be measured in the absence of any other influences. It is caused by the disturbance of the molecule due to

zero-point vibrations of electromagnetic fields which are always present in free space.[30, 31] At microwave frequencies it is about 10^{-6}Hz[32] and does not significantly affect the observed line width because other effects are much larger.

The molecules may also be disturbed by collisions with other particles, which is referred to as pressure broadening because the rate at which collisions occur is a function of the pressure. A collision can cause a transition to a different state reducing the lifetime of the state and so increasing the uncertainty of the energy broadening the line. The simplest method for minimising this is to reduce the pressure but a commensurate reduction in the signal strength will occur. The supersonic expansion counters this by generating a virtually collision free environment for spectroscopy. A background pressure of 7×10^{-5}atm is observed within the chamber when operating the pulsed nozzle at 20Hz. Although this can be varied by changing the frequency of pulses, constrained by the pumping system.

The Doppler effect is the other major property which influences the line width for all systems. The molecules within the expansion possess a velocity distribution determined by the effective temperature of the beam. By the Doppler effect the molecules travelling at different speeds interact with radiation at different frequencies to give a distribution of transition energies. The cooling effect of a supersonic expansion minimizes this because of the low effective temperature of the beam. In addition to broadening the Doppler effect also imposes a doublet structure onto a signal, because the gas is injected along the cavity axis. The radiation interacts with the molecules as it travels in both directions giving an equal and opposite shift.[33, 34] The centre of the line is just the arithmetic mean of the frequencies of the two components. Using the arrangement narrower lines are obtained because the beam waist of the Fabry-Perot cavity excludes molecules which have a large transverse velocity component. The alternative orientation with the nozzle perpendicular to the cavity axis is not able to do this and often exhibits a poorly split doublet structure. These frequencies are given by

$$\nu_{\pm Doppler} = \nu_0 \left(1 \pm \frac{V}{c}\right) \tag{2.13}$$

where V is the velocity of the gas, c is the speed of light and ν_0 is the frequency of the transition. Experimentally it is seen that the separation of the components does vary in proportion to the

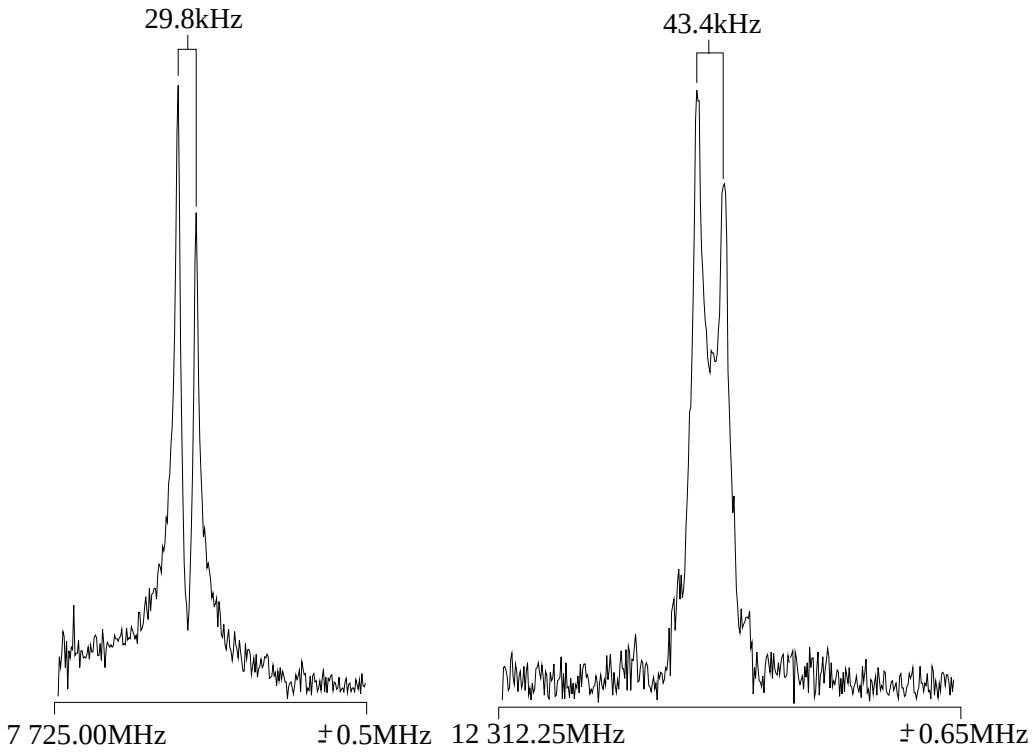

Figure 2.8: Illustration of the Doppler Splitting of a signal on the Fourier Transform Microwave Spectrometer from the complex NO-HF

frequency, as one would anticipate.

Broadening also occurs in the spectra of complexes that contain unpaired electrons. These electrons can interact with the Earth's magnetic field to produce splittings of the spectra. This field is removed by the use of three mutually perpendicular Helmholtz coils arranged about the cavity. This collapses the Zeeman components back onto one another. However it is not possible to completely remove the field which results in slightly broadened peaks.

2.6 Interaction of radiation with matter

The theory required to comprehend the process of the interaction of the applied radiation and the expanding molecules in a Fabry-Perot cavity has been dealt with extensively by Balle and Flygare.[35–38] The purpose here is to illustrate the salient points of the interaction and how that

influences the execution of the experiment.

A microwave pulse, τ_p, of length 1-2μs, which is short so that the translation of the molecules is negligible during the pulse, is applied to the Fabry-Perot cavity. A pulse of width 1μs generates a band of frequencies 1MHz wide about the central frequency. This causes an electric field to be established within the cavity which has a characteristic decay time, τ_c. If τ_p is greater than τ_c a stationary state electric field is attained within a short time, although this is not required. The molecules in the expansion encounter the electric field which induces a polarization of the molecules if the molecules have a transition within the bandwidth of the applied radiation. The maximum polarization is achieved for a $\frac{\pi}{2}$ pulse which satisfies the condition

$$\tau_p \kappa \epsilon = \frac{\pi}{2} \tag{2.14}$$

where ϵ is the electric field in the cavity and κ is the electric dipole transition moment for the desired transition between two states a and b, $\langle a|\mu|b\rangle$. The equation indicates many properties of the experiment. The ability to detect a transition is a function of the electric field within the cavity, the transition dipole moment and the pulse width. The detection of a weak transition, one of low transition dipole moment, can be improved by either increasing the pulse width or the electric field within the cavity. The electric field in the cavity is a function of the Q of the cavity and the input power available. For the current configuration with an input power of 20dBm and a Q of 10^4 the minimum measurable transition dipole moment is about 0.025Debye.

Once the microwave pulse has ceased, the static electric field within the cavity generated by the pulse must decay away rapidly to leave the electric field caused by the macroscopic polarization of the molecules. A cavity with a resonant frequency bandwidth, $\Delta\nu_c$, of 200kHz where

$$\Delta\nu_c = (2\pi\tau_c)^{-1} \tag{2.15}$$

has a characteristic decay time, τ_c, of 0.8μs. The exciting radiation does therefore decay rapidly, and provided that the polarization of the molecules decays more slowly then the electric field is detected. The polarization of the molecules decays with a phenomenological time constant T_2 which reflects the gradual dephasing of adjacent dipoles caused by collisions and the Doppler effect.

Atomic Mass			Relative Abundance	Frequency(MHz)
O	C	S		
16	12	32	1.0	12 162.979
16	12	34	$4.0\text{x}10^{-2}$	11 845.712
16	13	32	$1.0\text{x}10^{-2}$	12 123.845
18	12	32	$2.5\text{x}10^{-3}$	11 409.717
16	13	34	$4.0\text{x}10^{-4}$	11 823.461
18	12	34	$1.0\text{x}10^{-4}$	11 119.931
18	13	32	$2.5\text{x}10^{-5}$	11 382.133
18	13	34	$1.0\text{x}10^{-6}$	11 089.740
17	12	34	$3.5\text{x}10^{-5}$	11 767.395

Table 2.1: Relative Abundances and Frequencies[39] of the isotopomers of OCS for the calibration of the Microwave Spectrometer

2.7 Sensitivity

A method is required for the calibration of the spectrometer. In absolute terms this is very difficult to achieve because of the many variables upon which the sensitivity depends, for example, the quality of the coupling of the antenna to the cavity, the mixing of the gases, the conditions of the expansion, the insertion losses of microwave components at a given frequency.

The spectrometer is thus calibrated by using OCS[40] as a reference system because OCS has a moderate dipole moment, 0.715D, and a rotational transition which falls into the centre of the frequency range of the spectrometer. Additionally OCS has a variety of isotopomers with differing abundances for confirmation of sensitivity, as illustrated in Table 2.1.

Using a 2% mixture of OCS in argon it is possible to observe the $^{16}O^{13}C^{34}S$ isotopomer after one data collection cycle at a signal to noise of about 2:1. The full width half maximum(FWHM) line width of one component of the signal for the major isotopomer of OCS is $\sim$12kHz at 12.1GHz, which is a resolution of 1 part in 10^6. This high resolution coupled with the high sensitivity makes Fourier transform microwave spectroscopy an effective method for the investigation of hyperfine effects within complexes.

2.8 Microwave Circuits

The microwave circuit provides the mechanism by which radiation is transferred to the Fabry-Perot cavity and collected from it. There are a number of different microwave circuits which have been employed at various times for the collection of data in this thesis. The microwave circuits are dealt with in a pseudo-chronological fashion. The figures in brackets after a component refer to the list in Table 2.2.

2.8.1 18-26GHz Homodyne Microwave Circuit

This is the simplest of the microwave circuits, illustrated in Figure 2.9, which was initially used in all frequency ranges and is still used, in a modified form, for measurements from 18-26GHz. The circuit will be explained by following the path of the radiation through the circuit and discussing the function, where relevant, of each of the components.

The microwave radiation, ν_m at 13dBm, is generated by a Wiltron microwave synthesizer(1) which can be tuned across a range from 2-20GHz and generate powers of up to 20dBm. The radiation is transferred to the main circuit by a flexible coaxial connection and is divided into two components, in a power divider(2), one half continuing on into the cavity the other half being utilised later in the circuit. In the 18-26GHz circuit the radiation then passes into a frequency doubler and amplifier configuration(17) because the frequency source is limited to frequencies below 20GHz. In a conventional circuit this is not required but an amplifier(10) may optionally be used to produce more power. After this there is a switch(9) which is used to control the radiation entering the cavity. In normal operation the switch is pulsed open for about one microsecond which generates a burst of radiation with a bandwidth approximately 1MHz. When the cavity is being tuned the switch is held open. Before the cavity the radiation passes through a circulator(19) and finally an antenna, as described in Section 2.4.

After suitable delay, to ensure that virtually all of the exciting microwave radiation has dis-

sipated, the decay of radiation, ν, from any polarized molecules is detected via the antenna passing out through a circulator(19) into the detection arm of the circuit. Here the signal is first amplified(16) before passing through a directional coupler(24) which samples the incident radiation with a detecting crystal(18) and is used when tuning the cavity. The majority of the radiation continues onward until it reaches a switch(20) which is opened for detection. The radiation passes through an isolator(23) and into a harmonic mixer(21) which accepts the other component of the microwave radiation from the power divider. These mix together to produce a signal centred at 0V with with the frequency, $|\nu_m - \nu|$, from the radiating molecules imposed upon it This is amplified further and the passed to a computer for digitization at 4MHz giving a spectral range of up to 2MHz.

2.8.2 Heterodyne Detection Circuit

This is the first stage of improvement from a homodyne detection system, and is illustrated in Figure 2.10.

The Wiltron microwave synthesizer(1) is used as the source of microwave radiation, ν_m, at powers of up to 13dBm, which is divided into two components by a power divider(2). One component enters a single sideband generator(7) and the other half is used later in the circuit. The single sideband generator takes an additional input of 30MHz which is mixed with the microwave radiation to create the upper sideband of the signal, (ν_m+30)MHz. The 30MHz is produced by a frequency multiplier fed with a 10MHz reference signal from the microwave synthesizer. This signal is attenuated and amplified. The attenuation is necessary to match the power coming from the single sideband generator, which has minimum input power requirements, to that which will not cause the amplifier(10) to exceed its output capability. This gives us a signal of (ν_m+30)MHz at powers of up to 23dBm. After the output of the amplifier there is a switch(9) and a circulator(6) before the antenna leading to the resonant cavity.

The polarization of molecules, ν, is then detected by the same antenna, see Section 2.4, pass-

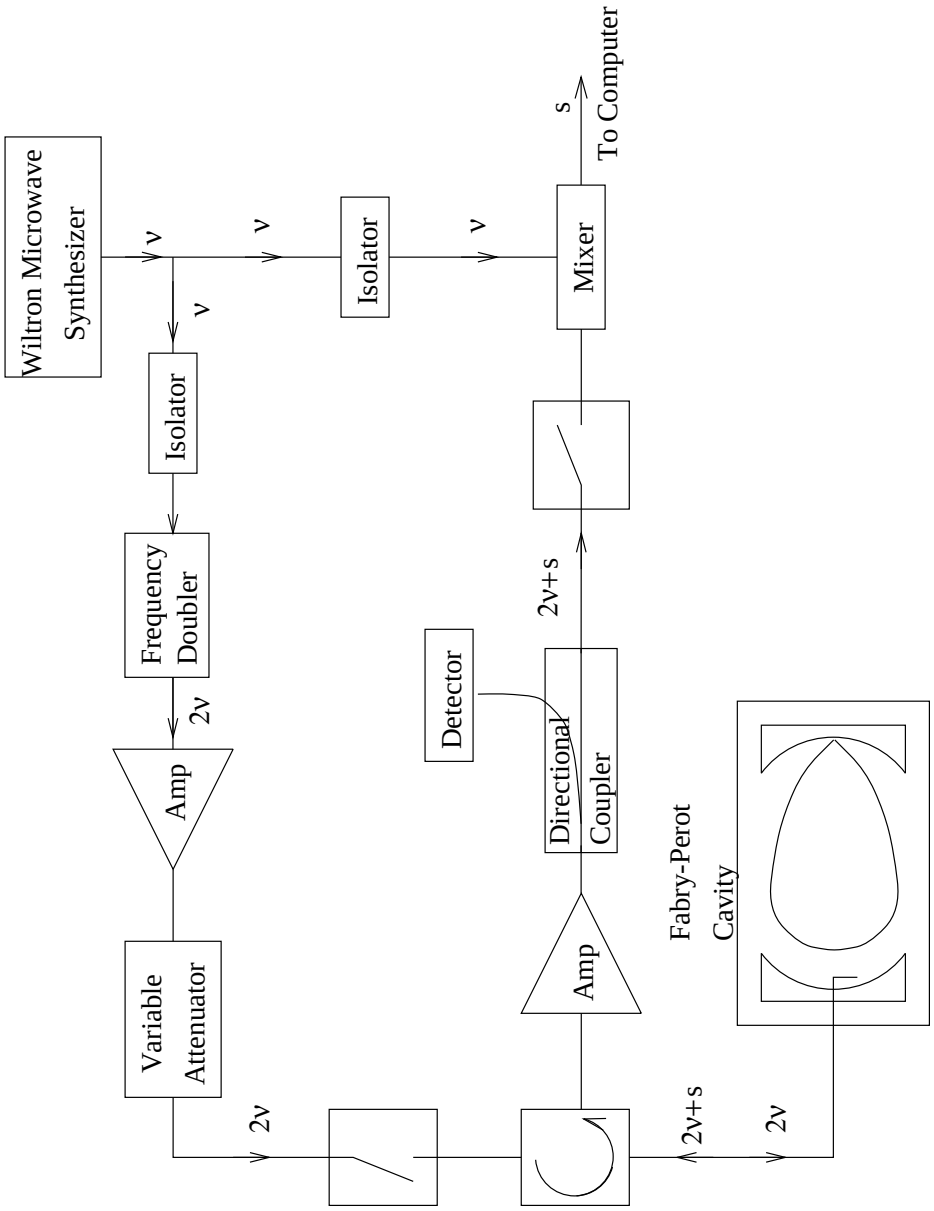

Figure 2.9: Basic homodyne circuit used currently in the frequency region 18-26GHz

ing through the circulator into the detection arm of the circuit. Firstly the signal is amplified(3 or 12) before entering a directional coupler(13) which samples the radiation and passes a small proportion onto a detector(11) which is used to tune the cavity. The majority of the radiation reaches a switch(9) which is opened when detection takes place. Here it enters an image rejection mixer(5) where it is mixed with the other half of the radiation from the power divider. A 30MHz signal is generated at this point, the difference of the output from the cavity and the radiation from the microwave synthesizer. This 30MHz radio frequency signal is amplified and filtered, with an active bandpass filter. It is then mixed with 30MHz in a double balanced mixer(15) to generate output with a frequency of $|\nu - \nu_m|$MHz which is passed to the computer for digitisation at 10MHz, giving a spectrum of width 5MHz based around 0MHz.

2.8.3 27.5 MHz Heterodyne Detection Circuit

In basic terms this circuit is identical to the standard heterodyne detection circuit. The differences arise in the generation of the radio frequency signals and in the final mixing stage, shown in Figure 2.11. In this circuit a pair of locally constructed synthesizers, phase locked to the reference frequency from the microwave synthesizer(1), are used to generate 30MHz and 27.5MHz for the mixing stages. The 30MHz signal is fed into the single sideband generator(7) but the 27.5MHz is used in the final mixer(15) to give an output which is centred on 2.5MHz as opposed to the signal based around dc from the previous heterodyne circuit. The 30MHz signal is filtered with a bandpass filter centred at 30MHz with 3dB of attenuation at 27.5MHz. Transitions which lie both above and below the central frequency can now be distinguished in a single scan where two scans at different frequencies would have been required. The signal to noise is improved because the noise that was below the centre frequency would in the mixing come in above dc. The filtering of the signal reduces the amplitude of any noise below 27.5MHz so that in the mixing the observed noise is reduced.

The data collected are centred on a frequency of 2.5MHz and the data collection could start

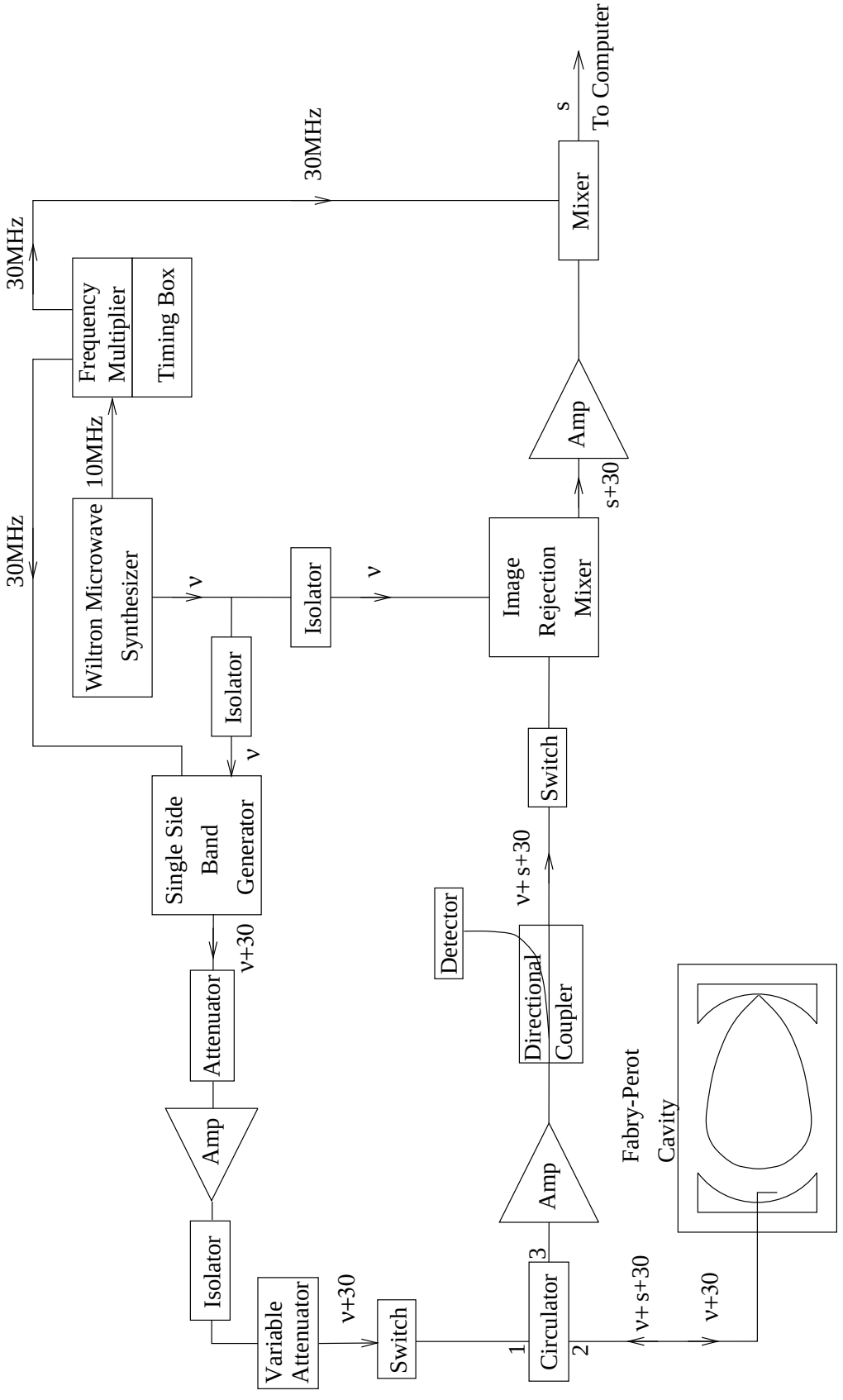

Figure 2.10: Heterodyne microwave circuit for a Fourier Transform Microwave Spectrometer

at any point of the 2.5MHz cycle. This would cause slight phase errors between collected cycles reducing the signal to noise. The radio frequencies generated by the two synthesizers are mixed together to produce a 2.5MHz signal which is used by the timing box to ensure that the trigger signals sent out will have a consistent phase with the central 2.5MHz signal. The A/D card is also driven by the 10MHz reference frequency from the Wiltron microwave synthesizer to maintain the phase of the data collection.

Table 2.2: Microwave Components and Specifications

Number	Make and Model	Function	Specifications
1	Wiltron	Microwave Synthesizer	2-20GHz Power: 1-20dBm
2	Microlab D2-9FF	Power Divider	6-18GHz Insertion Loss: 3dB
3	Avantek AWT 18675	Amplifier	6-18GHz Gain: 35dB Noise: 4.5dB Output: 20dBm
4	MaCom ML6560-117	Absorptive Attenuator	6-18GHz Insertion Loss: 2.8dB Return Loss: 11.7dB Attenuation: 53dB
5	Miteq IRE0618LI1A	Image Rejection Mixer	Conversion Loss: 9.5dB Image Rejection: 28dB
6	Microwave Associates ML3G-6100	Circulators	 4-8GHz Insertion Loss: 0.4dB Isolation: 20dB
	ML3G-9700		7-12.4GHz Insertion Loss: 0.4dB Isolation: 20dB
	ML3G-15200		12.4-18GHz Insertion Loss: 0.7dB Isolation: 19B
7	Miteq	Single Sideband Generator	6-18GHz

Number	Make and Model	Function	Specifications
	SME0618LI1A		Input Power: 10dBm Conversion Loss: 12dB Sideband Rejection: 28dB
8	Isolator ML2J718-83	7.5-18GHz	 Insertion loss: 0.9dB Isolation: 15dB
9	General Microwave F9114	PIN diode switch	6-18GHz Isolation:80dB Insertion loss 1.9-2.6dB
10	Avantek APT-18649	Amplifier	6-18GHz Gain 40dB Noise 10dB Output 23dB(min)
11	Omni-Spectra 20790	Point Contact Diode Detector	0.01-18GHz Sensitivity: 40mV/mW Maximum Power: 100mW
12	Miteq JS4-12001800-16	Low Noise Amplifier	12-18GHz Gain: 37dB Noise: 1.6dB Output: 8dBm
13	Microlab CB-86F	Directional Couplers	 6-12.4GHz Coupling: 6dB Directivity: 17 dB Insertion Loss: 2dB
	CB-106F		12.4-18GHz Coupling: 6dB Directivity: 15 dB Insertion Loss: 2.2dB
14	Mini-Circuits ZAD-3	Double Balanced Mixer	LO/RF: 0.25-200MHz IF; DC-200MHz Conversion Loss: 8.5dB LO-RF Isolation: 45dB LO-IF Isolation: 40dB
15	Mini-Circuits ZFM-3	Double Balanced Mixer	LO/RF: 1-1000MHz IF; DC-1000MHz

Number	Make and Model	Function	Specifications
			Conversion Loss: 8.5dB LO-RF Isolation: 40dB LO-IF Isolation: 35dB
16	Microwave Solutions Inc IISH-8344301WW	Amplifier	18-26.5GHz Gain: >26dB Noise: <5dB Output Power: 5dBm
17	Miteq MAXZ0113	Frequency Double and Amplifier	Input: 6.5-13GHz Output: 13-26GHz Gain: -5dB Input Power: 10dBm
18	Dorado CD-42(9114)	Crystal Detector	18-26.5GHz Sensitivity: 17mV/10μW
19	Dorado CD-054	Circulator	18-26.5GHz Insertion Loss: 0.5dB Isolation: 20dB
20	MaCom 7-42-431	PIN diode switch	18-26.5GHz Isolation: 30 dB Insertion Loss: 1.2 dB
21	OMLC175001	Harmonic Mixer	
22	Dorado VPS-42	Phase Adjuster	18-26.5GHz
23	Speary D41K5	Isolator	18-26.5GHz Insertion Loss: 1dB Isolation: 25 dB
24	MC-201-14A	Directional Coupler	Coupling: -10dB
25	Hewlet-Packard 8620C	Sweep Oscillator	
	86245C	RF Plugin	5.9-12.4GHz
	86260A	RF Plugin	12.4-18GHz
26	Hewlet-Packard 5345A	Electronic Counter	
	5255A	Frequency Converter	3-12.4GHz
	5256A	Frequency Converter	8-18GHz

Number	Make and Model	Function	Specifications
27	PTS 300	Frequency Synthesizer	0.1-300MHz
28	Hewlet-Packard 8709A	Synchronizer	

2.9 Timing

The key to performing virtually any experiment successfully is the timing with which the components within the apparatus are triggered. The timing in the microwave circuit is initially triggered by a pulse from a computer control system which is sent out by an expansion card in the computer, a PC-30 card. This enters a timing control box which consists of a series of modules to trigger different parts of the circuit with the relevant delays for optimal data collection. The first device which receives a signal is the valve controller which propagates that signal on to the solenoid valve which opens to allow gas into the cavity. Next is the microwave switch which is opened approximately 700μs after the valve is triggered. A long delay is required here to allow the solenoid valve to open and for the expansion of gas to reach the centre of the cavity. The solenoid is slow because it is an inductor in which the rise of current is proportional to the applied voltage[41] and a level of current has to be achieved before the magnetic field in the solenoid will move the armature. The valve is kept open for approximately 500μs. The microwave switch being timed to coincide with the expansion reaching the centre of the cavity. The timing thus varies with the carrier gas being used, see Section 2.3. The width of the microwave pulse is also carefully controlled because it determines the range of frequencies that are fed into the cavity. For example, an open time of 1μs generates a pulse of width 1MHz which is similar to the bandwidth of the cavity.

The detector switch is triggered next, opening after sufficient time has been allowed for the exciting radiation to decay away, referred to as cavity ring down. This switch is tuned manually using an oscilloscope to display the signal. Incidentally the detector switch also shuts

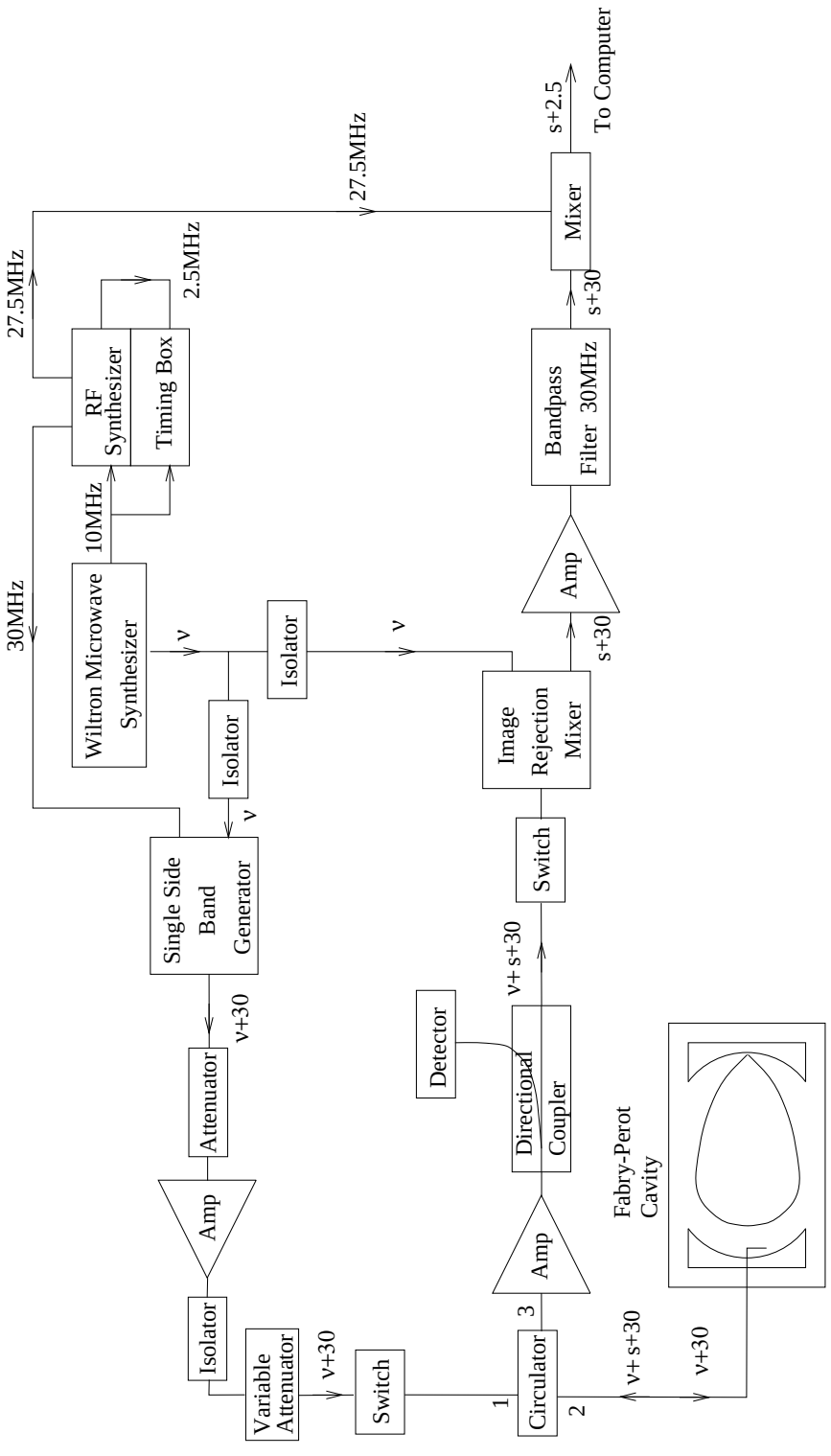

Figure 2.11: Heterodyne circuit for a Fourier Transform Microwave Spectrometer employing a 27.5MHz offset

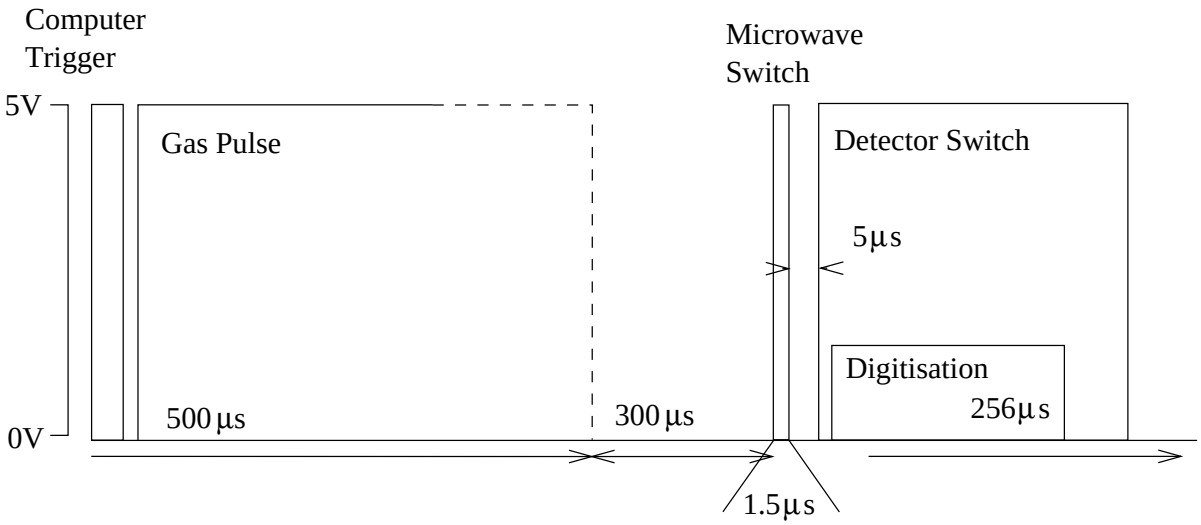

Figure 2.12: An illustration of the sequence in which trigger signals are sent to the various components of the microwave spectrometer.

the 30MHz frequency to the single sideband generator, in the heterodyne circuits, which cuts out any radiation leaking through the microwave switch and generating spurious signals at the detector. After a brief interval, to allow any switching transients to pass, the data collection card in the computer is signalled and commences data collection which lasts for 256μs, at 4 to 10MHz, collecting between 1024 and 2560 data points depending on the microwave circuit in use. One cycle of data collection is now completed and the circuit is ready for retriggering.

On the next data collection the computer asserts an additional line to the timing box which prevents the gas valve from firing. The collection proceeds as pairs of cycles of data collection, the first pass of which has been described. The second data collection pass remains the same except for the absence of the gas pulse, and is illustrated in Figure 2.13. This signal is subtracted from the data previously collected, unlike the data from sequences with a gas pulse which are added, see Figure 2.14. This process removes any characteristic absorption of the cavity.

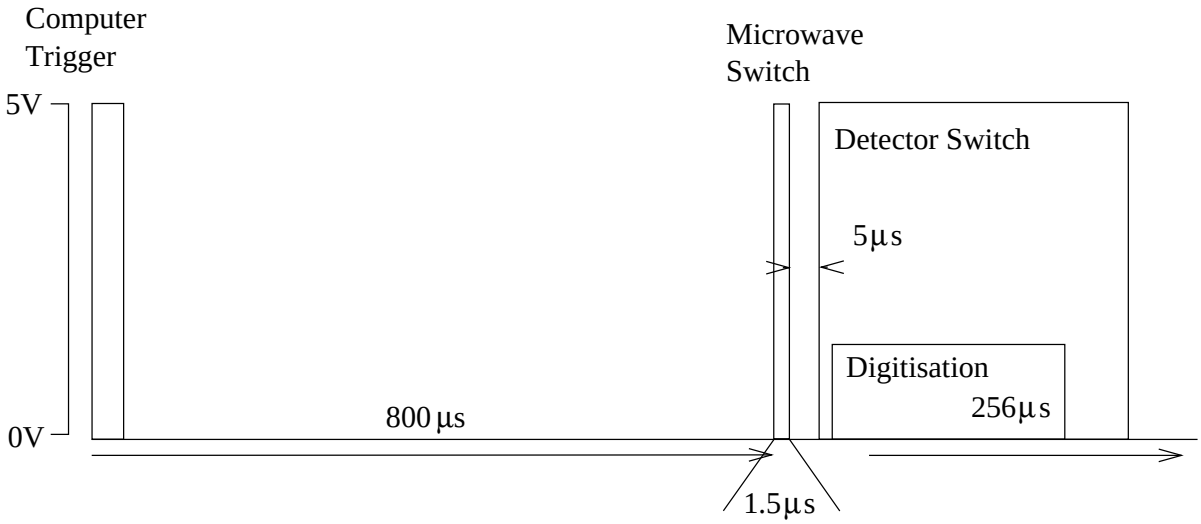

Figure 2.13: An illustration of the sequence in which trigger signals are sent to the various components of the microwave spectrometer in the absence of a gas pulse.

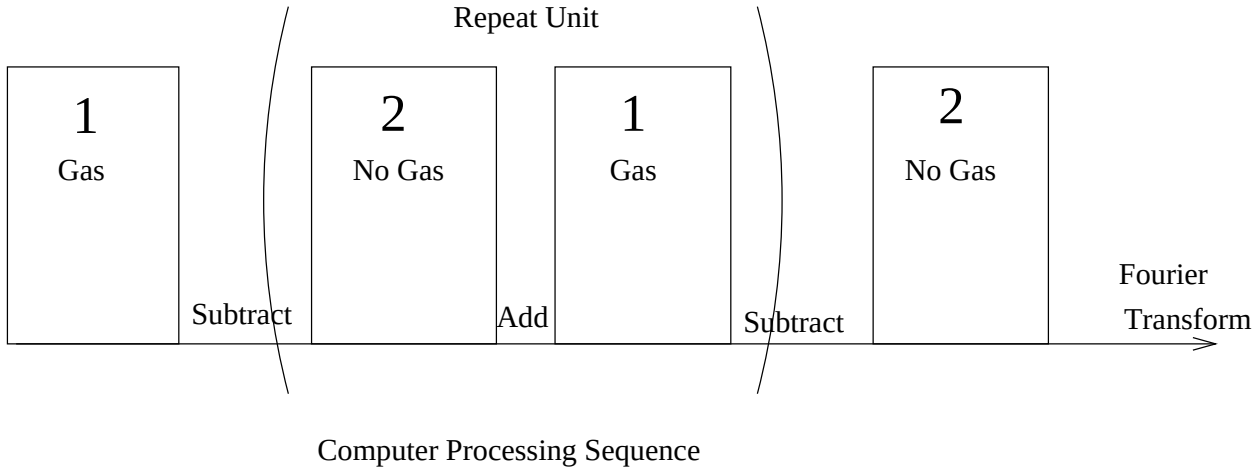

Figure 2.14: The data collection sequence for the microwave spectrometer consisting of repeated sequence of cycles with and without gas pulses.

2.10 Data Collection

It has been mentioned that the signal is collected by a computerised detection system. An analogue to digital to converter(A/D) card is fitted in a personal computer which is triggered by the timing box. For the 27.5MHz heterodyne circuit the A/D card collects 2560 data points with 8-bit resolution for 256μs, at a frequency of 10MHz using an external clock frequency derived from the microwave synthesizer. The homodyne circuits use the internal 20MHz clock which takes 5120 data points over the 256μs period. Only every fifth data point is used to produced an effective sampling frequency of 4MHz, and a data set of 1024 points.

The A/D card has a range of $\pm$0.64V so care must be taken during data collection to ensure that the signal is centered about 0V otherwise it is easy to exceed the voltage that the card can measure distorting the data collected and giving spurious signals. Strong signals may exceed these limits and they require lower gain on the variable amplifier.

2.11 Signal Processing

The data collected is in the form of either 1024 or 2560 point free induction decay, depending on the microwave circuit in use. The free induction decay exists in the time domain and the information of interest to us is in the frequency domain. It is thus necessary to manipulate the data using a discrete fast Fourier transform.[42]

$$H_n = \sum_{k=0}^{(N-1)} h_k \exp\left(\frac{i2\pi kn}{N}\right) \tag{2.16}$$

There is a property of discrete Fourier transforms called the Nyquist critical frequency,[42] f_c, given by

$$f_c = \frac{1}{2\Delta} \tag{2.17}$$

where Δ is the sampling interval. Basically this states that the maximum frequency that can be resolved is half the sampling frequency, because critical sampling of a sine wave is two sample

points per interval. For the experiment, with 1024 data points, the sampling frequency is 4MHz. Signals, including noise, above this threshold frequency can still be observed and are sampled as subharmonics of the actual frequency, folding back into the spectrum below 2MHz. This can be countered by the use of a low pass filter to attenuate any signals above 2MHz. If the alternative circuit is in use, collecting 2560 data points with a 5MHz Nyquist frequency, a band pass filter centred on 30MHz is used before the final mixing stage to remove signals from outside the desired range.

The free induction decay is passed to a Fourier transform routine which accepts a real data set. This routine passes this data to a complex Fourier transform routine as though it were a complex data set. The data is then recombined to return the positive frequency half of its complex Fourier transform. The data set is zero filled to 4096 or 8192 points before transformation. The complex spectrum which the routine returns is converted to the square root of the power spectrum by squaring the real and imaginary components and taking the square root of their sum.

For the 1024 point free induction decay, a 2048 point frequency spectrum is obtained with a 2MHz width. This gives a resolution per point of 1.953kHz. For the 2560 point free induction decay, a 4096 point spectrum is obtained with a width of 5MHz giving a resolution of 1.221kHz per point.

The transition frequencies are measured by fitting a variable size function through the first derivative of the signal, and calculating the zero point crossing.[43] The result is an offset from the central frequency, which for the basic 2MHz sample width circuit, can lie either above or below the central frequency. It is thus necessary to repeat the experiment with a small shift to the central frequency to determine the actual line position. In practice a number of spectra are taken and the average is used. For a strong transition (S/N>20), the measurement can be reproduced to an accuracy of ± 0.2kHz. However, weaker signals (S/N=2), and those from paramagnetic systems, can only be reliably measured to ± 1.5kHz.

The accuracy of any measurement depends on the accuracy of the frequency source used. The main frequency in our experiments is the 10MHz reference from the microwave synthesizer, which is used to synthesize all other frequencies. This is calibrated regularly from an atomic clock to ± 0.05kHz.

2.12 Automation

Fourier transform microwave spectroscopy is a very high resolution technique with a per spectrum bandwidth of 2MHz, but the spectrometer has a range of 6-18GHz. It would thus require at least 6000 separate spectra to cover the entire range with no overlap, which would take many weeks to collect. Often, given the difficulty of predicting the structures of complexes it is necessary to search large frequency regions before a signal is located. A procedure has thus been developed to allow the spectrometer to operate unattended for long periods, which is detailed below.

Initially the output of the spectrometer must be optimised to obtain the maximum signal, because as the frequency changes the optimisation will decrease, therefore starting with the best signal will hopefully maintain effective detection across the region scanned. The setting up involves positioning the antenna, maximizing the gas pulse, tuning the cavity resonance, and ensuring that there is enough gas mix to support the run. It may also be necessary to reduce the Q-factor of the cavity by attaching microwave absorbent foam to the mirrors. This increases the width of the dip allowing the increase of the scan interval.

Once the spectrometer is physically prepared the computer must be programmed to carry out the search. The start and stop frequencies, and the scan interval are entered, with the number of data collection cycles to take, which depends on the electric dipole moment of the complex. Around 2000 data collection cycles are suitable for a complex with a moderate dipole moment($\sim$0.5D). The stepper motor, which moves one of the mirrors via a micrometer, is set to

respond to external control signals with the direction of motion set to correspond to the direction of scanning. The scan is then started. The motor controller can only move the motor in one direction which prevents hysteresis in the mirror motion from affecting the scan.

The computer collects a spectrum, which it saves to disk for later perusal by the operator, then it tunes the spectrometer to a new frequency and starts to collect a new spectrum. It does this by moving the mirror an amount in the desired direction which is estimated from the scan interval and the current central frequency. A search for the dip is then carried out by stepping the microwave synthesizer through a range about the desired frequency(the old centre frequency plus the scan interval) and measuring the voltage on the crystal detector, the maximum being noted. If this maximum or minimum, depending on the polarity of the detector crystal, is sufficiently close to the desired frequency the microwave synthesizer is tuned to match the peak of the dip, it being simpler to tune the synthesizer, usually 0-100kHz, compared to trying to match the mirror position to the desired frequency, and a new spectrum is taken. However if the dip position is not correct then the computer will try again to position the mirrors. If after a number of tries the computer is unable to locate a dip it will halt. Once the computer reaches the stop frequency it will also stop scanning.

2.13 Helmholtz Coils

The Earth possesses a magnetic field which, for open shell complexes, can cause significant Zeeman splittings in spectra by interacting with the magnetic moment of the unpaired electron. The effect can be countered by the use of Helmholtz coils[44] to generate an opposing field to the Earth's creating a region free of magnetic fields, thus collapsing the spectra.

The coils consist of three pairs of square, guttered tracks, of dimension 1.2m in which enameled copper wire is wound. The three pairs of tracks separated by 64cm are arranged in a mutually perpendicular fashion about the vacuum chamber. A current is applied to each of the

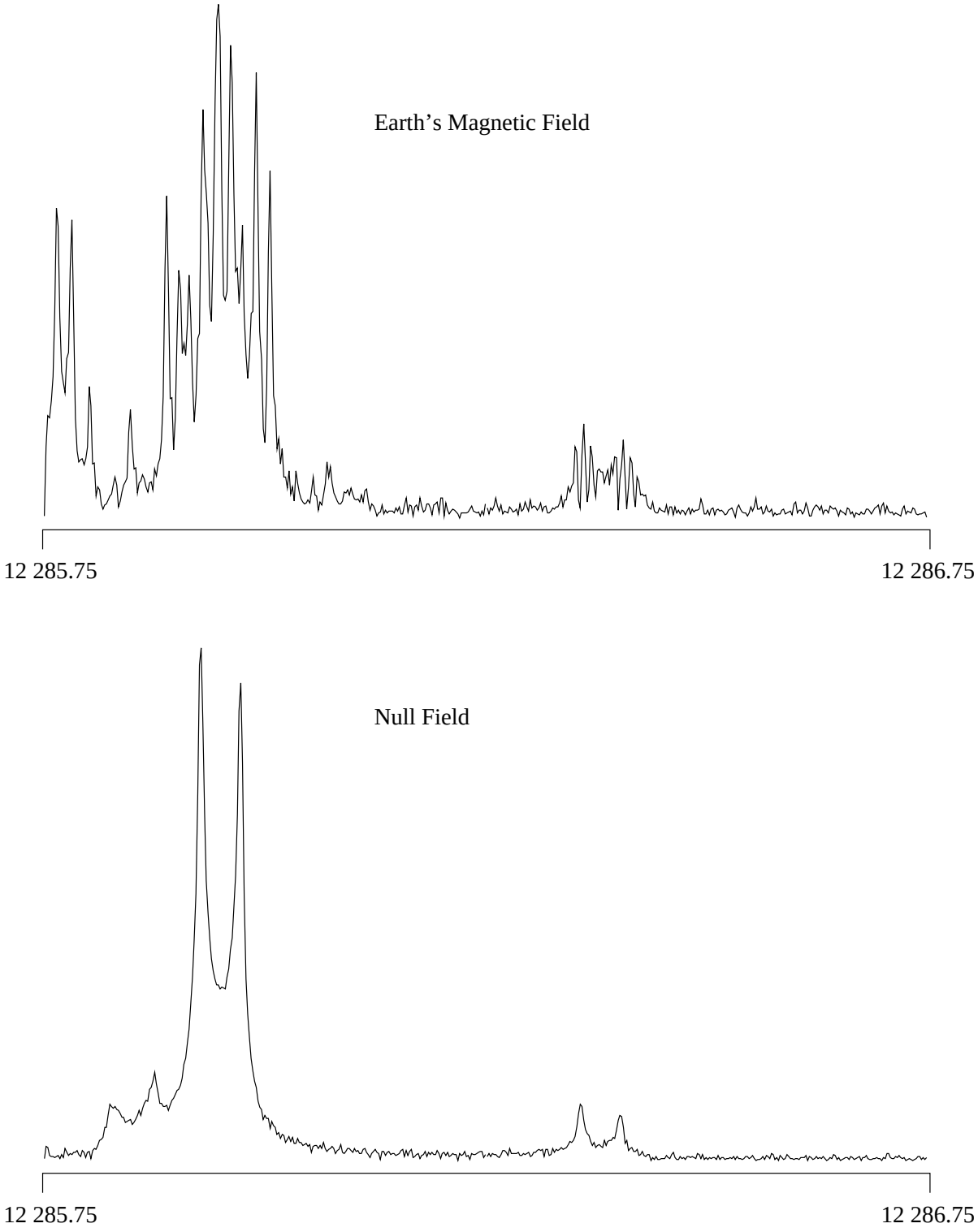

Figure 2.15: An illustration of the effect of the Earth's magnetic field on the microwave spectrum of the open-shell complex NO-HF

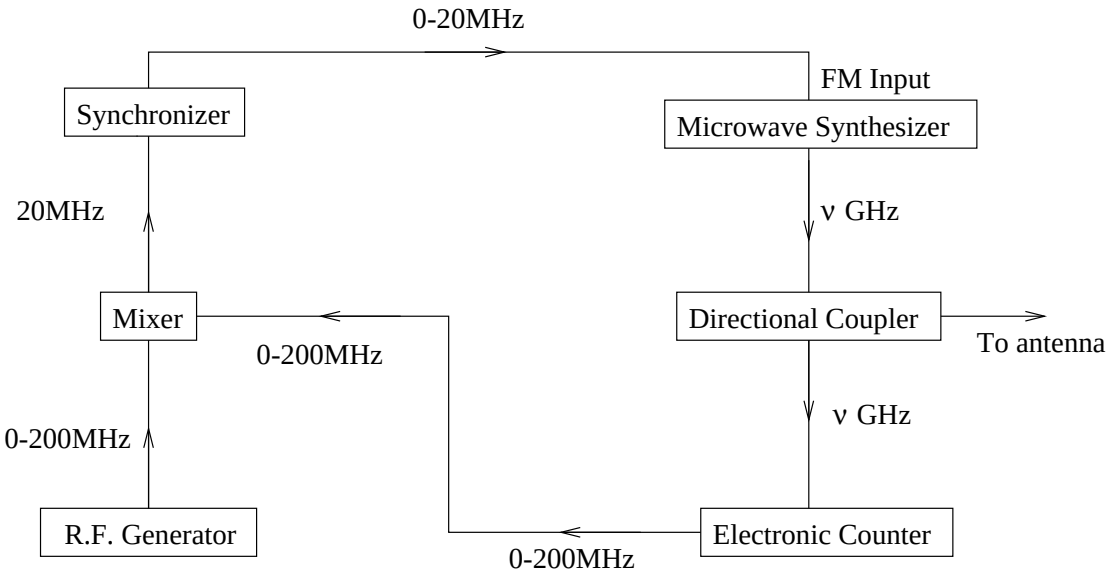

Figure 2.16: Schematic of the second circuit to generate microwaves used in double resonance experiments.

three pairs of coils. The currents required are initially set using a magnetometer to minimise the field in the chamber approximately 6cm from the exit of the nozzle. The settings are then fine tuned by looking at a strong transition of an open-shell complex to maximise the free induction decay.

The size of the chamber, 90x42x42cm, is such that it is impossible to obtain a perfectly zero field throughout the chamber. However the region of space in which the molecules interact with the microwave radiation is much smaller. It is therefore possible to achieve an effective null field with only a small increase in the line width that would be expected over a similar closed shell complex. The effect of the Earth's magnetic field on a spectrum is illustrated in Figure 2.15

2.14 Double Resonance

In some experiments where difficulty is encountered in assignment of the transitions that have been observed it can be helpful to carry out double resonance experiments. These experiments

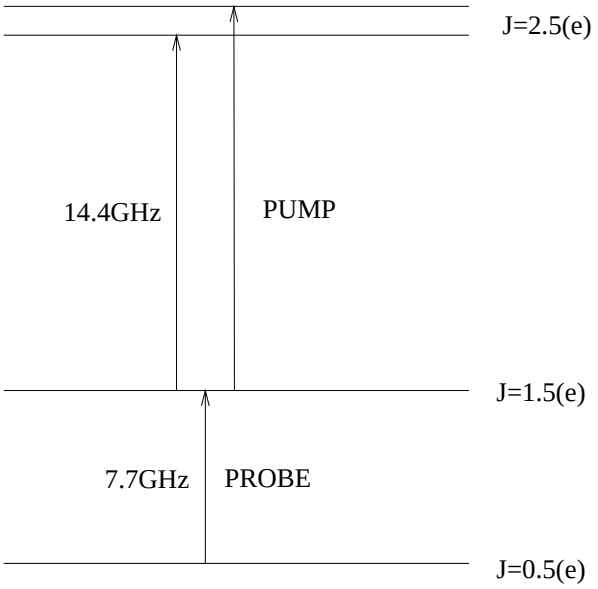

Figure 2.17: Illustration of the information obtained from double resonance

provide connections between various groups of lines. An older set of apparatus is used to generate the microwaves for double resonance.

The microwave radiation is generated by a Hewlett Packard microwave sweep oscillator(25). However the frequency produced by the sweep oscillator is not stable and has to be frequency locked. A proportion of the output of the generator is fed into an electronic counter(26) which mixes the microwave radiation with a second microwave source to generate a signal of between 0 and 200MHz. This output is mixed with another known signal of between 0-200MHz, from a radio frequency synthesizer(27), which is offset by 20MHz from the output of the counter. The mixer thus generates a signal of 20MHz which is fed into a synchronizer(28) which displays the error in the signal from that desired. The synchronizer in addition produces an error signal which is fed into the FM input on the sweep oscillator and is used to lock the output of the sweep oscillator. Once locked the microwave output frequency of the circuit can be tuned by changing the output of the radio frequency synthesizer.

The microwave radiation is introduced to the cavity from the top of the chamber by an

unterminated waveguide to coaxial connector mounted perpendicular to the cavity axis. The introduced radiation must not be resonant with the cavity otherwise it is possible to overpower the electronics in the detection arm of the microwave circuit.

This simple scheme then provides proof of a common level between transitions, see Figure 2.17. If we look at the line 7.725 210GHz of NO-HF and then apply radiation from the double resonance circuit at 14.415 114GHz the transition is dephased and disappears. By accumulating this data stacks of related lines can be generated.

2.15 Vacuum system

The vacuum chamber is constructed out of stainless steel of thickness 10mm with overlap of 5mm and internal dimensions 40x40x88cm. The main body of the chamber has two ends open which are sealed with plates and around the body are four 23cm ports. These ports are used for mounting the diffusion pump, providing mounting points for various connections and access to the chamber. One of the two end plates of the chamber has a central 10cm port through which a metal top hat arrangement is fed and the fixed mirror is bolted to the end of the top hat. The antenna is connected via this port and can simply be changed by unbolting the port with the antenna in it and inserting the new antenna to facilitate changing between a coaxial aerial and the Gordon coupler.

The pumping system consists of an Edwards Diffstak MK2 250/2000 diffusion pump which is able to displace 2000ls^{-1}, using silicon 704 oil, and a Leybold Trivac rotary pump which can pump 65m^{3}h^{-1}. The lowest pressure which can be attained with this is 9x10^{-6} mbar. The large pumping capacity allows the apparatus to be operated at higher repetition rates for spectra to be taken more quickly.

Inside the chamber there is a track mounted on the floor upon which the movable mirror rests. The carriage on the track is connected by a shaft to a micrometer driven by a stepper

motor. The configuration gives a total range for the mirror of 5cm in 2.5μm steps, to allow accurate tuning of the cavity with a wide range to ensure that more than one resonant band can be found.

References

[1] T. J. Balle, E. J. Campbell, M. R. Keenan, W. H. Flygare. *J. Chem. Phys.*, **71**, 2723, (1979).

[2] A. C. Legon, C. A. Rego. *J. Chem. Soc. Faraday Trans.*, **86**, 1915, (1990).

[3] M. Iida, Y. Ohsima. Y. Endo. *J. Chem. Phys.*, **94**, 6989, (1991).

[4] Th. Brupbacher, A. Bauder. *J. Chem. Phys.*, **99**, 9394, (1993).

[5] R. D. Suenram, F. J. Lovas, G. T. Fraser, K. Matsumura. *J. Chem. Phys.*, **92**, 4724, (1990).

[6] Y. Xu, W. Jäger, M. C. L. Gerry. *J. Mol. Spec.*, **151**, 206, (1992).

[7] W. Stahl, G. Bestmann, H. Dreizler, U. Andresen, R. Schwarz. *Rev. Sci. Instrum.*, **56**, 1759, (1985).

[8] C. Chaung, C. J. Hawley, T. Emilsson, H. S. Gutowsky. *Rev. Sci. Instrum.*, **61**, 1629, (1990).

[9] R. J. Low, C. J. Whitham, T. D. Varberg, B. J. Howard. *Chem. Phys. Lett.*, **222**, 443, (1994).

[10] G. D. Boyd, J. P. Gordon. *Bell Syst. Tech. J.*, **40**, 489, (1961).

[11] A. G. Fox, Tingye Li. *Bell Syst. Tech. J.*, **40**, 453, (1961).

[12] G. D. Boyd, H. Kogelnik. *Bell Syst. Tech. J.*, **41**, 1347, (1962).

[13] Emerson and Cumming (U.K.) Ltd Eccosorb AN-73 foam sheet.

[14] G. Scoles. *Atomic and Molecular Beam Methods Volume 2*. Oxford University Press, New York, (1992).

[15] G. M. McClelland, K. L. Saenger, J. J. Velentini, D. H. Herschbach. *J. Phys. Chem.*, **83**, 947, (1979).

[16] R. E. Smalley, L. Wharton, D. H. Levy. *J. Chem. Phys.*, **63**, 4977, (1975).

[17] D. Lippman, W. C. Schieve, C. Canestaro. *J. Chem. Phys.*, **81**, 4969, (1984).

[18] T. A. Milne, A. E. Vandegrift, F. T. Greene. *J. Chem. Phys.*, **52**, 1553, (1970).

[19] P. J. F. Gandy. *Part II Thesis*, (1991).

[20] J. D. Kraus. *Antennas*. McGraw-Hill, New York, (1988).

[21] S. Drabowitch, C. Ancona. *Antennas, Volume 2 Applications*. North Oxford Academic Publishers, Oxford, (1988).

[22] K. F. Lee. *Principles of Antenna Theory*. John Wiley and Sons, New York, (1984).

[23] J. P. Gordon. *Rev. Sci. Instrum.*, **32**, 658, (1961).

[24] T. Chang, D. Foster, A. H. Kahn. *J. Res. NBS*, **83**, 133, (1978).

[25] U. Ramon, D. N. Stamires. *Rev. Sci. Instrum.*, **41**, 147, (1970).

[26] R. N. Gould, A. Cunliffe. *The Philosophical Magazine*, **1**, 1126, (1973).

[27] J. E. Whitehouse. *Rev. Sci. Instrum.*, **49**, 541, (1978).

[28] R. E. Collin. *Foundations for Microwave Engineering*. McGraw-Hill, New York, (1992).

[29] C. P. Poole. *Electron Spin Resonance*. John Wiley and Sons, New York, (1982).

[30] C. H. Townes, A. L. Schawlow. *Microwave Spectroscopy*. McGraw-Hill, New York, (1955).

[31] W. Gordy, R. L. Cook. *Microwave Molecular Spectra*. John Wiley and Sons, New York, (1970).

[32] H. W. Kroto. *Molecular Rotation Spectra*. John Wiley and Sons, New York, (1975).

[33] J. U. Grabow, W. Stahl. *Z. Naturforsch*, **45a**, 1043, (1990).

[34] H. Dreizler. *Z. Naturforsch*, **47a**, 342, (1992).

[35] T. J. Balle, W. H. Flygare. *Rev. Sci. Instrum.*, **52**, 33, (1981).

[36] E. J. Campbell, L. W. Buxton, T. J. Balle, W. H. Flygare. *J. Chem. Phys.*, **74**, 813, (1981).

[37] E. J. Campbell, L. W. Buxton, T. J. Balle, M. R. Keenan, W. H. Flygare. *J. Chem. Phys.*, **74**, 829, (1981).

[38] H. Dreizler. *Mol. Phys.*, **59**, 1, (1986).

[39] F. J. Lovas. *J. Phys. Chem. Ref. Data.*, **7**, 1502, (1978).

[40] F. J. Lovas, R. D. Suenram. *J. Chem. Phys.*, **87**, 2010, (1987).

[41] P. Horowitz, W. Hill. *The Art of Electronics*. Cambridge University Press, Cambridge, (1989).

[42] W. H. Press, S. A. Teukolsky, W. T. Vetterling, B. P. Flannery. *Numerical Recipies in C*. Cambridge University Press, Cambridge, (1992).

[43] A. Savitzky, M. J. E. Golay. *Anal. Chem.*, **36**, 1627, (1964).

[44] A. H. Firester. *Rev. Sci. Instrum.*, **37**, 1264, (1966).

Chapter 3

Fine Structure Hamiltonian

God's last message to his creation
"We apologise for the inconvenience."
-Douglas Adams,
So long and thanks for all the fish.

3.1 Introduction

The concepts required to understand the properties of open-shell molecules have always been perceived as much more difficult than the theory for comparable closed-shell complexes. This is mainly because the presence of unpaired electrons within a molecule introduces many more possible interactions all of which must be accounted for in the theory. In particular, the ground electronic state of NO possesses both electronic orbital angular momentum, **L**, and electronic spin angular momentum, **S**. A correct description of the energy states of an NO complex needs to take into account interactions involving these angular momenta, the rotation of the complex and the removal of the Π orbital degeneracy caused by the closed shell partner.

The first treatment of the theory for van der Waals complexes of NO was by Mills et al[1] to account for the microwave spectrum of Ar-NO, which had been observed using MBERS. It is this method of modelling the complex that is applied here but with a change in the definition of the angle used to describe the relationship between the monomers. Ar-NO has an almost T-shaped configuration and it is therefore most convenient to characterize the complex in terms of

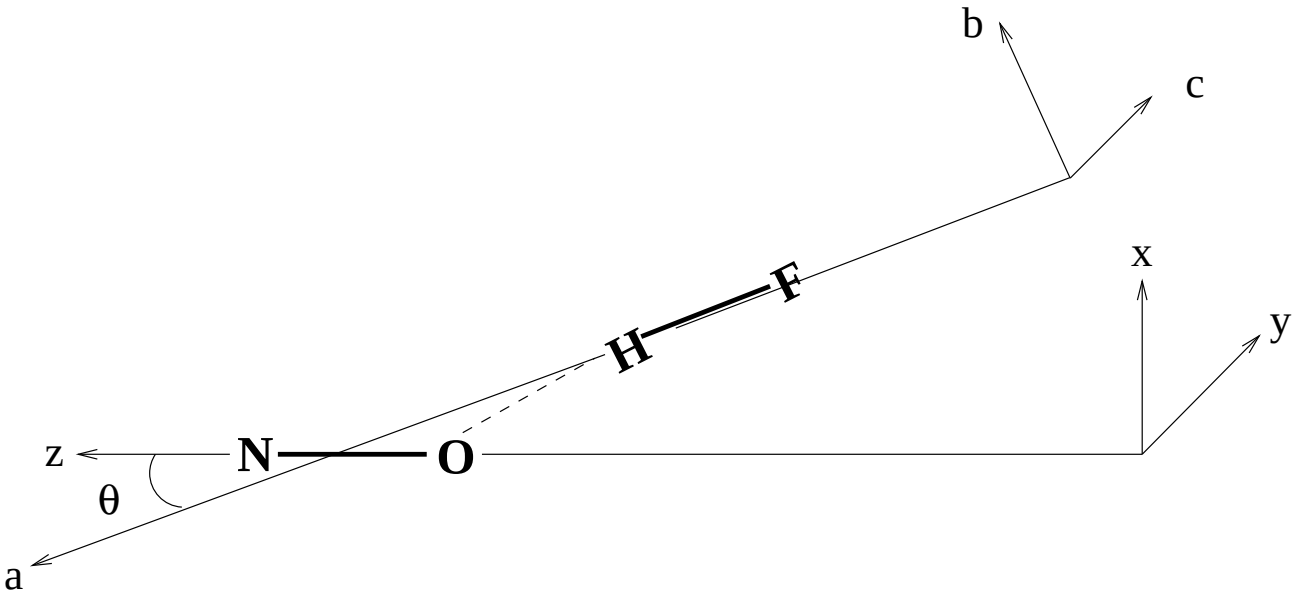

Figure 3.1: Model structure for NO-HF complex, illustrating the directions of the NO-fixed and molecule fixed axis systems.

the deviation from a T-shaped orientation. However NO-HF is closer to linear and we therefore take the deviation from a linear configuration as the angle. The two approaches are identical and for the fine structure may be converted by swapping all instances of sine and cosine functions. An alternative scheme is that of Fawzy et al[2] that differs only in the definitions of some of the terms within the Hamiltonian and includes the theory for centrifugal distortion which Mills et al. neglect because of the low rotational energy levels observed.

The theory for the fine structure of NO complexes can be applied to any ${}^2\Pi_{\frac{1}{2}}$ or ${}^2\Pi_{\frac{3}{2}}$ state complex like the hydroxyl and SH radical complexes Ar-OH and Ar-SH.

A near linear model for the NO-HF complex was proposed with the hydrogen fluoride molecule lying aligned effectively along one of the lone pairs of the oxygen in NO, as illustrated in Figure 3.1. In addition the model assumes that the molecule is planar simplifying the treament. A non-planar model would require a second angle to describe the complex.

The electronic angular momenta that are in the NO sub-unit will be projected from there

onto the principal axis, as shown in Figure 3.1. The projections of the angular momenta will depend on the angle between the NO z-axis and the a-axis of the complex defined as θ . The components of these projected angular momenta within the principal axis system of the complex are given by

$$\begin{aligned} L_a &= -L_x \sin\theta + L_z \cos\theta \qquad & S_a &= -S_x \sin\theta + S_z \cos\theta \\ L_b &= L_x \cos\theta + L_z \sin\theta \qquad & S_b &= S_x \cos\theta + S_z \sin\theta \\ L_c &= L_y & S_c &= S_y \end{aligned} \tag{3.1}$$

It is important at this juncture to note the forms of the raising and lowering operators for the angular momenta in the complex. The raising and lowering operators for the total angular momentum, **J**, are reversed in the complex because of the change between space-fixed and molecule fixed coordinate systems,[3, 4] i.e. J^+ is the lowering operator and J^- is the raising operator.

$$\begin{aligned} J^{\pm} &= J_b \pm iJ_c \\ L^{\pm} &= L_x \pm iL_y \\ S^{\pm} &= S_x \pm iS_y \end{aligned} \tag{3.2}$$

This changes the commutation relations for **J** as well

$$\begin{aligned} [J_a, J_b] &= -iJ_c \\ [L_x, L_y] &= iL_z \\ [S_x, S_y] &= iS_z \end{aligned} \tag{3.3}$$

3.2 Basis Set

A basis set from which the matrix elements can be derived needs to be selected. The literature[5, 6] shows that for NO the standard choice of basis set is Hund's case a with the orbital and spin angular momenta of the electron strongly tied to the internuclear axis of NO. The orbital motion is strongly coupled to the internuclear axis and the spin motion is strongly coupled to that via the

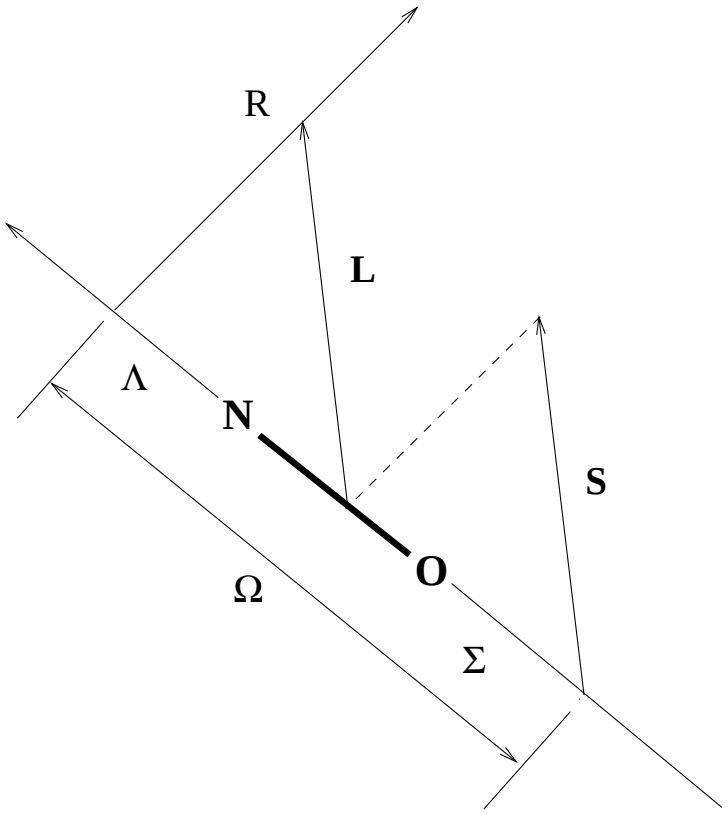

Figure 3.2: The Hund's case a coupling scheme for angular momenta in a linear molecule, where $\Omega = \Lambda + \Sigma$.

spin-orbit interaction and hence to the NO axis. For Hund's case a type coupling we require that the spin-orbit interaction, ζ, be much larger than the rotational constant, B_J. For the complex, for NO B=1.696cm^{-1} and ζ=123.16cm^{-1}, indicating that Hund's case a will model the system well. However we have no information on how the coupling scheme will change in the complex and starting from a known position provides the obvious course. The angular momenta couple as

$$\mathbf{J} = \mathbf{R} + \mathbf{L} + \mathbf{S} \tag{3.4}$$

where **R**, the rotational angular momentum, is defined in terms of **J**, the total angular momentum, **L**, the orbital angular momentum with a projection of Λ onto the NO axis, and **S**, the spin angular

momentum with a projection of Σ onto the NO axis.

Using the two axis systems within the complex as illustrated in Figure 3.1 we can formulate a set of basis functions. A simple product wavefunction is then used to describe the basis set where **J** is quantized in the principal axis system and **L** and **S** are quantized in the NO axis system.

$$|\eta\Lambda; \mathbf{S}\Sigma; \mathbf{J}M_J K_a\rangle = |\eta\Lambda\rangle|\mathbf{S}\Sigma\rangle|\mathbf{J}M_J K_a\rangle \tag{3.5}$$

where η labels the vibronic state, and M_J is the projection of the total angular momentum of the complex(excluding nuclear spin), **J**, onto an arbitrary spaced fixed axis. Note that the rotational part of the wavefunction is quantised in a different axis system to the orbital and spin parts of the wavefunction, which is not a problem as a complete basis set is used. NO-HF has a near prolate symmetric top structure so K_a is the projection of **J** onto the a principal a axis.

The representation of the symmetric rotor part of the wavefunction requires a K_a dependent choice of phase. The convention adopted is that of Brink and Satchler.[7]

$$|\boldsymbol{J}M_J K_a\rangle = \left[\frac{2J+1}{8\pi^2}\right]^{\frac{1}{2}} D^{(J)*}_{M_J K_a}(\alpha, \beta, \gamma) \tag{3.6}$$

where D is a rotation matrix with Euler angles α, β and γ. The orbital wavefunctions selected are taken to be linear combinations of spherical harmonics to be consistent with this.

$$|\eta\Lambda\rangle = \sum_L a_L Y_{L,\Lambda}(\theta_i, \phi_i) \tag{3.7}$$

where the spherical harmonics, $Y_{L,\Lambda}(\theta_i, \phi_i)$, are as tabulated by Edmonds.[8] The subscript i is appended to denote an electronic coordinate and distinguish them from the structural angle, θ.

3.2.1 Symmetry with respect to space fixed inversion

The overall symmetry of the wavefunction with respect to space-fixed inversion, referred to as parity, is a tool that it is necessary to use in factorising the fine structure matrix. The Hamiltonian

is symmetric with respect to this operation and thus the wavefunctions can only interact with states of the same parity. The fine structure matrix can be divided into two blocks which are almost identical in energy but are of opposite parity. The spectroscopic transitions that are observed all occur between states of opposite symmetry because the electric dipole operator is antisymmetric with respect to inversion.

It can be shown that by considering the effects of the space-fixed inversion operator, i_{sp}, as made up of a rotation of 180° with a reflection in a plane perpendicular to the axis of the rotation,[9] that the symmetry of the orbital and electronic parts of the wavefunction are

$$i_{sp}|\eta\Lambda\rangle = (-1)^{\Lambda+s}|\eta\,-\Lambda\rangle \tag{3.8}$$

$$i_{sp}|S\Sigma\rangle = (-1)^{S-\Sigma}|S\,-\Sigma\rangle \tag{3.9}$$

where s=1 for Σ^- states or s=0 for all other states.

The rotational part of the wavefunction can be considered in terms of the effect on the direction cosine matrix that comprises the wavefunction. The result is

$$i_{sp}|JK_aM_J\rangle = (-1)^{J-K_a}|J\,-K_aM_J\rangle \tag{3.10}$$

The inversion operation has no effect on either the vibrational part of the wavefunction or the nuclear spin contributions so the symmetry of the whole wavefunction with respect to space-fixed inversion is thus

$$i_{sp}|\eta\Lambda;S\Sigma;JK_aM_J\rangle = (-1)^{\Lambda+s+S-\Sigma+J-K_a}|\eta\,-\Lambda;S\,-\Sigma;J\,-K_aM_J\rangle \tag{3.11}$$

The wavefunctions in these system are often expressed in symmetrised form

$$\begin{aligned}|\eta\Lambda;S\Sigma;JK_aM_J;\pm\rangle = \frac{1}{\sqrt{2}}\big\{&|\eta\Lambda;S\Sigma;JK_aM_J\rangle \pm \\ &(-1)^{\Lambda+s+S-\Sigma+J-K_a}|\eta\,-\Lambda;S\,-\Sigma;J\,-K_aM_J\rangle\big\}\end{aligned} \tag{3.12}$$

3.3 The Molecular Hamiltonian

The molecular Hamiltonian relevant for the microwave experiment consists of the following terms.

$$H_{total} = H_{rot} + H_{so} + H_q + H_{sr} + H_{hf} \tag{3.13}$$

These terms represent the rotational, spin-orbit, orbital quenching, spin-rotation and hyperfine contributions to the energy levels. Centrifugal distortion effects have been dropped to reduce the complexity of the Hamiltonian. This is justified because only the lower J states of the complex NO-HF have been observed, where centrifugal distortion will be small so that it is not necessary to include it. If it becomes necessary to the analysis then the theory could be extended to include centrifugal distortion.

The forms of each of the above operators will now be derived, except the hyperfine contribution which is discussed in Chapter 4.

3.4 Rotational Hamiltonian

The rotational Hamiltonian for a molecule which possesses both rotational and electronic angular momentum can be written as[9]

$$\begin{aligned} H_{rot} =& AR_a^2 + BR_b^2 + CR_c^2 \\ =& A(J_a - L_a - S_a)^2 + B(J_b - L_b - S_b)^2 + C(J_c - L_c - S_c)^2 \end{aligned} \tag{3.14}$$

where A, B and C are the conventional rotational constants. However, **L** and **S** are quantized along the NO internuclear axis and must be rotated into the principal axis system. H_{rot} needs to be expanded with the aid of the equations in relationship 3.1 which convert the operators **L** and **S** to the NO axis system. A form of the Hamiltonian suitable for evaluation of matrix elements is then produced, with the final, somewhat complex result given below;

$$
\begin{aligned}
H_{rot} = & \left\{ A - \frac{1}{2}(B+C) \right\} J_a^2 + \frac{1}{2}(B+C)J^2 + \frac{1}{4}(B-C)\left(J^{+^2} + J^{-^2} \right) \\
& + \frac{1}{2}(B-A)\sin\theta\cos\theta\left\{ [L^+, L_z]^+ [L^-, L_z]^+ + [S^+, S_z]^+ + [S^-, S_z]^+ \right\} \\
& + AJ_a \sin\theta\{L^+ + L^- + S^+ + S^-\} - 2AJ_a\cos\theta\{L_z + S_z\} \\
& + \frac{1}{4}(A\sin^2\theta + B\cos^2\theta - C)\left\{ L^{+^2} + L^{-^2} + S^{+^2} + S^{-^2} \right\} \\
& + \frac{1}{4}(A\sin^2\theta + B\cos^2\theta + C)\left\{ [L^+, L^-]^+ + [S^+, S^-]^+ \right\} \\
& + (B-A)\sin\theta\cos\theta\left\{ (L^+ + L^-)S_z + (S^+ + S^-)L_z \right\} \\
& - \frac{1}{2}(B\cos\theta + C)\{J^+L^- + J^-L^+ + J^+S^- + J^-S^+\} \\
& - \frac{1}{2}(B\cos\theta - C)\{J^+L^+ + J^-L^- + J^+S^+ + J^-S^-\} \\
& + \frac{1}{2}(A\sin^2\theta + B\cos^2\theta + C)\{L^+S^- + L^-S^+\} \\
& + \frac{1}{2}(A\sin^2\theta + B\cos^2\theta - C)\{L^+S^+ + L^-S^-\} \\
& - B\sin\theta\{J^+L_z + J^+S_z + J^-L_z + J^-S_z\} \\
& + (A\cos^2\theta + B\sin^2\theta)\{L_z^2 + S_z^2\} \\
& + 2(A\cos^2\theta + B\sin^2\theta)\{L_z S_z\}
\end{aligned}
\tag{3.15}
$$

It is possible to neglect many of the terms within this Hamiltonian because they do not influence the energies of the transitions between rotational levels. They have a constant contribution to all levels within the $^2\Pi$ ground state manifold. These are the anticommutators $[L^+, L^-]^+$, and $[S^+, S^-]^+$, and the operators L_z^2 and S_z^2. In addition, in a $^2\Pi$ state there are no non-vanishing matrix elements off-diagonal in Σ by ± 2 as this would involve changing to a value of **S** greater than that allowed. The anti-commutators $[S^\pm, S_z]^+$ yield zero matrix elements for the $^2\Pi$ state$\left(\Sigma = \pm\frac{1}{2}, \boldsymbol{S} = \frac{1}{2}\right)$.

The matrix elements of the rotational fine structure Hamiltonian can be found in Appendix A.

3.5 Spin-Orbit Hamiltonian

This takes the simple approximate form[9, 10] for the phenomological spin-orbit interaction,

$$H_{so} = \zeta \boldsymbol{L}.\boldsymbol{S} \tag{3.16}$$

which can only connect states of the same multiplicity. It is expanded by substituting for **L** and **S**,

$$H_{so} = \zeta L_z S_z + \frac{1}{2}\zeta(L^+S^- + L^-S^+) \tag{3.17}$$

which when applied to the wavefunction gives the diagonal matrix element

$$\langle JK\Lambda\Sigma|H_{so}|J'K'\Lambda'\Sigma'\rangle = \zeta\Lambda\Sigma \tag{3.18}$$

which is incorporated into the diagonal matrix element for the rotational Hamiltonian. The coupling of other electronic states is much less important and is considered later.

3.6 Quenching

In the theory so far it has been assumed that the NO within the complex has axial symmetry for the orbital motion of the unpaired electron about the internuclear NO axis. The presence of the HF molecule will present a barrier to the free orbital motion of the unpaired electron removing the degeneracy of the Π_x and Π_y orbitals. A suitable model to describe this effect is required as it is not observed in conventional non-linear polyatomic molecules because in this case it is almost always true that the orbital angular momentum is fully quenched. The closest approximation to this can be found in the spectra of linear triatomic molecules, which because of the bending modes can lose the degeneracy of the in plane and out of plane of orbitals, for example in NCO.[11] The effect is called the Renner-Teller effect. In the conventional case, the Renner-Teller effect is expanded as a function of the bending coordinate but the structure in

the complex is permanently bent to give a constant effect. It is therefore modelled by a series expansion in the azimuthal angle of the odd electron about the NO axis, ϕ_i, as defined by the orbital basis set.

$$H_Q = \epsilon_1 \cos\phi_i + \epsilon_2 \cos 2\phi_i + \ldots\ldots \tag{3.19}$$

This expansion contains the correct symmetry with respect to reflection in the molecular plane. The expansion coefficients will be functions of the van der Waals bond length and the structural angle.

The second term is the most important because its action is diagonal within the $^2\Pi$ manifold. Its matrix elements are deduced from the form of the orbital function to be

$$\langle \Lambda = \pm 1 | \epsilon_2 \cos 2\phi_i | \Lambda = \mp 1 \rangle = -\frac{1}{2}\epsilon_2 \tag{3.20}$$

The first term of the expansion connects the $^2\Pi$ ground state to other electronic states differing in Λ by ± 1, that is to $^2\Sigma$ and $^2\Delta$ states, which will be much higher in energy and will have only a small effect on the energy The $\epsilon_1 \cos\phi_i$ term can connect the $\Lambda = \pm 1$ states in second order but functionally is the same as the matrix elements of the second term and therefore is indistinguishable from it.

In a linear molecule the wavefunction is expressed as a linear combination of the Π_x and Π_y orbitals.

$$\Pi_\pm = \frac{1}{\sqrt{2}}(\Pi_x \pm \Pi_y) \tag{3.21}$$

The pseudo Renner-Teller parameter represents the shift in energy of the Π_x and Π_y orbitals relative to one another. In the scheme used a positive value of the Renner-Teller parameter indicates that the orbital in the plane of the complex, the A' orbital, Π_x, has been shifted to a higher energy than the orbital out of the plane, the A'' orbital, Π_y, of the complex. The value of this parameter gives an important indication as to the nature of the interaction between the components of the complex.

3.7 Terms Off-Diagonal in Orbital Angular Momentum

Within the rotational Hamiltonian there are terms containing L^+ and L^- which mix the $^2\Pi$ ground state with the $^2\Sigma^+$,$^2\Sigma^-$ and $^2\Delta$ excited electronic states. In theory an exact treatment would require the inclusion of all the electronic states of the given types. The interaction of these states can be treated by degenerate perturbation theory. However it leads to a large number of constants which have little effect on the fit. It was therefore decided to model such effects as the Λ-doubling by including a single $^2\Sigma^-$ state in the Hamiltonian matrix.[12] The interactions that arise involve either a $\Lambda = \pm 1$ state in the $^2\Pi$ manifold connected with itself via the excited state, or a cross term between the states $\Lambda = +1$ and $\Lambda = -1$. As a result of the symmetry properties of the orbital wavefunction, the matrix elements of the cross terms involving the states $^2\Sigma^+$ and $^2\Sigma^-$ have opposite signs, that is they are parity dependent.

The evaluation of the matrix elements of the rotational and spin-orbit Hamiltonians require some definitions.

$$\begin{aligned}
\langle \Lambda = 1 | AL^+ | \Lambda' = 0 \rangle =& \langle A^+ \rangle \\
\langle \Lambda = 0 | AL^- | \Lambda' = 1 \rangle =& \langle A^+ \rangle \\
\langle \Lambda = -1 | AL^+ | \Lambda' = 0 \rangle =& (-1)^S \langle A^+ \rangle \\
\langle \Lambda = 0 | AL^+ | \Lambda' = -1 \rangle =& (-1)^S \langle A^+ \rangle
\end{aligned} \tag{3.22}$$

with similar relationships for $\langle B^+ \rangle$, $\langle C^+ \rangle$ and $\langle \zeta^+ \rangle$. It is assumed that the rotational constants and trigonometric functions of θ are not operators on the excited vibronic wavefunctions that appear in the perturbation expression modelled by the single excited $^2\Sigma^-$ state. The approximation may not be very good but it avoids the introduction of a large number of empirical parameters which would be difficult to estimate and fit. The Renner-Teller term can connect states that differ in electronic state but it was decided that their effect would not be significant and were neglected. The matrix elements can be found in Appendix A.

3.8 The Fine Structure Matrix

The complexity of the interactions within the fine structure of the NO-HF complex makes it difficult to understand the effect that variation of a particular parameter may have on the resultant energy produced by the diagonalisation procedure. This is exacerbated because of the large values which are obtained for some of the off-diagonal elements. A simple procedural simplification can be carried out to show how terms occur in the final matrix and what effect they have on the energy and the dominant constituents in the final wavefunction.

The fine structure Hamiltonian matrix in the absence of any spin-rotation terms or Λ-doubling terms is given in Table 3.1. Where the following substitutions have been used to simplify the matrix,

$$\begin{aligned} E_{rot} =& \left\{ A - \frac{1}{2}(B+C) \right\} K_a^2 + \frac{1}{2}(B+C)J(J+1) \\ \zeta' =& 2A\sin^2\theta + 2B\cos^2\theta + \zeta \\ \frac{\epsilon_2'}{2} =& \frac{\epsilon_2}{2} + \frac{1}{2}\{A\sin^2\theta + B\cos^2\theta - C\} \end{aligned} \tag{3.23}$$

Inspecting the matrix in Table 3.1 it is clear the the matrix can be divided into two sub-blocks which reflect the parity of the wavefunctions. By taking linear combinations of the form $|K_a, \Omega\rangle \pm |-K_a, -\Omega\rangle$, as found in Equation 3.12. The absolute parity can be determined by using the symmetry of the wavefunction with respect to space-fixed inversion as found in Section 3.2.1. The basis has been simplified because terms where $K_a > |\frac{1}{2}|$ have been excluded.

The matrix can then be reformulated as in Table 3.2 where the matrix is divided into its parity blocks.

Parity	+	-
	$\psi_1 = \frac{1}{\sqrt{2}}\left\{\left\|\frac{1}{2},\frac{1}{2}\right\rangle + \left\|-\frac{1}{2},-\frac{1}{2}\right\rangle\right\}$	$\psi_2 = \frac{1}{\sqrt{2}}\left\{\left\|\frac{1}{2},\frac{1}{2}\right\rangle - \left\|-\frac{1}{2},-\frac{1}{2}\right\rangle\right\}$
	$\psi_3 = \frac{1}{\sqrt{2}}\left\{\left\|\frac{1}{2},-\frac{1}{2}\right\rangle - \left\|-\frac{1}{2},\frac{1}{2}\right\rangle\right\}$	$\psi_4 = \frac{1}{\sqrt{2}}\left\{\left\|\frac{1}{2},-\frac{1}{2}\right\rangle + \left\|-\frac{1}{2},\frac{1}{2}\right\rangle\right\}$
	$\psi_5 = \frac{1}{\sqrt{2}}\left\{\left\|\frac{1}{2},\frac{3}{2}\right\rangle - \left\|-\frac{1}{2},-\frac{3}{2}\right\rangle\right\}$	$\psi_6 = \frac{1}{\sqrt{2}}\left\{\left\|\frac{1}{2},\frac{3}{2}\right\rangle + \left\|-\frac{1}{2},-\frac{3}{2}\right\rangle\right\}$
	$\psi_7 = \frac{1}{\sqrt{2}}\left\{\left\|\frac{1}{2},-\frac{3}{2}\right\rangle + \left\|-\frac{1}{2},\frac{3}{2}\right\rangle\right\}$	$\psi_8 = \frac{1}{\sqrt{2}}\left\{\left\|\frac{1}{2},-\frac{3}{2}\right\rangle - \left\|-\frac{1}{2},\frac{3}{2}\right\rangle\right\}$

	$\vert -\frac{1}{2},-\frac{3}{2}\rangle$	$\vert -\frac{1}{2},-\frac{1}{2}\rangle$	$\vert -\frac{1}{2},\frac{1}{2}\rangle$	$\vert -\frac{1}{2},\frac{3}{2}\rangle$	$\vert\frac{1}{2},-\frac{3}{2}\rangle$	$\vert\frac{1}{2},-\frac{1}{2}\rangle$	$\vert\frac{1}{2},\frac{1}{2}\rangle$	$\vert\frac{1}{2},\frac{3}{2}\rangle$
$\vert -\frac{1}{2},-\frac{3}{2}\rangle$	$E_{rot}+\frac{1}{2}\zeta'$ $-\frac{3}{2}A\cos\theta$	$-\frac{1}{2}A\sin\theta$ $-(B-A)$ $.\sin\theta\cos\theta$	$-\frac{1}{2}\epsilon'_2$	0	$\frac{3}{2}B\sin\theta$ $.(J+\frac{1}{2})$	$-(B\cos\theta+C)$ $.\frac{1}{2}(J+\frac{1}{2})$	0	0
$\vert -\frac{1}{2},-\frac{1}{2}\rangle$		$E_{rot}-\frac{1}{2}\zeta'$ $-\frac{1}{2}A\cos\theta$	0	$-\frac{1}{2}\epsilon'_2$	$-(B\cos\theta-C)$ $.\frac{1}{2}(J+\frac{1}{2})$	$\frac{1}{2}B\sin\theta$ $.(J+\frac{1}{2})$	0	0
$\vert -\frac{1}{2},\frac{1}{2}\rangle$			$E_{rot}-\frac{1}{2}\zeta'$ $+\frac{1}{2}A\cos\theta$	$-\frac{1}{2}A\sin\theta$ $+(B-A)$ $.\sin\theta\cos\theta$	0	0	$-\frac{1}{2}B\sin\theta$ $.(J+\frac{1}{2})$	$-(B\cos\theta+C)$ $.\frac{1}{2}(J+\frac{1}{2})$
$\vert -\frac{1}{2},\frac{3}{2}\rangle$				$E_{rot}+\frac{1}{2}\zeta'$ $+\frac{3}{2}A\cos\theta$	0	0	$-(B\cos\theta-C)$ $.\frac{1}{2}(J+\frac{1}{2})$	$-\frac{3}{2}B\sin\theta$ $.(J+\frac{1}{2})$
$\vert\frac{1}{2},-\frac{3}{2}\rangle$					$E_{rot}+\frac{1}{2}\zeta'$ $+\frac{3}{2}A\cos\theta$	$\frac{1}{2}A\sin\theta$ $-(B-A)$ $.\sin\theta\cos\theta$	$-\frac{1}{2}\epsilon'_2$	0
$\vert\frac{1}{2},-\frac{1}{2}\rangle$						$E_{rot}-\frac{1}{2}\zeta'$ $+\frac{1}{2}A\cos\theta$	0	$-\frac{1}{2}\epsilon'_2$
$\vert\frac{1}{2},\frac{1}{2}\rangle$							$E_{rot}-\frac{1}{2}\zeta'$ $-\frac{1}{2}A\cos\theta$	$\frac{1}{2}A\sin\theta$ $+(B-A)$ $.\sin\theta\cos\theta$
$\vert\frac{1}{2},\frac{3}{2}\rangle$								$E_{rot}+\frac{1}{2}\zeta'$ $-\frac{3}{2}A\cos\theta$

Table 3.1: The main elements in the Hamiltonian matrix for NO-HF

Only the upper left quadrant of the matrix needs to be considered because in the absence of Λ-doubling the energies of the parity sub-blocks are identical. A preliminary examination would lead to the expectation that the lowest energy level would be dominated by the ψ_1 state because it contains both $-\frac{1}{2}\zeta'$ and $-\frac{1}{2}A\cos\theta$ on the diagonal. However in the event of a large Renner-Teller parameter, as observed in NO-HF,[13] the ψ_1 state will mix with ψ_7 and ψ_4 will mix with ψ_6. Assuming complete mixing, the linear combination of ψ_1 and ψ_7 will have an $A\cos\theta$ term whereas the ψ_4/ψ_6 combination will have a $-A\cos\theta$ term making it lower in energy. There is thus some value of the Renner-Teller parameter at which the energies of the states approach and eventually change order.

The $\frac{1}{2}(B\cos\theta - C)(J+\frac{1}{2})$ term is important because it mediates the J dependent mixing of the states which will control some of the J dependence of the hyperfine parameters, which is illustrated in Chapter 5.

The dominant off-diagonal terms will depend on the magnitude of the ϵ_2' term, which is dominated by the Renner-Teller parameter, ϵ_2. If the value of ϵ_2 is small then the lowest energy level will be that created from ψ_1. However if ϵ_2 is large, as in NO-HF, then a combination of ψ_4 and ψ_6 will take place which will become lower in energy. Note must be taken of those terms which depend on $(J+\frac{1}{2})$ whose influence becomes significant when the hyperfine terms are considered.

	ψ_1	ψ_4	ψ_6	ψ_7	ψ_2	ψ_3	ψ_5	ψ_8
ψ_1	$E_{rot} - \frac{1}{2}\zeta'$ $-\frac{1}{2}A\cos\theta$	$\frac{1}{2}B\sin\theta(J+\frac{1}{2})$	$\frac{1}{2}A\sin\theta$ $+(B-A)$ $.\sin\theta\cos\theta$	$-\frac{1}{2}\epsilon_2'-$ $\frac{1}{2}(B\cos\theta-C)$ $.(J+\frac{1}{2})$	0	0	0	0
ψ_3		$E_{rot} - \frac{1}{2}\zeta'$ $+\frac{1}{2}A\cos\theta$	$-\frac{1}{2}\epsilon_2'+$ $\frac{1}{2}(B\cos\theta-C)$ $.(J+\frac{1}{2})$	$\frac{1}{2}A\sin\theta$ $-(B-A)$ $.\sin\theta\cos\theta$	0	0	0	0
ψ_5			$E_{rot} + \frac{1}{2}\zeta'$ $-\frac{3}{2}A\cos\theta$	$-\frac{3}{2}B\sin\theta(J+\frac{1}{2})$	0	0	0	0
ψ_7				$E_{rot} + \frac{1}{2}\zeta'$ $+\frac{3}{2}A\cos\theta$	0	0	0	0
ψ_2					$E_{rot} - \frac{1}{2}\zeta'$ $-\frac{1}{2}A\cos\theta$	$-\frac{1}{2}B\sin\theta(J+\frac{1}{2})$	$\frac{1}{2}A\sin\theta$ $+(B-A)$ $.\sin\theta\cos\theta$	$-\frac{1}{2}\epsilon_2'+$ $\frac{1}{2}(B\cos\theta-C)$ $.(J+\frac{1}{2})$
ψ_4						$E_{rot} - \frac{1}{2}\zeta'$ $+\frac{1}{2}A\cos\theta$	$-\frac{1}{2}\epsilon_2'-$ $\frac{1}{2}(B\cos\theta-C)$ $.(J+\frac{1}{2})$	$\frac{1}{2}A\sin\theta$ $-(B-A)$ $.\sin\theta\cos\theta$
ψ_6							$E_{rot} + \frac{1}{2}\zeta'$ $-\frac{3}{2}A\cos\theta$	$\frac{3}{2}B\sin\theta(J+\frac{1}{2})$
ψ_8								$E_{rot} + \frac{1}{2}\zeta'$ $+\frac{3}{2}A\cos\theta$

Table 3.2: The Hamiltonian matrix with states of the same parity coupled into each other and divided into parity blocks.

References

[1] P. D. A. Mills, C. M. Western, B. J. Howard. *J. Phys. Chem.*, **90**, 2991, (1986).

[2] W. M. Fawzy, M. C. Heaven. *J. Chem. Phys.*, **89**, 7030, (1988).

[3] J. M. Brown, B. J. Howard. *Mol. Phys.*, **31**, 1517, (1976).

[4] J. H. Van Vleck. *Rev. Mod. Phys.*, **23**, 213, (1951).

[5] R. A. Frosch, H. M. Foley. *Phys. Rev*, **88**, 1337, (1952).

[6] R. S. Mulliken, A. Christy. *Phys. Rev*, **38**, 87, (1931).

[7] D. M. Brink, G. R. Satchler. *Angular Momentum*. Clarendon Press, Oxford, (1979).

[8] A. R. Edmonds. *Angular Momentum in Quantum Mechanics*. Princeton University Press, Princeton, NJ, (1974).

[9] R. N. Zare. *Angular Momentum: Understanding Spatial Aspects of Physics and Chemistry*. Wiley, New York, (1988).

[10] W. H. Flygare. *Molecular Structure and Dynamics*. Prentice-Hall, Englewood Cliffs, (1978).

[11] A. Carrington, A. R. Fabris, B. J. Howard, N. J. D. Lucas. *Mol. Phys.*, **20**, 961, (1971).

[12] E. Miescher. *J. Chem. Phys.*, **73**, 3088, (1980).

[13] W. M. Fawzy, G. T. Frazer, J. T. Hougen. *J. Chem. Phys*, **93**, 2992, (1990).

Chapter 4

Hyperfine Interactions

To see a world in a grain of sand
And heaven in a wild flower
Hold infinity in the palm of your hand
And eternity in an hour
-W. Blake Augaries of Innocence

The theory for the hyperfine spectrum of NO-HF is based on that of NO which has been extensively studied for many years. The earliest observations of the microwave spectrum spectrum of nitric oxide were by Beringer and Castle[1] in 1950. An effective model for the hyperfine interaction was developed by Frosch and Foley[2] who represented the fields due to the electron and the nitrogen nucleus(I=1) as vector potentials. Subsequently many people have considered the problem[3–8] and the related problem of OH.[9, 10]

NO-HF exhibits a number of extensions to the hyperfine theory of NO because there are two other nuclei in the molecule which have magnetic moments and are able to couple to the unpaired electron.[11] Here the Hamiltonian is derived in terms of irreducible spherical tensors which simplify the calculations and allow the use standard transformations which can be found in any text on angular momentum[12–15] and are listed for convenience in Appendix C.

4.1 Nitrogen Magnetic Hyperfine

There are two magnetic moments associated with the unpaired electron that can interact with the magnetic moment of a nuclear spin. Solving the Hamiltonian for this[2] gives rise to three different terms. They occur for the orbital motion of the electron, $T^1(\boldsymbol{L})$, the electron spin, $T^1(\boldsymbol{S}, \boldsymbol{C^2})$, where C^2 is a modified spherical harmonic representing the spatial relationship between the nitrogen nucleus and the electron, and a Fermi contact term due to the presence of electron density at the nitrogen nucleus, $T^1_p(\boldsymbol{S})$. The Hamiltonian is given by,

$$\begin{aligned} H_{mag,N} =& T^1(\boldsymbol{I_N}).\Bigg(2g_I\mu_B\mu_I T^1(\boldsymbol{L}) + \frac{8\pi}{3}g_e g_I\mu_B\mu_I|\psi(r=0)^2|T^1(\boldsymbol{S}) \\ & - \sqrt{10}g_e g_I\mu_B\mu_I\frac{1}{r^3}T^1(\boldsymbol{S}, \boldsymbol{C^2})\Bigg) \\ =& T^1(\boldsymbol{I_N}).T^1(\boldsymbol{X}) \end{aligned} \tag{4.1}$$

The term $T^1(\boldsymbol{X})$ is introduced to denote the sum of the three other first rank tensor operators.

The matrix element to be found is thus

$$\begin{aligned} &\langle \eta\Lambda; S\Sigma; JK_a; I_N F_N|H_{mag,N}|\eta\Lambda'; S'\Sigma'; J'K'_a; I_N F'_N\rangle \\ &\quad = \delta_{F_N,F'_N}\delta_{M_{F_N},M'_{F_N}}(-1)^{J'+I_N+F_N}\begin{Bmatrix} J & I_N & F_N \\ I_N & J' & 1 \end{Bmatrix} \\ &\qquad \langle I_N\|T^1(\boldsymbol{I_N})\|I'_N\rangle\langle \eta\Lambda; S\Sigma; JK_a\|T^1(\boldsymbol{X})\|\eta\Lambda'; S'\Sigma'; J'K'_a\rangle \end{aligned} \tag{4.2}$$

Having performed this separation we now need to determine the values of the reduced matrix elements. If the reduced matrix element of the nuclear spin is taken and starting from the unreduced spin matrix element. A Wigner-Eckart reduction is performed to produce

$$\langle I_1 M_{I_1}|T^1_0(\boldsymbol{I_1})|I_1 M_{I_1}\rangle = (-1)^{I_1-M_{I_1}}\begin{pmatrix} I_1 & 1 & I_1 \\ -M_{I_1} & 0 & M_{I_1} \end{pmatrix}\langle I_1\|T^1(\boldsymbol{I_1})\|I_1\rangle \tag{4.3}$$

We also have the value of the $T^1_0(\boldsymbol{I}_1)$ operator.

$$\langle I_1 M_{I_1}|T^1_0(\boldsymbol{I_1})|I_1 M_{I_1}\rangle = M_{I_1} \tag{4.4}$$

The value of the three-j symbol is given by

$$(-1)^{I_1-M_{I_1}}\begin{pmatrix} I_1 & 1 & I_1 \\ -M_{I_1} & 0 & M_{I_1}\end{pmatrix} = (-1)^{I_1-I_1}\frac{2M_{I_1}}{\left[(2I_1+2)(2I_1+1)(2I_1)\right]^{\frac{1}{2}}} \tag{4.5}$$

When the two results for $\langle I_1 M_{I_1}|T_0^1(\boldsymbol{I}_1)|I_1 M_{I_1}\rangle$ are equated and rearranged we obtain the following expression for the reduced matrix element.

$$\langle I_N\|T^1(\boldsymbol{I_N})\|I_N\rangle = [I_N(I_N+1)(2I_N+1)]^{\frac{1}{2}} \tag{4.6}$$

Next we have the reduced matrix element of the other angular momenta,

$$\langle \eta\Lambda; S\Sigma; JK_a\|T^1(\boldsymbol{X})\|\eta\Lambda'; S'\Sigma'; J'K_a'\rangle \tag{4.7}$$

The tensor operator in the reduced matrix element of the electron's magnetic moments is currently quantised in the space-fixed axis system. However the total rotational angular momentum, J, is quantised in the molecule fixed-axis system. The operator, $T_p^1(\boldsymbol{X})$, must be rotated by

$$T_p^1(\boldsymbol{X}) = \sum_q D_{pq}^{1*}(\omega)T_q^1(\boldsymbol{X}) \tag{4.8}$$

In order to calculate the form of the reduced matrix element the unreduced matrix element is required

$$\begin{aligned}&\langle \eta\Lambda; S\Sigma; JK_aM|T_p^1(\boldsymbol{X})|\eta\Lambda'; S'\Sigma'; J'K_a'M'\rangle \\ &\qquad = (-1)^{J-M}\begin{pmatrix} J & 1 & J' \\ -M & p & M'\end{pmatrix}\langle \eta\Lambda; S\Sigma; JK_a\|T^1(\boldsymbol{X})\|\eta\Lambda'; S'\Sigma'; J'K_a'\rangle\end{aligned} \tag{4.9}$$

On taking the same matrix element and applying a rotation from the space fixed to molecule fixed coordinates.

$$\begin{aligned}&\langle \eta\Lambda; S\Sigma; JK_aM|T_p^1(\boldsymbol{X})|\eta\Lambda'; S'\Sigma'; J'K_a'M'\rangle \\ &\qquad = \sum_q \langle JK_aM|D_{pq}^{1*}(\omega)|J'K_a'M'\rangle\langle \eta\Lambda; S\Sigma|T_q^1(\boldsymbol{X})|\eta\Lambda'; S'\Sigma'\rangle\end{aligned} \tag{4.10}$$

Taking the matrix element of the rotation matrix and substituting for the wavefunction as defined in Equation 3.6. The result is the integral over three rotation matricies.

$$\begin{aligned}\langle JK_aM|D^{1*}_{pq}(\omega)|J'K'_aM'\rangle \\ =&\frac{1}{8\pi^2}\big[(2J+1)(2J'+1)\big]^{\frac{1}{2}} \\ &\times\int D^{J}_{MK_a}(\omega)(-1)^{p-q}D^{1*}_{-p-q}(\omega)(-1)^{M'-K'_a}D^{J'*}_{-M'-K'_a}(\omega)d\tau\end{aligned} \tag{4.11}$$

Integrating the rotation matrices equation becomes,

$$\begin{aligned}\langle JK_aM|D^{1*}_{pq}(\omega)|J'K'_aM'\rangle \\ &= (-1)^{M-K_a}\big[(2J+1)(2J'+1)\big]^{\frac{1}{2}}\begin{pmatrix}J & 1 & J'\\ -M & p & M'\end{pmatrix}\begin{pmatrix}J & 1 & J'\\ -K_a & q & K'_a\end{pmatrix}\end{aligned} \tag{4.12}$$

Substituting back into Equation 4.10

$$\begin{aligned}\langle \eta\Lambda;S\Sigma;JK_aM|T^1_p(\boldsymbol{X})|\eta\Lambda';S'\Sigma';J'K'_aM'\rangle \\ &=\sum_q(-1)^{M-K_a}\big[(2J+1)(2J'+1)\big]^{\frac{1}{2}}\begin{pmatrix}J & 1 & J'\\ -M & p & M'\end{pmatrix} \\ &\times\begin{pmatrix}J & 1 & J'\\ -K_a & q & K'_a\end{pmatrix}\langle \eta\Lambda;S\Sigma|T^1_q(\boldsymbol{X})|\eta\Lambda';S'\Sigma'\rangle\end{aligned} \tag{4.13}$$

Equating the two results for the matrix elements of the space fixed tensor, $T^1_p(\boldsymbol{X})$, and rearranging the resultant expression the form of the equation for the reduced matrix element is derived

$$\begin{aligned}\langle \eta\Lambda;S\Sigma;JK_a\|T^1(\boldsymbol{X})\|\eta\Lambda';S'\Sigma';J'K'_a\rangle \\ =\sum_q(-1)^{J-K_a}\big[(2J+1)(2J'+1)\big]^{\frac{1}{2}}\begin{pmatrix}J & 1 & J'\\ -K_a & q & K'_a\end{pmatrix}\langle \eta\Lambda;S\Sigma|T^1_q(\boldsymbol{X})|\eta\Lambda';S'\Sigma'\rangle\end{aligned} \tag{4.14}$$

By combining Equations 4.6 and 4.14 the expression for the complete matrix element becomes,

$$\begin{aligned}
&\langle \eta\Lambda; S\Sigma; JK_a; I_N F_N | H_{mag,N} | \eta\Lambda'; S'\Sigma'; J'K_a'; I_N F_N' \rangle \\
&= \delta_{F_N,F_N'}\delta_{M_{F_N},M_{F_N'}'}(-1)^{J'+I_N+F_N}
\begin{Bmatrix} J & I_N & F_N \\ I_N & J' & 1 \end{Bmatrix}
\left[I_N(I_N+1)(2I_N+1)\right]^{\frac{1}{2}} \\
&\left[(2J+1)(2J'+1)\right]^{\frac{1}{2}} \sum_q (-1)^{J-K_a}
\begin{pmatrix} J & 1 & J' \\ -K_a & q & K_a' \end{pmatrix}
\langle \eta\Lambda; S\Sigma | T_q^1(\boldsymbol{X}) | \eta\Lambda'; S'\Sigma' \rangle
\end{aligned} \tag{4.15}$$

The matrix elements of the type $\langle \eta\Lambda; S\Sigma | T_q^1(\boldsymbol{X}) | \eta\Lambda'; S'\Sigma' \rangle$ have to be evaluated. Before this can take place the operator must be rotated again from the molecule-fixed axis system to the NO axis system because Λ and Σ are quantised there. A planar d-matrix is used to rotate the operator

$$\sum_r d_{qr}^1(\theta) \langle \eta\Lambda; S\Sigma | T_r^1(\boldsymbol{X}) | \eta\Lambda'; S'\Sigma' \rangle \tag{4.16}$$

The $d_{qr}^1(\theta)$ can be substituted for with their standard expressions. The matrix element can be split up into its component operators as defined in equation 4.1.

4.1.1 Nuclear Spin-Orbit Interaction

The operator for this interaction was $T_p^1(\boldsymbol{L})$ which when rotated becomes

$$\langle \eta\Lambda; S\Sigma | 2g_I\mu_B\mu_I \frac{1}{r^3} T_q^1(\boldsymbol{L}) | \eta\Lambda'; S\Sigma' \rangle = \sum_r \langle \eta\Lambda; S\Sigma | 2g_I\mu_B\mu_I \frac{1}{r^3} d_{0,r}^1 T_r^1(\boldsymbol{L}) | \eta\Lambda'; S\Sigma' \rangle \tag{4.17}$$

The final matrix element of the system is

$$\begin{aligned}
&\langle \eta\Lambda; S\Sigma | 2g_I\mu_B\mu_I \frac{1}{r^3} T_q^1(L) | \eta\Lambda'; S\Sigma' \rangle \\
&\quad = \langle \eta\Lambda; S\Sigma | 2g_I\mu_B\mu_I \frac{1}{r^3} (d_{0,-1}^1 T_{-1}^1(L) + d_{0,0}^1 T_0^1(L) + d_{0,1}^1 T_1^1(L)) | \eta\Lambda'; S\Sigma' \rangle \\
&\quad = -\frac{a}{\sqrt{2}} \sin(\theta) \delta_{\Sigma,\Sigma'}\delta_{\Lambda,\Lambda'} \langle \eta\Lambda | d_{0,-1}^1 T_{-1}^1(L) | \eta\Lambda' \rangle \\
&\qquad + a\cos\theta \delta_{\Sigma,\Sigma'}\delta_{\Lambda,\Lambda'} \langle \eta\Lambda | d_{0,0}^1 T_0^1(L) | \eta\Lambda' \rangle \\
&\qquad + \frac{a}{\sqrt{2}} \sin(\theta) \delta_{\Sigma,\Sigma'}\delta_{\Lambda,\Lambda'} \langle \eta\Lambda | 2g_I d_{0,1}^1 T_1^1(L) | \eta\Lambda' \rangle
\end{aligned} \tag{4.18}$$

There are two different types of terms, those which connect states which do not differ in Λ and those which connect states different in Λ by ± 1. The states off-diagonal in Λ will connect to the Λ-doubling states which are far away in energy and will have an insignificant effect. They are therefore neglected.

The constant a is given by

$$a = 2g_I\mu_B\mu_I \left\langle \frac{1}{r^3} \right\rangle \tag{4.19}$$

4.2 Fermi Contact Interaction

The components of $T^1(\boldsymbol{S})$ in the NO axis system are generated by exactly the same series of transformations as for those of the nuclear spin-orbit interaction. The actual matrix elements are then evaluated as

$$\langle \eta\Lambda; S\Sigma | b_F T^1_q(\boldsymbol{S}) | \eta\Lambda'; S\Sigma \rangle = \sum_r d^1_{qr}(\theta) b_F . \delta_{\Lambda,\Lambda'} . (-1)^{S-\Sigma} \sqrt{S(S+1)(2S+1)} \begin{pmatrix} S & 1 & S \\ -\Sigma & r & \Sigma' \end{pmatrix} \tag{4.20}$$

The constant b_F is

$$b_F = \frac{8\pi}{3} g_e g_I \mu_B \mu_I |\psi(r=0)^2| \tag{4.21}$$

4.3 Spin-Spin Dipolar Interaction

The first rank tensor formed by coupling $T^1(\boldsymbol{S})$ to $C^2(\theta_i, \phi_i)$ is defined by the equation 4.22. where $C^2(\theta_i, \phi_i)$ is a modified spherical harmonic relating the positions of the electronic and nuclear magnetic dipoles.

$$T^1_r(\boldsymbol{S}, \boldsymbol{C}) = \sqrt{3}(-1)^{1-r} \sum_{r_1, r_2} T^1_{r_1}(\boldsymbol{S}) . C^2_{r_2}(\theta_i, \phi_i) \begin{pmatrix} 1 & 2 & 1 \\ r_1 & r_2 & -r \end{pmatrix} \tag{4.22}$$

$T^1(\boldsymbol{S},\boldsymbol{C})$ may be expressed in terms of the above components and its matrix element may thus be expanded.

$$
\begin{aligned}
&-\sqrt{10}\langle\eta\Lambda;S\Sigma|g_e g_I\mu_B\mu_I\frac{1}{r^3}T^1_q(\boldsymbol{S},\boldsymbol{C})|\eta\Lambda';S\Sigma'\rangle \\
&\qquad = -\sqrt{10}\sum_{r,r_1,r_2}\left\{\begin{array}{c}\sqrt{3}.(-1)^{1-r}\begin{pmatrix}1 & 2 & 1\\ r_1 & r_2 & -r\end{pmatrix}d^1_{q,r}(\theta)\times \\ \langle\eta\Lambda|g_e g_I\mu_B\mu_I\frac{1}{r^3}C^2_{r_2}(\theta_i,\phi_i)|\eta\Lambda'\rangle\langle S\Sigma|T^1_{r_1}(\boldsymbol{S})|S\Sigma'\rangle\end{array}\right\} \\
&\qquad =\sqrt{30}\sum_{r,r_2}\left\{\begin{array}{c}(-1)^r\begin{pmatrix}1 & 1 & 2\\ -r & r_1 & r_2\end{pmatrix}d^1_{q,r}(\theta).(-1)^{S-\Sigma}\sqrt{S(S+1)(2S+1)}. \\ \times\begin{pmatrix}S & 1 & S\\ -\Sigma & r_1 & \Sigma\end{pmatrix}\langle\eta\Lambda|g_e g_I\mu_B\mu_I\frac{1}{r^3}C^2_{r_2}(\theta_i,\phi_i)|\eta\Lambda'\rangle\end{array}\right\}
\end{aligned}
\tag{4.23}
$$

where the symmetry properties and argument constraints of the three-j symbols have been invoked. The matrix elements of $g_e g_I\mu_B\mu_I\frac{1}{r^3}C^2(\theta_i,\phi_i)$ which are diagonal in the $^2\Pi$ manifold may be described in terms of the original c and d parameters of Frosch and Foley,[2] given below. Again the terms which would link to the $^2\Sigma^-$ states have been neglected.

$$c = \frac{3}{2}g_e g_I\mu_B\mu_I\left\langle\frac{3\cos^2\theta_i-1}{r^3}\right\rangle \tag{4.24}$$

$$d = \frac{3}{2}g_e g_I\mu_B\mu_I\left\langle\frac{\sin^2\theta_i}{r^3}\right\rangle \tag{4.25}$$

From these definitions the matrix elements of $g_e g_I\mu_B\mu_I\frac{1}{r^3}C^2(\theta_i,\phi_i)$ are:

$$\langle\eta\Lambda|g_e g_I\mu_B\mu_I\frac{1}{r^3}C^2_{\pm2}(\theta_i,\phi_i)|\eta\Lambda'\rangle = -\frac{1}{\sqrt{6}}\delta_{\Lambda,\Lambda'\pm2}d \tag{4.26}$$

$$\langle\eta\Lambda|g_e g_I\mu_B\mu_I\frac{1}{r^3}C^2_{0}(\theta_i,\phi_i)|\eta\Lambda'\rangle = \frac{1}{3}\delta_{\Lambda,\Lambda'}c \tag{4.27}$$

The complete expressions for the matrix element are given in Appendix B.1.

4.4 The Electric Quadrupole Interaction.

The electric quadrupole interaction takes place between any nucleus with a spin of at least one and the electric field gradient at that nucleus, which in NO-HF exists only for the nitrogen nucleus where I=1. Nuclei with a quadrupole moment possess a non-spherical charge distribution and different orientations of the nucleus relative to the electron distribution in the molecule have different energies. The derivation of the electric quadrupole interaction is well established.[12, 16]

The Hamiltonian for this interaction is the scalar product of two tensor operators, one for the quadrupole moment of the nucleus, $T^2(\boldsymbol{Q})$, and the other for the electric field gradient, $T^2(\boldsymbol{\nabla^2 V})$.

$$H_{quad} = T^2(\boldsymbol{\nabla^2 V}).T^2(\boldsymbol{Q}) \tag{4.28}$$

where

$$T^2(\boldsymbol{\nabla^2 V}) = \sum_i \frac{e_i}{r_i^3} C^2(\theta_i, \phi_i) \tag{4.29}$$

$$T^2(\boldsymbol{Q}) = \sum_p \frac{e_p}{r_p^3} C^2(\theta_p, \phi_p) \tag{4.30}$$

The subscript i denotes electronic coordinates and the p for the coordinates of the nucleons. The matrix element is then given by the expression below which can then be simplified by using the separation of scalar products of tensor operators.

$$\begin{aligned}\langle \eta\Lambda; S\Sigma; J, K_a; I_N, &F_N, M_{F_N} | H_{quad} | \eta\Lambda'; S\Sigma'; J', K_a'; I_N, F_N', M_{F_N'} \rangle \\ &= \delta_{F_N, F_N'} \delta_{M_{F_N}, M_{F_N'}} (-1)^{J'+I_N+F_N} \begin{Bmatrix} J & I_N & F_N \\ I_N & J' & 2 \end{Bmatrix} \\ &\quad \langle I_N \| T^2(\boldsymbol{Q}) \| I_N \rangle \langle \eta\Lambda; S\Sigma; J, K_a \| T^2(\boldsymbol{\nabla^2 V}) \| \eta\Lambda'; S\Sigma'; J', K_a' \rangle\end{aligned} \tag{4.31}$$

It now becomes necessary to deal with the two reduced matrix elements that this operation has generated. Firstly taking the reduced matrix element of the quadrupole moment operator with

the nuclear spin. In order to derive an expression for the reduced matrix element we need to start with the unreduced matrix element and apply the Wigner-Eckart theorem.

$$\langle I_N, M_{I_N}|T^2_q(\boldsymbol{Q})|I'_N, M'_{I_N}\rangle = (-1)^{I_N - M_{I_N}} \begin{pmatrix} I_N & 2 & I'_N \\ -M_{I_N} & q & M'_{I_N} \end{pmatrix} \langle I_N \| T^2(\boldsymbol{Q}) \| I'_N \rangle \tag{4.32}$$

By using the definition of $T^2_0(\boldsymbol{Q})$ an expression for the matrix element below can be obtained in terms of the classically defined Q parameter.

$$\begin{aligned} \langle I_N, M_{I_N} = I_N|T^2_0(\boldsymbol{Q})|I_N, M'_{I_N} = I_N\rangle & \\ &= \langle I_N, M_{I_N} = I_N|\frac{1}{2}\sum_p e_p(3z_p^2 - r_p^2)|I_N, M'_{I_N} = I_N\rangle \\ &= \frac{1}{2}e\langle I_N, I_N|\sum_p(3z_p^2 - r_p^2)|I_N, I_N\rangle \\ &= \frac{1}{2}eQ \end{aligned} \tag{4.33}$$

This uses the classical definition of Q,

$$Q = \langle I_N, I_N|\sum_p(3z_P^2 - r_p^2)|I_N I_N\rangle \tag{4.34}$$

which would be equal if I and I_z were coincident. However quantum mechanical considerations indicate that this is never quite so though it will approach the value at high values of I when $M_I = I$. It is the standard convention to define this limiting case as the quadrupole moment of the nucleus. If we then take the matrix element of $T^2_0(Q)$ for M_{I_N} and separated by the Wigner-Eckart theorem we get,

$$\begin{aligned} \langle I_N, M_{I_N} = I_N|T^2_0(\boldsymbol{Q})|I_N, M'_{I_N} = I_N\rangle &= (-1)^{I_N - I_N} \begin{pmatrix} I_N & 2 & I_N \\ -I_N & 0 & I_N \end{pmatrix} \langle I_N \| T^2(Q) \| I_N \rangle \\ &= \begin{pmatrix} I_N & 2 & I_N \\ -I_N & 0 & I_N \end{pmatrix} \langle I_N \| T^2(Q) \| I_N \rangle \end{aligned} \tag{4.35}$$

By substituting $\frac{1}{2}eQ$ for the left hand side in the above and rearranging, the formula for the reduced matrix element of $T^2(Q)$ is then obtained.

$$\langle I_N \| T^2(\boldsymbol{Q}) \| I_N \rangle = \frac{\frac{1}{2}eQ}{\begin{pmatrix} I_N & 2 & I_N \\ -I_N & 0 & I_N \end{pmatrix}} \tag{4.36}$$

The 3-j symbol can be evaluated using standard tables and is given by,

$$\begin{pmatrix} I_N & 2 & I_N \\ -I_N & 0 & I_N \end{pmatrix} = \left[\frac{2I_N(2I_N-1)}{(2I_N+3)(2I_N+2)(2I_N+1)} \right]^{\frac{1}{2}} \tag{4.37}$$

Substituting this into the expression gives,

$$\langle I_N \| T^2(\boldsymbol{Q}) \| I_N \rangle = \frac{1}{2}eQ \left[\frac{(2I_N+3)(2I_N+2)(2I_N+1)}{2I_N(2I_N-1)} \right]^{\frac{1}{2}} \tag{4.38}$$

This final expression can then be substituted into equation number 4.32.

The calculation has not been completed because the reduced matrix element of the field gradient tensor needs to be determined. The field gradient is tied to the rotating molecule and needs to be evaluated in the axis system of the complex. The matrix element that is required is,

$$\langle \eta, \Lambda; S, \Sigma; J, K_a \| T^2(\boldsymbol{\nabla^2 V}) \| \eta, \Lambda'; S', \Sigma'; J', K'_a \rangle \tag{4.39}$$

The expression for this reduced matrix element can be derived by exactly the same procedure as is found between Equations 4.7 and 4.14 in the derivation of the matrix elements of the magnetic hyperfine. The result is

$$\begin{aligned} &\langle \eta, \Lambda; S, \Sigma; J, K_a \| T^2(\boldsymbol{\nabla^2 V}) \| \eta, \Lambda'; S', \Sigma'; J', K'_a \rangle \\ &= \sum_q (-1)^{J-K_a} \left[(2J+1)(2J'+1) \right]^{1/2} \begin{pmatrix} J & 2 & J' \\ -K_a & q & K'_a \end{pmatrix} \langle \Lambda S \Sigma | T^2_q(\boldsymbol{\nabla^2 V}) | \Lambda' S' \Sigma' \rangle \end{aligned} \tag{4.40}$$

This can then be substituted into the main expression for the quadrupole matrix element to leave only one unresolved term. The matrix element in the above expression.

$$\langle \Lambda S \Sigma | T^2_q(\boldsymbol{\nabla^2 V}) | \Lambda' S' \Sigma' \rangle \tag{4.41}$$

Now the components of Λ and Σ are quantized in the NO sub-molecule axis system so an additional rotation is required.

$$T_q^2(\boldsymbol{\nabla^2 V}) = \sum_r d_{qr}^2(\theta) T_r^2(\boldsymbol{\nabla^2 V}) \tag{4.42}$$

which gives

$$\sum_r d_{qr}^2(\theta) \langle \Lambda S \Sigma | T_r^2(\boldsymbol{\nabla^2 V}) | \Lambda' S' \Sigma' \rangle \tag{4.43}$$

If we examine the form of the operator $T_r^2(\boldsymbol{\nabla^2 V})$ we can demonstrate that it only acts on the orbital part of the wavefunction. The field gradient in the nucleus will not depend on the electron spin and this can therefore be eliminated to give

$$\delta_{\Sigma,\Sigma'} \sum_r d_{qr}^2(\theta) \langle \Lambda | T_r^2(\boldsymbol{\nabla^2 V}) | \Lambda' \rangle \tag{4.44}$$

It is then required that the matrix elements of $\langle \Lambda | T_r^2(\boldsymbol{\nabla^2 V}) | \Lambda' \rangle$ be evaluated. However this is not required as the results of these matrix elements are defined in the theory and are given by;

$$\langle \Lambda | T_{r=0}^2(\boldsymbol{\nabla^2 V}) | \Lambda' \rangle = \delta_{\Lambda,\Lambda'} \frac{1}{2} q_0 \tag{4.45}$$

$$\langle \Lambda | T_{r=\pm 2}^2(\boldsymbol{\nabla^2 V}) | \Lambda' \rangle = \delta_{\Lambda,\Lambda' \pm 2}, \frac{1}{2\sqrt{6}} q_2 \tag{4.46}$$

If the component parts which have been demonstrated so far are assembled then a complete equation for the electric quadrupole interaction is obtained. For $\Delta\Lambda = 0$;

$$\begin{aligned}
&\langle \eta\Lambda; S\Sigma; J, K_a; I_N, F_N, M_{F_N} | H_{quad} | \eta\Lambda'; S\Sigma'; J', K_a'; I_N, F_N', M_{F_N'} \rangle \\
&= \delta_{F_N,F_N'} \delta_{M_{F_N},M_{F_N'}'} \delta_{\Sigma,\Sigma'} (-1)^{J'+I_N+F_N} \begin{Bmatrix} J & I_N & F_N \\ I_N & J' & 2 \end{Bmatrix} \left[\frac{(2I_N+3)(2I_N+2)(2I_N+1)}{2I_N(2I_N-1)} \right]^{1/2} \\
&\quad \times \left[(2J+1)(2J'+1) \right]^{\frac{1}{2}} \sum_q (-1)^{J-K_a} \begin{pmatrix} J & 2 & J' \\ -K_a & q & K_a' \end{pmatrix} d_{q0}^2 \frac{1}{4} eQq_0
\end{aligned} \tag{4.47}$$

For $\Delta\Lambda = 2$;

$$\begin{aligned}
&\langle \eta\Lambda; S\Sigma; J, K_a; I_N, F_N, M_{F_N} | H_{quad} | \eta\Lambda'; S\Sigma'; J', K'_a; I_N, F'_N, M_{F'_N} \rangle \\
&= \delta_{F_N, F'_N} \delta_{M_{F_N}, M'_{F_N}} \delta_{\Sigma,\Sigma'} (-1)^{J'+I_N+F_N} \begin{Bmatrix} J & I_N & F_N \\ I_N & J' & 2 \end{Bmatrix} \left[\frac{(2I_N+3)(2I_N+2)(2I_N+1)}{2I_N(2I_N-1)} \right]^{\frac{1}{2}} \\
&\times \left[(2J+1)(2J'+1) \right]^{1/2} \sum_q (-1)^{J-K_a} \begin{pmatrix} J & 2 & J' \\ -K_a & q & K'_a \end{pmatrix} d^2_{q2} \frac{1}{4\sqrt{6}} eQq_2
\end{aligned} \tag{4.48}$$

Having now derived these formulae it is necessary to write the explicit forms of the matrix elements for the different values of q. These are given in full detail in Appendix B.2

4.5 Hydrogen and Fluorine Hyperfine

The appearance of the hyperfine structure for the hydrogen and fluorine nuclei was initially assumed to mimic that of the nitrogen nucleus, the interaction being simplified with the absence of any quadrupolar structure. The effect of the coupling to a second nucleus can be calculated by the use of standard transformations of angular momentum theory.

It was expected that the nuclei closest to the unpaired electron on the nitric oxide molecule would have the largest hyperfine interaction therefore nitrogen would be the strongest and fluorine the weakest. The coupling system is with the nitrogen nuclear spin, $\mathbf{I_N}$, coupled to the total angular momentum of the complex, $\mathbf{J}$, to create a resultant angular momentum, $\mathbf{F_N}$. The hydrogen nuclear spin, $\mathbf{I_H}$, then couples to the angular momentum $\mathbf{F_N}$ to generate the angular momentum $\mathbf{F_H}$ and finally the fluorine nuclear spin, $\mathbf{I_F}$, couples to that angular momentum to produce the final angular momentum $\mathbf{F}$. This coupling scheme was selected because on empirical grounds it should be a good representation of the interaction and the preliminary results indicated that it would be an effective system. The coupling scheme used as basis for describing the interactions does not need to be an accurate representation of the relative strengths of the

coupling but it is always desirable to work in a basis which is a close approximation to the real one because it minimises the magnitudes of any off-diagonal elements. The reason being that a complete basis set is always used so that the results do not depend on that basis set.

4.5.1 Hydrogen Coupling

If it is initially assumed that the interaction of the hydrogen nucleus takes the same form as that of the nitrogen nucleus which is introduced in Equation 4.1 where the tensor operator is changed to that for hydrogen. The actual form of the $T^1(\boldsymbol{X})$ may be different but will still interact with the nuclear spin tensor in the same way. Using this Hamiltonian the first thing to do is to separate the scalar product.

$$\begin{aligned}\langle \eta\Lambda; S\Sigma; JK_a; I_N F_N; I_H F_H M_{F_H} | T^1(\boldsymbol{I_H}).T^1(\boldsymbol{X}) | \eta\Lambda; S\Sigma; J'K'_a; I_N F'_N; I_H F'_H M_{F_H}\rangle \\ = (-1)^{F'_N+I_H+F_2} \begin{Bmatrix} F_N & I_H & F_H \\ I_H & F'_N & 1 \end{Bmatrix} \langle I_H||T^1(\boldsymbol{I_H})||I_H\rangle \\ \langle \eta\Lambda; S\Sigma; JK_a; I_N F_N||T^1(\boldsymbol{X})||\eta\Lambda'; S\Sigma'; J'K'_a; I_N F'_N\rangle\end{aligned} \tag{4.49}$$

The reduced matrix element of the spin is given by

$$\langle I_H||T^1(\boldsymbol{I_H})||I_H\rangle = \sqrt{I_H(I_H+1)(2I_H+1)} \tag{4.50}$$

The other reduced matrix element still contains a dependence on the nuclear spin of the nitrogen atom. This can be removed by another transformation.

$$\begin{aligned}\langle \eta\Lambda; S\Sigma; JK_a; I_N F_N||T^1(\boldsymbol{X})||\eta\Lambda'; S\Sigma'; J'K'_a; I_N F'_N\rangle = \\ (-1)^{J+I_N+F'_N} \begin{Bmatrix} J & F_N & I_N \\ F'_N & J' & 1 \end{Bmatrix} \langle \eta\Lambda; S\Sigma; JK_a||T^1(\boldsymbol{X})||\eta\Lambda'; S\Sigma'; J'K'_a\rangle\end{aligned} \tag{4.51}$$

The complete matrix element is thus

$$\begin{aligned}
&\langle \eta\Lambda; S\Sigma; JK_a; I_N F_N; I_H F_H M_{F_H} | T^1(\boldsymbol{I_H}).T^1(\boldsymbol{X}) | \eta\Lambda; S\Sigma; J'K'_a; I_N F'_N; I_H F'_H M_{F_H} \rangle \\
&\quad = (-1)^{2F'_N+J+F_H+I_N+I_H+1} \begin{Bmatrix} F_N & I_H & F_H \\ I_H & F'_N & 1 \end{Bmatrix} \begin{Bmatrix} J & F_N & I_N \\ F'_N & J' & 1 \end{Bmatrix} \\
&\quad \sqrt{I_H(I_H+1)(2I_H+1)} \sqrt{(2F'_N+1)(2F_N+1)} \\
&\quad \langle \eta\Lambda; S\Sigma; JK_a || T^1(\boldsymbol{X}) || \eta\Lambda'; S\Sigma'; J'K'_a \rangle
\end{aligned} \tag{4.52}$$

The matrix elements for the $\langle \eta\Lambda; S\Sigma; JK_a || T^1(\boldsymbol{X}) || \eta\Lambda'; S\Sigma'; J'K'_a \rangle$ term are of the same form as those for the nitrogen nucleus, if the same breakdown of the hyperfine interaction is used.

4.5.2 Fluorine Coupling

By the same procedure as for the hydrogen nucleus the expression for the interaction with the fluorine nucleus can be derived. There is an extra 6-j symbol reflecting the extra level of coupling that occurs.

$$\begin{aligned}
&\langle \eta\Lambda; S\Sigma; JK_a; I_N F_N; I_H F_H; I_F F M_{F_F} | T^1(\boldsymbol{I_F}).T^1(\boldsymbol{X}) | \eta\Lambda; S\Sigma; J'K'_a; I_N F'_N; I_H F'_H; I_F F M_{F_F} \rangle \\
&\quad = (-1)^{F+2F'_H+F_N+F'_N+J+I_F+I_H+I_N} \begin{Bmatrix} F_H & I_F & F \\ I_F & F'_H & 1 \end{Bmatrix} \begin{Bmatrix} F_N & F_H & I_H \\ F'_H & F'_N & 1 \end{Bmatrix} \begin{Bmatrix} J & F_N & I_N \\ F'_N & J' & 1 \end{Bmatrix} \\
&\quad \sqrt{I_F(I_F+1)(2I_F+1)} \sqrt{(2F'_H+1)(2F_H+1)} \sqrt{(2F'_N+1)(2F_N+1)} \\
&\quad \langle \eta\Lambda; S\Sigma; JK_a || T^1(\boldsymbol{X}) || \eta\Lambda'; S\Sigma'; J'K'_a \rangle
\end{aligned} \tag{4.53}$$

4.6 Magnetic hyperfine parameters for hydrogen and fluorine

The basic expressions for the magnetic hyperfine parameters due to the hydrogen and fluorine nuclei have been derived above before any real consideration has been made of the effects seen at

these nuclei. The conventional theory which has been espoused for the nitrogen nucleus assumes that the interacting nucleus lies on the internuclear axis and has cylindrical symmetry. The other nuclei are remote from the NO axis and will see a net field due to the magnetic moments of the unpaired electron. The conventional Frosch and Foley[2] treatment is not therefore suitable for the remote hydrogen and fluorine nuclei. A pure dipolar treatment of the interaction may be more effective and such a treatment initially has fewer constants than the Frosch and Foley treatment. No Fermi contact term is included as part of this interaction; in the event that the electron transfer to the remote nuclei does take place it can be added using the Frosch and Foley scheme.

The Hamiltonian is represented as for either of the nuclei

$$H_{hf} = -\sqrt{10}\alpha T^1_p(\boldsymbol{I}).\left(T^1_p(\boldsymbol{L},\boldsymbol{C}) + g_e T^1_p(\boldsymbol{S},\boldsymbol{C})\right) \tag{4.54}$$

where α is defined as

$$\alpha = g_I \mu_B \mu_I \frac{1}{r^3} \tag{4.55}$$

and g_e is the g-factor of the electron required for the spin part of the interaction. The Hamiltonian can be substituted into the final unsolved term in either Equation 4.52 or Equation 4.53. The operator has to then be rotated from the space-fixed to the molecule-fixed axis system with the relation $T^1_p(\boldsymbol{Y},\boldsymbol{C^2}) = \sum_q D^{1*}_{pq}(\omega) T^1_q(\boldsymbol{Y},\boldsymbol{C^2})$, where $\boldsymbol{Y}$ denotes $\boldsymbol{S}$ or $\boldsymbol{L}$.

$$\begin{aligned}\langle \eta\Lambda; S\Sigma; JK_a|| -\sqrt{10}\alpha\Big(T^1(\boldsymbol{L},\boldsymbol{C^2}) + g_e T^1(\boldsymbol{S},\boldsymbol{C^2})\Big)||\eta\Lambda'; S\Sigma'; J'K'_a\rangle \\ = \sum_q \langle \eta\Lambda; S\Sigma; JK_a| -\sqrt{10}\alpha D^{1*}_{pq}\Big(T^1_q(\boldsymbol{L},\boldsymbol{C^2}) + g_e T^1_q(\boldsymbol{S},\boldsymbol{C^2})\Big)|\eta\Lambda'; S\Sigma'; J'K'_a\rangle\end{aligned} \tag{4.56}$$

The reduced matrix element can be evaluated by applying the Wigner-Eckart theorem and inte-

grating the matrix elements of the rotation operator.

$$\begin{aligned}
&\langle \eta\Lambda; S\Sigma; JK_a|| - \sqrt{10}\alpha\Big(T^1(\boldsymbol{L}, \boldsymbol{C^2}) + g_e T^1(\boldsymbol{S}, \boldsymbol{C^2})\Big)||\eta\Lambda'; S\Sigma'; J'K_a'\rangle \\
&= \sum_q (-1)^{J-K_a}\sqrt{(2J+1)(2J'+1)}\begin{pmatrix} J & 1 & J' \\ -K_a & q & K_a' \end{pmatrix} \\
&\langle \eta\Lambda; S\Sigma| - \sqrt{10}\alpha\Big(T_q^1(\boldsymbol{L}, \boldsymbol{C}) + g_e T_q^1(\boldsymbol{S}, \boldsymbol{C})\Big)|\eta\Lambda'; S\Sigma'\rangle
\end{aligned} \tag{4.57}$$

Taking the remaining part and making the substitution for $T_q^1(\boldsymbol{Y}, \boldsymbol{C})$ from its definition, initially from Equation 4.22

$$T_q^1(\boldsymbol{Y}, \boldsymbol{C}) = \sqrt{3}(-1)^{q-1}\sum_{q1,q2}\begin{pmatrix} 1 & 2 & 1 \\ q_1 & q_2 & -q \end{pmatrix} T_{q_1}^1(\boldsymbol{Y}).C_{q_2}^2(\theta_i, \phi_i) \tag{4.58}$$

The equation becomes

$$\begin{aligned}
&\langle \eta\Lambda; S\Sigma| - \sqrt{10}A\Big(T_q^1(\boldsymbol{L}, \boldsymbol{C^2}) + g_e T_q^1(\boldsymbol{S}, \boldsymbol{C^2})\Big)|\eta\Lambda'; S\Sigma'\rangle \\
&= \sum_{q_1,q_2}\sqrt{30}A(-1)^q\begin{pmatrix} 1 & 2 & 1 \\ q_1 & q_2 & -q \end{pmatrix}\langle \eta\Lambda; S\Sigma|\Big(T_{q_1}^1(\boldsymbol{L}) + g_e T_{q_1}^1(\boldsymbol{S})\Big)C_{q_2}^2(\theta_i, \phi_i)|\eta\Lambda'; S\Sigma'\rangle
\end{aligned} \tag{4.59}$$

The matrix elements can be divided into the parts of the wavefunction that they act upon. The tensor product $T^1(\boldsymbol{L})C^2(\theta_i, \phi_i)$ however is not Hermitian and has to be expressed as

$$\frac{1}{2}\left\{\langle\eta\Lambda|C_{q_2}^2(\theta_i,\phi_i)|\eta\Lambda''\rangle\langle\eta\Lambda''|T_{q_1}^1(\boldsymbol{L})|\eta\Lambda'\rangle + \langle\eta\Lambda|T_{q_1}^1(\boldsymbol{L})|\eta\Lambda''\rangle\langle\eta\Lambda''|C_{q_2}^2(\theta_i,\phi_i)|\eta\Lambda'\rangle\right\} \tag{4.60}$$

to ensure the Hermiticity of the Hamiltonian. The two tensor operators, $T_{q_1}^1(\boldsymbol{L})$ and $T_{q_1}^1(\boldsymbol{S})$, now need to be rotated into the NO axis system where the components of Λ and Σ are quantized. The $C_{q_2}^2(\theta_i, \phi_i)$ is not rotated because it describes the spatial relationship between the nucleus and the electron. However even in the case where $q_2 = 0$ it can change Λ by ± 2 because the angles θ_i and ϕ_i can be expressed as functions of the azimuthal angle of the electron about the NO axis and as such contain $\cos^2$ terms. Using the substitution

$$T_{q_1}^1(\boldsymbol{L}) = \sum_r d_{q_1 r}^1 T_r^1(\boldsymbol{L}) \tag{4.61}$$

all the parts can then be collated into the final matrix element, which in this case uses Equation 4.52 to generate the result for the hydrogen nucleus.

$$\begin{aligned}
&\langle \eta\Lambda; S\Sigma; JK_a; I_N F_1; I_H F_2| - \sqrt{10}AT^1_p(\boldsymbol{I}).(T^1_p(\boldsymbol{L},\boldsymbol{C}) + g_e T^1_p(\boldsymbol{S},\boldsymbol{C}))|\eta\Lambda'; S\Sigma'; J'K'_a; I'_1F'_1; I_H F'_2\rangle \\
&\quad = \delta_{F_2,F'_2}(-1)^{F_2+2F'_1+J+I_H+I_N+1}\begin{Bmatrix} F_1 & I_H & F_2 \\ I_H & F'_1 & 1 \end{Bmatrix}\begin{Bmatrix} J & F_1 & I_N \\ F'_1 & J' & 1 \end{Bmatrix}[I_H(I_H+1)(2I_H+1)]^{\frac{1}{2}} \\
&\quad [(2F_1+1)(2F'_1+1)]^{\frac{1}{2}}\sum_q (-1)^{J-K_a}[(2J+1)(2J'+1)]^{\frac{1}{2}}\begin{pmatrix} J & 1 & J' \\ -K_a & q & K'_a \end{pmatrix} \\
&\quad \sum_{q_1,q_2}\sqrt{30}A(-1)^q\begin{pmatrix} 1 & 2 & 1 \\ q_1 & q_2 & -q \end{pmatrix}\sum_r d^1_{q_1 r}(\theta) \\
&\quad \Big(\delta_{\Sigma,\Sigma'}\frac{1}{2}\left\{\langle\eta\Lambda|C^2_{q_2}(\theta_i,\phi_i)|\eta\Lambda''\rangle\langle\eta\Lambda''|T^1_r(\boldsymbol{L})|\eta\Lambda'\rangle + \langle\eta\Lambda|T^1_r(\boldsymbol{L}|\eta\Lambda''\rangle\langle\eta\Lambda''|C^2_{q_2}(\theta_i,\phi_i)|\eta\Lambda'\rangle\right\} \\
&\quad + g_e\langle S\Sigma|T^1_r(\boldsymbol{S})|S\Sigma'\rangle\langle\eta\Lambda|C^2_{q_2}(\theta_i,\phi_i)|\eta\Lambda'\rangle\Big)
\end{aligned} \tag{4.62}$$

These then have to be worked up into the full matrix elements by substituting for the rotation matrix $d^1_{q_1 r}(\theta)$ and considering the possible cases for the different summations. There are sums over q, q_1, q_2 and r. The first of these connects states which differ in K_a and can apply in all cases. The q_2 term affects the matrix element of $C^2_{q_2}$ which initially can be set to zero because these states are the most significant. The higher order terms may be required for a complete analysis. The values of q_1 are constrained by the symmetry of the 3-j symbol. Finally r may take the values 0,$\pm$1 which is perfectly fine for the $T^1_r(\boldsymbol{S})$ operator which connects the states of different electron spin projection, Σ. However the $r = \pm 1$ values connect to the Λ-doubling states which will only have a small effect and can be neglected.

The constants obtained are given by

$$\begin{aligned} f &= \delta_{\Lambda,\Lambda'}\langle\eta\Lambda|AC_0^2(\theta_i,\phi_i)|\eta\Lambda'\rangle \\ g &= \delta_{\Lambda,\Lambda'\pm2}\langle\eta\Lambda|AC_0^2(\theta_i,\phi_i)|\eta\Lambda'\rangle \\ h &= \delta_{\Lambda,\Lambda'}\langle\eta\Lambda|AC_1^2(\theta_i,\phi_i)|\eta\Lambda'\rangle \end{aligned} \tag{4.63}$$

The matrix elements are given in complete form in Appendix B.3.

4.7 Nuclear Spin-Spin Interaction

The final interactions which have not yet been accounted for are the nuclear spin-spin interactions taking place between the various magnetic moments of the nuclei in the complex. Of the various possible interactions only the hydrogen-fluorine interaction is derived here as this is expected to be the dominant term. The nuclear magnetic moments of nitrogen, hydrogen and fluorine are $0.404\mu_N$, $2.793\mu_N$ and $2.629\mu_N$[17] respectively. The hydrogen and fluorine are the closest in space and the interaction scales as $\frac{1}{r^3}$ so the hydrogen-fluorine interaction will be the largest. Even the hydrogen and fluorine nuclear spin-spin interaction will only affect the energy at the 10kHz level. The nuclear spin-spin interaction is responsible for the splittings that are observed in NMR spectroscopy.[18] The operator is the same as that for the other spin-spin interactions consisting of the magnetic moments of the nuclear spins and a reduced spherical harmonic representing the spatial relationship between them.

$$H_{SS} = \sqrt{10}T^1(\boldsymbol{I_F}).T^1(\boldsymbol{C^2}, \boldsymbol{I_H}) \tag{4.64}$$

The matrix element is thus

$$\begin{aligned}
&\langle \eta\Lambda; S\Sigma; JK_a; I_N F_N; I_H F_H; I_F F | \sqrt{10} T^1(\boldsymbol{I_F}).T^1(\boldsymbol{C^2}, \boldsymbol{I_H}) | \eta\Lambda'; S\Sigma'; J'K'_a; I_N F'_N; I_H F'_H; I_F F' \rangle \\
&= \delta_{F,F'} (-1)^{F'_H + I_F + F} \begin{Bmatrix} F_H & I_F & F \\ I_F & F'_H & 1 \end{Bmatrix} \sqrt{I_F(I_F+1)(2I_F+1)} \\
&\quad \langle \eta\Lambda; S\Sigma; JK_a; I_N F_N; I_H F_H \| T^1(\boldsymbol{C^2}, \boldsymbol{I_H}) \| \eta\Lambda'; S\Sigma'; J'K'_a; I_N F'_N; I_H F'_H \rangle
\end{aligned} \tag{4.65}$$

which can be reduced by separating the dot product and substituting for the reduced matrix element $\langle I_F \| T^1(\boldsymbol{I_F}) \| I_F \rangle$. The matrix element can then be simplified by separating the matrix element of the operator $T^1_p(\boldsymbol{C}, \boldsymbol{I_H})$

$$\begin{aligned}
&\langle \eta\Lambda; S\Sigma; JK_a; I_N F_N; I_H F_H \| T^1(\boldsymbol{C^2}, \boldsymbol{I_H}) \| \eta\Lambda'; S\Sigma'; J'K'_a; I_N F'_N; I_H F'_H \rangle \\
&= \sqrt{3(2F_H+1)(2F'_H+1)} \begin{Bmatrix} F_N & F'_N & 2 \\ I_H & I_H & 1 \\ F_H & F'_H & 1 \end{Bmatrix} \sqrt{I_H(I_H+1)(2I_H+1)} \\
&\quad \langle \eta\Lambda; S\Sigma; JK_a; I_N F_N \| C^2(\theta_i, \phi_i) \| \eta\Lambda'; S\Sigma'; J'K'_a; I_N F'_N \rangle
\end{aligned} \tag{4.66}$$

and substituting for the reduced matrix element $\langle I_H \| T^1(\boldsymbol{I_H}) \| I_H \rangle$. The reduced spherical harmonic acts on the total angular momentum, J, so the reduced matrix element can be rewritten as

$$\begin{aligned}
&\langle \eta\Lambda; S\Sigma; JK_a; I_N F_N \| C^2_p(\theta_i, \phi_i) \| \eta\Lambda'; S\Sigma'; J'K'_a; I_N F'_N \rangle \\
&= (-1)^{J + I_N + F'_N + 2} \sqrt{(2F_N+1)(2F'_N+1)} \begin{Bmatrix} F_N & J & I_N \\ J' & F'_N & 2 \end{Bmatrix} \\
&\quad \langle \eta\Lambda; S\Sigma; JK_a \| C^2(\theta_i, \phi_i) \| \eta\Lambda'; S\Sigma'; J'K'_a \rangle
\end{aligned} \tag{4.67}$$

The reduced matrix element of $C^2_p(\theta_i, \phi_i)$ can be evaluated by rotating the operator into the molecule fixed axis system and comparing it with the reduced matrix element of the operator

from the Wigner-Eckart theorem to give

$$\begin{aligned}&\langle \eta\Lambda; S\Sigma; JK_a \| C^2(\theta_i,\phi_i) \| \eta\Lambda'; S\Sigma'; J'K'_a\rangle \\ &\quad = \sum_q (-1)^{J-K_a} \sqrt{(2J+1)(2J'+1)} \begin{pmatrix} J & 2 & J' \\ -K_a & q & K'_a \end{pmatrix} \langle \eta\Lambda; S\Sigma | C^2_q(\theta_i,\phi_i) | \eta\Lambda'; S\Sigma'\rangle\end{aligned} \tag{4.68}$$

The reduced spherical tensor operator only describes the spatial relationship of the hydrogen and fluorine nuclei and does not act on the angular momenta associated with the NO so it is acceptable to stop and this point and say that the matrix element $\langle \eta\Lambda; S\Sigma | C^2_q(\theta_i,\phi_i) | \eta\Lambda'; S\Sigma'\rangle$ is a constant.

The complete matrix element is

$$\begin{aligned}&\langle \eta\Lambda; S\Sigma; JK_a; I_N F_N; I_H F_H; I_F F | \sqrt{10} T^1(\boldsymbol{I_F}).T^1(\boldsymbol{C}, \boldsymbol{I_H}) | \eta\Lambda'; S\Sigma'; J'K'_a; I_N F'_N; I_H F'_H; I_F F'\rangle \\ &= \delta_{F,F'} (-1)^{J+F'_N+F'_H+F+I_N+I_F+2} \sqrt{I_F(I_F+1)(2I_F+1)} \sqrt{I_H(I_H+1)(2I_H+1)} \\ &\quad \sqrt{30(2F_H+1)(2F'_H+1)} \sqrt{(2F_N+1)(2F'_N+1)} \sqrt{(2J+1)(2J'+1)} \\ &\quad \begin{Bmatrix} F_H & I_F & F \\ I_F & F'_H & 1 \end{Bmatrix} \begin{Bmatrix} F_N & F'_N & 2 \\ I_H & I_H & 1 \\ F_H & F'_H & 1 \end{Bmatrix} \begin{Bmatrix} F_N & J & I_N \\ J' & F'_N & 2 \end{Bmatrix} \sum_q (-1)^{J-K_a} \\ &\quad \begin{pmatrix} J & 2 & J' \\ -K_a & q & K'_a \end{pmatrix} \langle \eta\Lambda; S\Sigma | C^2_q(\theta_i,\phi_i) | \eta\Lambda'; S\Sigma'\rangle\end{aligned} \tag{4.69}$$

References

[1] R. Beringer, J. G. Castle. *Phys. Rev.*, **78**, 581, (1950).

[2] R. A. Frosch, H. M. Foley. *Phys. Rev*, **88**, 1337, (1952).

[3] R. M. Neumann. *Astro. J.*, **161**, 779, (1970).

[4] G. C. Dousmanis. *Phys. Rev.*, **97**, 967, (1955).

[5] M. Mizushima. *Phys. Rev*, **94**, 569, (1954).

[6] M. Mizushima, K. M. Evenson, J. S. Wells. *Phys. Rev. A*, **5**, 2276, (1972).

[7] C. C. Lin, M. Mizushima. *Phys. Rev.*, **100**, 1726, (1955).

[8] R. L. Brown, H. E. Radford. *Phys. Rev.*, **147**, 147, (1966).

[9] J. M. Brown, M. Kaise, C. M. L. Kerr, D. J. Milton. *Mol. Phys.*, **36**, 553, (1978).

[10] G. C. Dousmanis, T. M. Sanders Jr, C. H. Townes. *Phys. Rev.*, **100**, 1735, (1955).

[11] R. L. Cook, F. C. De Lucia. *Am. J. Phys.*, **39**, 1433, (1971).

[12] R. N. Zare. *Angular Momentum: Understanding Spatial Aspects of Physics and Chemistry*. Wiley, New York, (1988).

[13] M. E. Rose. *Elementary Theory of Angular Momentum*. Wiley, New York, (1957).

[14] A. R. Edmonds. *Angular Momentum in Quantum Mechanics*. Princeton University Press, Princeton, NJ, (1974).

[15] D. M. Brink, G. R. Satchler. *Angular Momentum*. Clarendon Press, Oxford, (1979).

[16] C. H. Townes, A. L. Schawlow. *Microwave Spectroscopy*. McGraw-Hill, New York, (1955).

[17] I. Mills, T. Cvitaš, K. Homann, N. Kallay, K. Kuchitsu. *Quantities, Units and Symbols in Physical Chemistry*. Blackwell Scientific Publications, Oxford, (1993).

[18] R. R. Ernst, G. Bodenhausen, A. Wokaun. *Principles of Nuclear Magnetic Resonance in One and Two Dimensions*. Oxford University Press, Oxford, (1997).

Chapter 5

Results

What we call the beginning is often the end
And to make an end is to make a beginning
The end is where we start from

We shall not cease from exploration
And the end of all our exploring
Will be to arrive where we started
And know the place for the first time
-T. S. Eliot, Little Gidding

5.1 Introduction

The discussion of the spectroscopy of NO-HF is introduced by a brief review of previous studies of complexes containing NO.

The first spectroscopic observations of NO complexes occurred at the end of the 1970's with MBER spectroscopy of $(NO)_2$.[1,2] NO dimer is different in its bonding to other van der Waals complexes because it contains a more chemical component with electron spin-pairing producing a large exchange energy. The complex is therefore stabilised with respect to a pure electrostatic interaction and can be regarded as chemically bonded species. The complex of a closed-shell molecule with an open-shell partner can only have small exchange effects and the bonding should more closely resemble that of two closed-shell molecules.

At about the same time rotational spectra of Ar-NO were seen, again using MBERS. The spectra were extremely complex and posed considerable difficulty in analysis, with no comparable studies having been done before on any similar complexes. A formalism was developed to explain the fine and hyperfine structure of the spectra.[3] The spectral assignment was problematic and was deduced by the use of common differences and double resonance. The analysis is still far from complete. In the analysis the complex was found to deviate from T-shaped by 5.175° with a small positive Renner-Teller parameter, ϵ_2, indicating that the unpaired electron slightly favours the out of plane orbital. Since then other complexes with similar properties have been studied, e.g. Ar-OH.[4]

NO-HF was first observed by Davis, Andrews and Trindle[5] in the infrared using matrix isolation. The complex was then observed by Fawzy et al.[6] in the gas phase using infrared spectroscopy, where a bent structure with an angle of approximately 30° was proposed with a large value for the Renner-Teller parameter, ϵ. The infrared data provided the requisite rotational constants to predict the frequencies of the spectrum in the microwave, thus facilitating the search for the microwave spectrum of the complex. In the absence of the infrared data the location of the spectrum would have been very difficult to predict. The analysis of the infrared spectrum has an anomaly in that the constants for the excited vibrational state are very different from those of the ground state. Normally the two sets of constants only deviate from one another by a few percent because of the change in average bond length between the vibrational states. The large change may be attributable to the close correspondence in energy between two quanta of the NO stretch and one quantum of the HF stretch. An intermolecular Fermi resonance could thus be taking place. Evidence of this can be found in the exceptionally effective collisional deactivation of HF($\nu = 1$) by NO.[7]

NO-HF is one of a few complexes studied to date which exhibit an intermolecular hyperfine interaction. It is the analysis of this hyperfine interaction that provides the data of most value because it is a direct probe of the changes that are taking place in the electronic structure of the

monomers due to complexation.

5.2 Experimental

The microwave spectrometer which was described in detail in Chapter 2 was used to collect the data discussed here. A gas mixture containing approximately 1% of both NO and HF in an argon carrier was used at a backing pressure of 1atm. The mixture was expanded into the Fabry-Perot cavity through a pulsed nozzle with an orifice of 0.5mm at a repetition rate of between 10 and 20Hz with a pulse length of 600μS. Data were collected with current running through a set of mutually perpendicular Helmholtz coils to remove the Earth's magnetic field. Spectra were collected in many cases with the Helmholtz coils off as well in order to resolve the Zeeman components of the transition. For any given spectrum between 10-10000 gas pulses were required depending on the relative intensity of the transition. Double resonance measurements were made for many transitions to aid the assignments.

5.3 Results

The fine structure energy level pattern of NO-HF is quite complex being formed from an asymmetric rotor with the orbital and spin components of the unpaired electron and the Renner-Teller interaction. Figure 5.1 shows the pattern derived from the theory in Chapter 3 using the constants that result from the fitting detailed later in this chapter at an angle of 49°. There are eight levels of $|K_a| = \frac{1}{2}$ for each rotational quantum number which derive from the two values of K_a with the four possible combinations of the projections of the orbital and spin angular momenta of the unpaired electron Λ and Σ that occur. If the diagonal terms of the fine structure matrix in Table 3.2 are considered, then the large separation between the two groups of four levels would be the spin-orbit interaction and then the intermediate separation would be $A\cos\theta$. In the complex itself there is extensive mixing of the levels by the Renner-Teller term which complicates

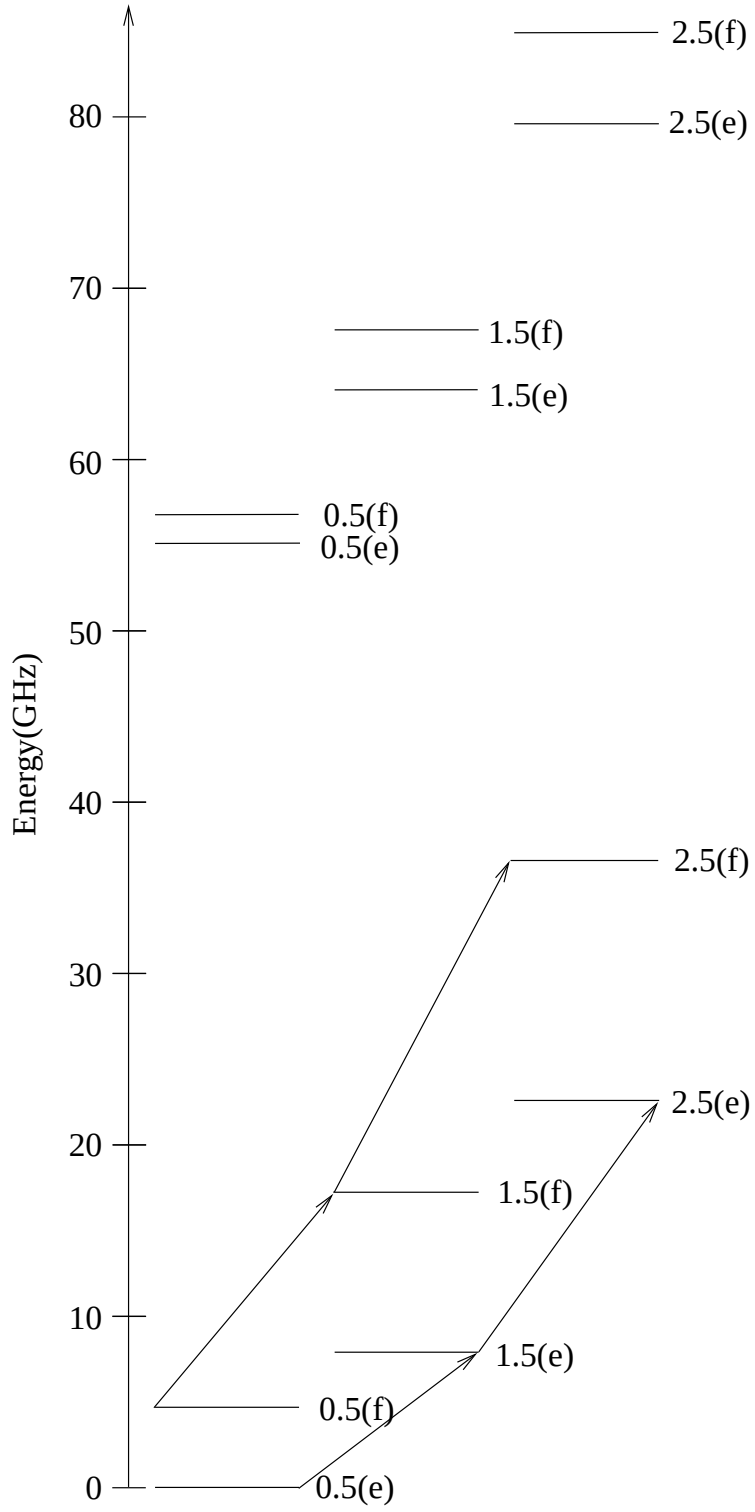

Figure 5.1: Calculated fine structure energy levels of the van der Waals complex NO-HF, with the four observed transition groups marked. The levels are labelled with their rotational level, J, and their parity.

the attribution of the splittings.

Fawzy et al[6] only observed the lower groups of rotational levels including the parity splitting, presumably because the higher levels were not sufficiently populated. As a consequence of this only these levels were searched for in the microwave region. A total of four rotational transitions were observed within a few megahertz of the initial predictions based on the constants from the infrared data. These are marked on the Figure 5.1. It is possible that transitions within the upper groups of rotational levels could be observed and some attempts were made to find them. However they were not seen which may be due to the cooling effect of the supersonic expansion depopulating the levels.

Each of the fine structure levels was found to have a rich hyperfine structure due to the presence of three nuclei possessing a spin magnetic moment, making the assignment a much more arduous task. This was an unexpected complication because the effect of an unpaired electron on one monomer of the complex on the nucleus in another monomer had not been seen before. Quadrupolar effects on the rare gas atom have been seen in some of the rare gas hydrogen halide complexes[8, 9] but this is not the same because it depends on the electric not the magnetic field. In excess of 1100 spectra were eventually collected of the 156 observed spectral transitions. Each transition required several spectra either to resolve overlapping lines, determine absolute positions or measure Zeeman patterns.

A further complication was the observation of significant Zeeman splittings of most of the hyperfine transitions. This is interesting because the NO molecule itself has no net magnetic moment, in the $^2\Pi_{\frac{1}{2}}$ ground state. The lack of a magnetic moment in NO is caused by the opposition of the magnetic moments due to the orbital motion of the electron and the spin of the electron which cancel almost entirely due to the g-value of the spin. Indeed in the microwave spectrum of Ar-NO[3] no effects of the magnetic moment were observed. However in NO-HF there is a magnetic moment because of the quenching of the orbital motion of the unpaired electron on the NO by the presence of the HF molecule. This reduces the magnetic moment of

the orbital motion allowing a resultant magnetic moment, from the electron spin on the complex which can couple to the Earth's magnetic field to remove the degeneracy of the M_F components of the total angular momentum. This is confirmed later by the magnitudes of the eigenvectors from the diagonalization of the fine structure illustrated in Table 5.4. The table shows that the $\Omega = \frac{3}{2}$ states constitute a significant proportion of the wavefunction of the fine structure states of the NO-HF complex.

The number of hyperfine components for each fine structure state can be obtained by coupling sequentially each nuclear spin angular momentum.

$$\begin{aligned} \boldsymbol{J} + \boldsymbol{I_N} &\rightarrow \boldsymbol{F_N} \\ \boldsymbol{F_N} + \boldsymbol{I_H} &\rightarrow \boldsymbol{F_H} \\ \boldsymbol{F_H} + \boldsymbol{I_F} &\rightarrow \boldsymbol{F} \end{aligned} \tag{5.1}$$

I_N=1 and $I_H = I_F = \frac{1}{2}$ so twelve hyperfine levels would be expected for each rotational level, except for $J = \frac{3}{2}$ and $J = \frac{1}{2}$ where eleven and seven levels are expected respectively. If the relative interactions are different then the intermediate quantum numbers, F_N and F_H are still valid and can be used to label the states.

The spectra were assigned starting with the J=$\frac{3}{2}$(f)-$\frac{1}{2}$(f) centred at 12.28GHz because these were the first levels found and the simplest to comprehend. The J=$\frac{5}{2}$(e)-$\frac{3}{2}$(e), at 14.41GHz, and J=$\frac{3}{2}$(e)-$\frac{1}{2}$(e), at 7.72GHz, were thoroughly measured, but the assignment here proved to much more difficult. Lastly there is the J=$\frac{5}{2}$(f)-$\frac{3}{2}$(f) transition at 18.93GHz. The assignments will now be discussed.

5.3.1 12GHz; J=$\frac{3}{2}$(f)-$\frac{1}{2}$(f) Transitions

Fortuitously this was the first group of lines that was exhaustively measured. Forty-nine hyperfine transitions were observed spread over a region of 70MHz centred at 12 275.0MHz. Initially only three relatively closely spaced groups were seen starting at 12 279MHz and extending up

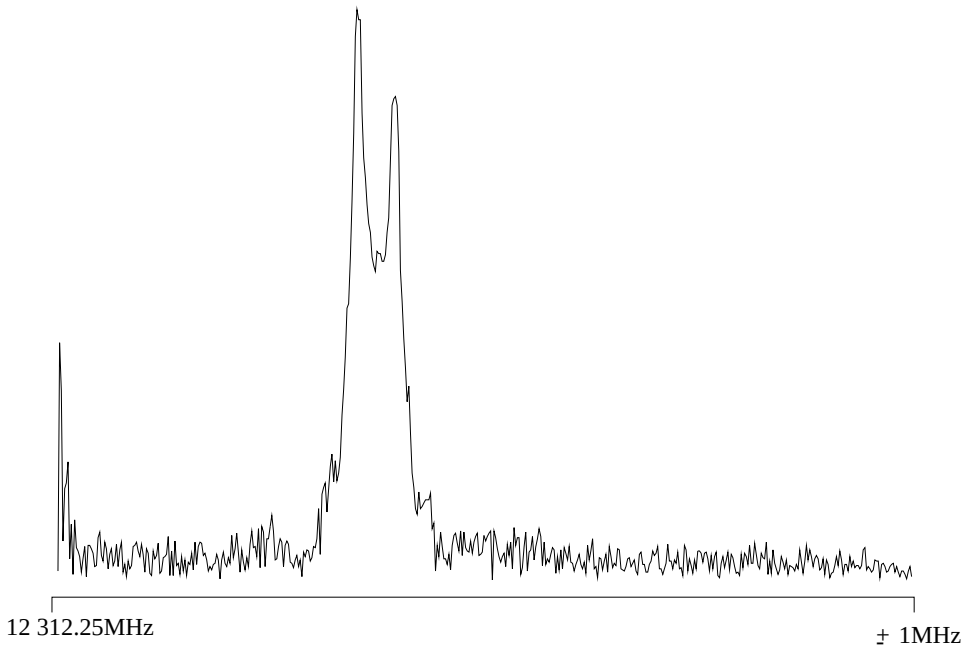

Figure 5.2: Spectrum of the J=$\frac{3}{2}$,f,$\frac{3}{2}$, 2, $\frac{5}{2}$-$\frac{1}{2}$,f,$\frac{1}{2}$, 1, $\frac{3}{2}$ transition in NO-HF in a null magnetic field

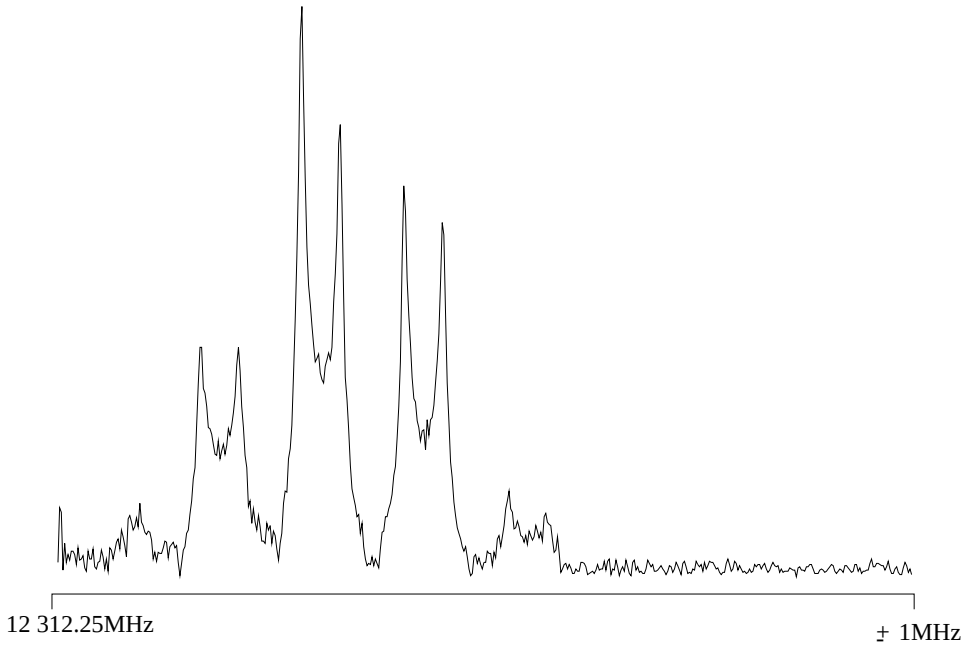

Figure 5.3: Spectrum of the J=$\frac{3}{2}$,f,$\frac{3}{2}$, 2, $\frac{5}{2}$-$\frac{1}{2}$,f,$\frac{1}{2}$, 1, $\frac{3}{2}$ transition in NO-HF in the Earth's magnetic field

to 12 312MHz. These groups were attributed to the nitrogen hyperfine which one would naïvely anticipate to have the largest hyperfine splitting being the closest in space to the unpaired electron. Two of the groups were attributed to the $\Delta F_N = +1$ which are expected to contain the strongest transitions. The remaining group was a $\Delta F_N = 0$. There were therefore two more groups which had not yet been seen, the other $\Delta F_N = 0$ and the $\Delta F_N = -1$. On searching for them they were found at around 12 260MHz and 12 245MHz. The finding and the attribution of the groups to the nitrogen hyperfine had effectively assigned one out of the three total angular momentum quantum numbers required to label the energy levels.

The next piece of data that could be easily extracted was the total F quantum number because of the structure of the Zeeman patterns observed in the Earth's magnetic field, see Figures 5.2 and 5.3. A magnetic field removes the degeneracy of the M_F components of the total angular momentum. The antenna is normally oriented parallel to the Earth's magnetic field so that the selection rule is $\Delta M_F = 0$. A pattern of ($2F_{min}$+1) components is then seen for a given transition, where F_{min} is the smallest of the two total angular momenta involved in the transition. There is additional information in the intensity variation of the components of the Zeeman pattern. The intensity is given by a 3-j symbol $\begin{pmatrix} F & 1 & F' \\ -M_F & 0 & M'_F \end{pmatrix}$ which when $\Delta F = 0$ gives an intensity proportional to M_F^2. If $\Delta F = \pm 1$ then the intensities of the M_F components are proportional to $(F+1)^2 - M_F^2$. The simple result is that if $\Delta F = 0$ then the Zeeman transitions have a bowl shaped profile with the lowest intensity components in the centre and if $\Delta F = \pm 1$ then the Zeeman pattern has a humped profile, as is seen in Figure 5.3. Each transition may, for a $\Delta F = 0$, have its F quantum number explicitly assigned or for a $\Delta F = \pm 1$ have two possible F quantum numbers assigned to it depending on whether the smaller F quantum number is in the upper or lower state.

However there are two different types of doublet which arise from $F = \frac{1}{2} - \frac{1}{2}$ and $F = \frac{3}{2} - \frac{1}{2}$ transitions that cannot be distinguished. If the antenna is rotated 90°, so that it is perpendicular to

the Earth's magnetic field, then the selection rules for the transitions change to $\Delta M_F = \pm 1$. The $F = \frac{3}{2} - \frac{1}{2}$ transition then has four allowed components because transitions there are transitions from the $M_F = \frac{1}{2}$ to the $M_F = -\frac{1}{2}, \frac{3}{2}$ and from the $M_F = -\frac{1}{2}$ to the $M_F = \frac{1}{2}, -\frac{3}{2}$ levels but the $F = \frac{1}{2} - \frac{1}{2}$ still has only two components due to $M_F = \frac{1}{2}$ to $M_F = -\frac{1}{2}$ and $M_F = -\frac{1}{2}$ to $M_F = \frac{1}{2}$. The effect of the rotation of the antenna on a $F = \frac{3}{2} = \frac{1}{2}$ transition is illustrated in Figures 5.4 and 5.5.

Each of the observed spectral transitions then had a limited amount of data associated with it, the quantum number of the nitrogen hyperfine, F_N and a set of alternatives for the total angular quantum number F. The only way to go from this to a complete assignment was to build up assignments of lines and test them against one another until a complete self-consistent assignment was achieved. Common differences were used to provide an indication of shared levels and helped in extending the assignment to all the observed transitions. This was facilitated by the fact that the hyperfine energy levels exhibited a simple structure with a large nitrogen hyperfine splitting, a smaller splitting attributed to the hydrogen nucleus and the smallest splitting which was assigned to the effect of the fluorine nucleus. The effect of the nitrogen nucleus could be easily separated from that of the hydrogen and fluorine nuclei because it has a different nuclear spin and splits the spectrum into a different number of components. The hydrogen and fluorine nuclei have the same spin and thus the same effect when coupled to the total angular momentum and cannot be separated in that way. The couplings were ordered with the hydrogen larger than the fluorine because the magnitude of the hyperfine interaction was expected to scale as $\left\langle \frac{1}{r^3} \right\rangle$ where r is the distance of the nucleus from the unpaired electron. However it was not until the global fit took place that the effects could be definitively assigned to a particular nucleus.

Many permutations were manually tested until one was found that could explain all of the observed levels. The assignment was then confirmed by the capability of the assignment to accurately predict the locations of other transitions which had not been seen.

There is additional information that can be used as an aid to assignment of the spectra.

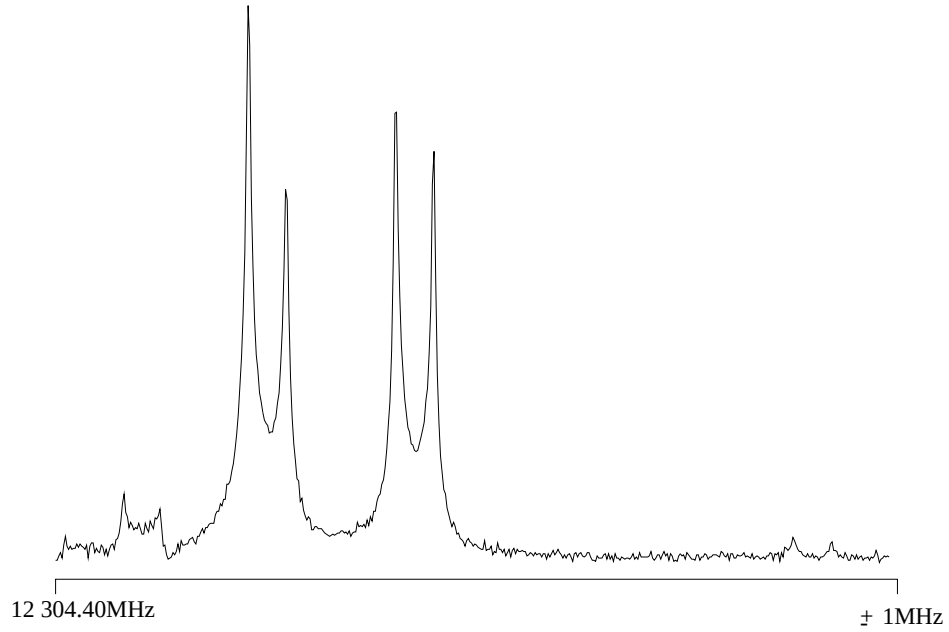

Figure 5.4: Spectrum of the J=$\frac{3}{2}$,f,$\frac{3}{2}$, 1, $\frac{3}{2}$-$\frac{1}{2}$,f,$\frac{1}{2}$, 1, $\frac{1}{2}$ transition in NO-HF in the Earth's magnetic field with the antenna parallel to the magnetic field

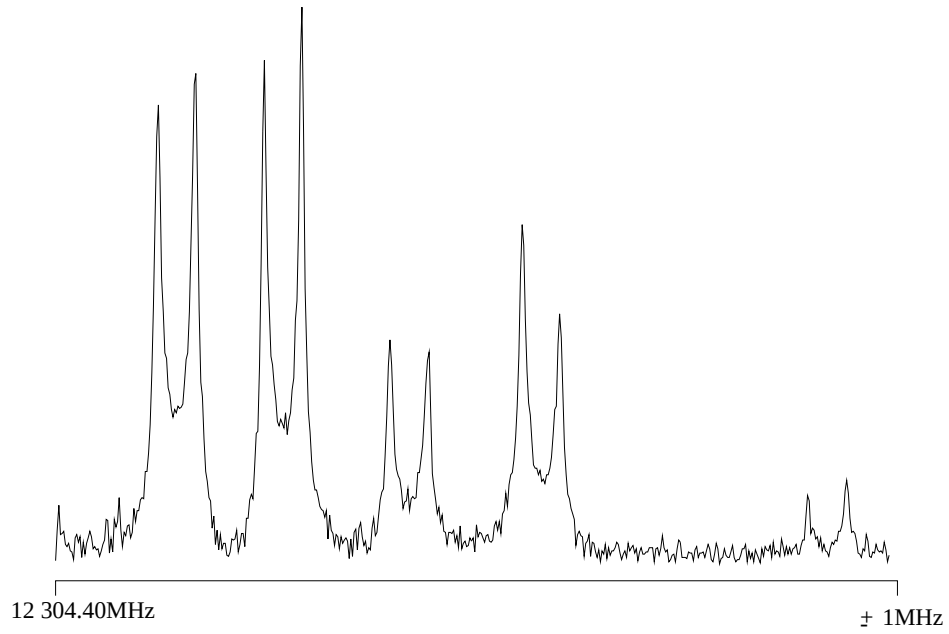

Figure 5.5: Spectrum of the J=$\frac{3}{2}$,f,$\frac{3}{2}$, 1, $\frac{3}{2}$-$\frac{1}{2}$,f,$\frac{1}{2}$, 1, $\frac{1}{2}$ transition in NO-HF in the Earth's magnetic field with the antenna perpendicular to the magnetic field

If there is only limited mixing of the states that constitute the hyperfine energy levels then the relative intensities of the transitions can be evaluated and help to indicate whether the assignment of a line is correct. Although it is not possible to measure absolute intensities with the microwave spectrometer, because of the many variables which control its operation, the relative intensities over a small frequency region are viable.

The intensity of a transition is the square of the matrix element of the dipole moment operator. Now it is simple to remove the F dependence of the operator to leave the intensity as

$$\begin{aligned} I \propto \Bigg| & \sqrt{(2F+1)(2F'+1)(2F_H+1)(2F'_H+1)(2F_N+1)(2F'_N+1))} \\ & \times \begin{Bmatrix} F_H & F & I_F \\ F' & F'_H & 1 \end{Bmatrix} \begin{Bmatrix} F_N & F_H & I_H \\ F'_H & F'_N & 1 \end{Bmatrix} \begin{Bmatrix} J & F_N & I_N \\ F'_N & J' & 1 \end{Bmatrix} \\ & \times \langle \nu\Lambda; S\Sigma; JK_a \| T^1(\mu) \| \nu\Lambda'; S\Sigma'; J'K'_a \rangle \Bigg|^2 \end{aligned} \tag{5.2}$$

for the vector model with no mixing of intermediate quantum numbers. The first part just depends on the total angular momentum quantum numbers of the complex and will contain the probability of the transitions between the various F states. The other part, the matrix element $\langle \nu\Lambda; S\Sigma; JK_a \| T^1(\mu) \| \nu\Lambda'; S\Sigma'; J'K'_a \rangle$, contains probability of the particular fine structure transition. Now as only levels of the same fine structure transition are being compared this term will be a constant and will not be required in the relative intensity. The product of the 6-j symbols and the various F based terms can be evaluated to give a table of relative transition probabilities for the various hyperfine levels combinations. The results indicate, unsurprisingly that the strongest transitions are those for which all the hyperfine quantum numbers increase by one. The second strongest group are those for which the quantum numbers do not change. The intensity data can then be used as an additional guide for the assignment.

Finally the separations in the Zeeman splittings could be determined which could then be used to indicate if two transitions have an energy level in common. A simple vector model for the coupling of the magnetic moments was assumed similar to that used for calculating the

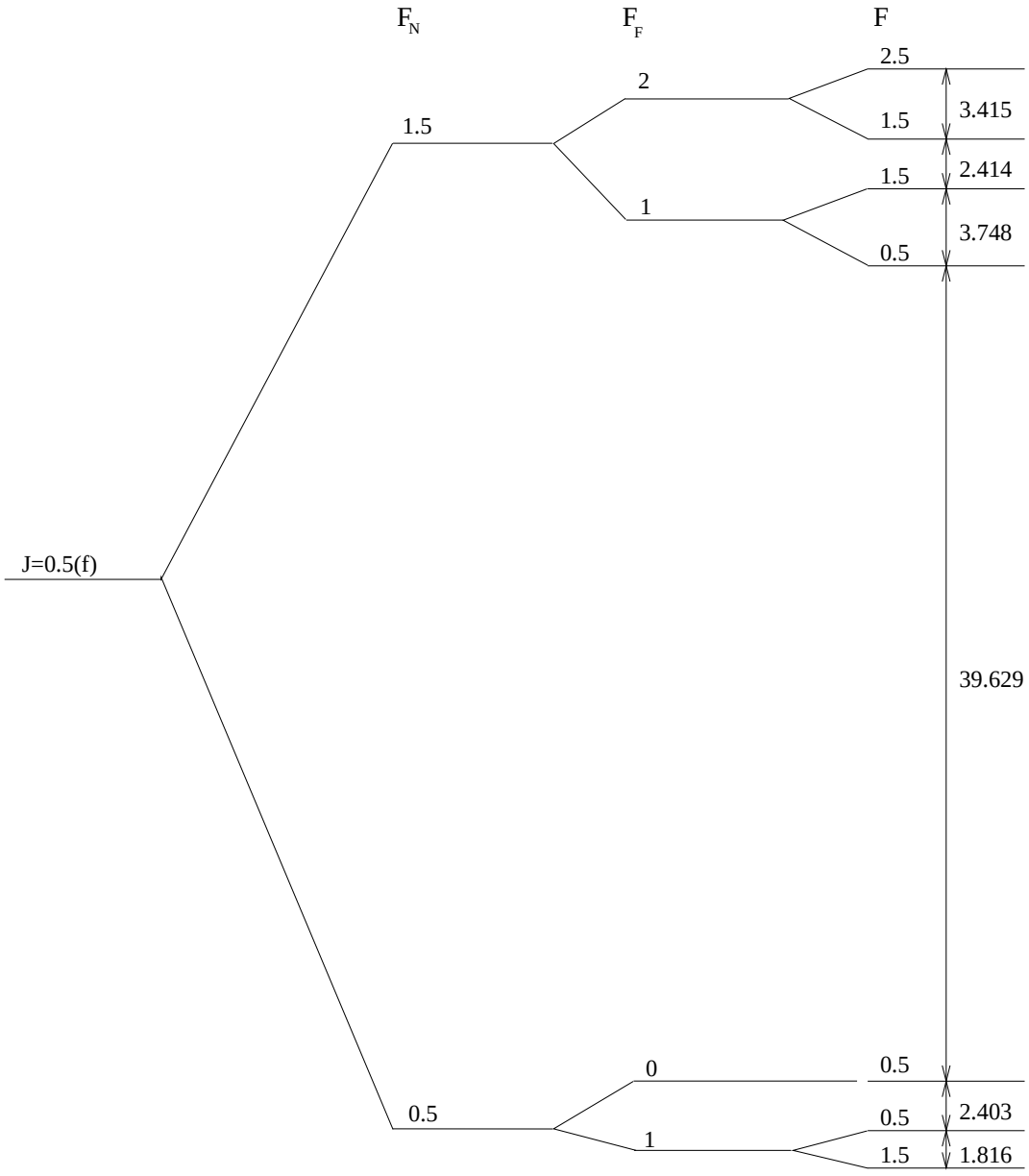

Figure 5.6: Energy Level Diagram of the J=$\frac{1}{2}$(f) State of NO-HF. The splittings are in MHz.

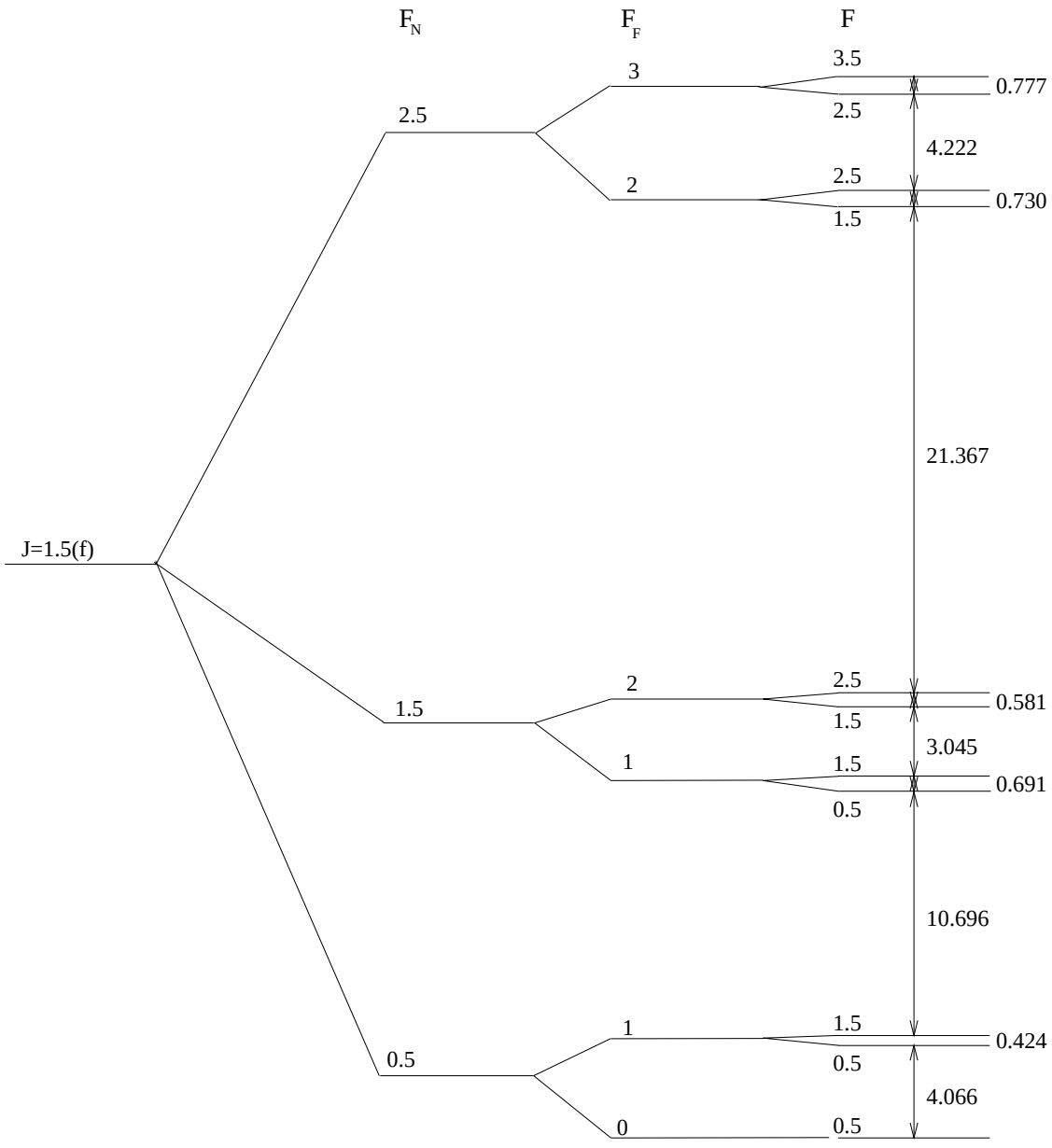

Figure 5.7: Energy Level Diagram of the J=$\frac{3}{2}$(f) State of NO-HF. The splittings are in MHz.

Zeeman effect in atoms.[10] This results in a Hamiltonian for the Zeeman effect of

$$H_{Zee} = -\gamma_e g \left\{ \frac{F_N(F_N+1) + J(J+1) - I_N(I_N+1)}{2(F_N(F_N+1)} \right\} \left\{ \frac{F_H(F_H+1) + F_N(F_N+1) - I_H(I_H+1)}{2(F_H(F_H+1)} \right\} \left\{ \frac{F(F+1) + F_H(F_H+1) - I_F(I_F+1)}{2(F(F+1)} \right\} \boldsymbol{F.B} \tag{5.3}$$

When this matrix element is evaluated it will be possible to determine for a given F the Zeeman splitting of the lines. This formula was applied when two lines had been assigned to have a common level. The differences in the Zeeman pattern, if the different levels were of a common total angular momentum, F, could be used to calculate a constant for a given F. Once carried out for a number total angular momentum states Zeeman patterns can be predicted and compared confirming the assignment. The method does rely on the fact that there is not significant perturbation of the Zeeman patterns by other levels.

The resulting hyperfine patterns for the $J = \frac{1}{2}$(f) and $J = \frac{3}{2}$(f) are shown in Figures 5.6 and 5.7 respectively. The relative magnitudes of the splittings confirm the vector model used.

5.3.2 7GHz; J=$\frac{3}{2}$(e)-$\frac{1}{2}$(e) and 14GHz; J=$\frac{5}{2}$(e)-$\frac{3}{2}$(e) Transitions

The techniques developed for the 12GHz transition group were applied to the e-states with no success because the spectra are much more compressed occurring in a band of width 32MHz for the J=$\frac{3}{2}$(e)-$\frac{1}{2}$(e) transition and 20MHz for the J=$\frac{5}{2}$(e)-$\frac{3}{2}$(e) transition. The problem is that there is no easy way to determine the nitrogen quantum number because the transitions do not divide up into well spaced groups as for the f-states. The Zeeman patterns for many of the transitions cannot be determined because of the small separations between the lines so that when the Earth's magnetic field is allowed to act the components of the Zeeman patterns overlap preventing resolution of the pattern. There is clearly a paucity of information required to assign the spectra.

The lack of information would seem to render the assignment of the e-states an impossibility

2.5	1.5	1.5	0.5	3.5	0.5	2.5	2.5	1.5	1.5	0.5	F
							14 423.427	14 422.074	14 419.679	14 417.594	1.5
				14 424.669			14 420.412	14 419.057	14 416.667		2.5
						14 420.011	14 418.145	14 416.778	14 414.388		2.5
		14 424.253			14 420.222				14 414.248	14 412.168	0.5
				14 419.886			14 415.638				3.5
14 426.355	14 424.147	14 421.414	12 420.936		14 417.388				14 411.408	14 409.326	1.5
						14 415.805	14 413.935				3.5
		14 418.806	14 418.312					14 411.177			1.5
				14 415.114							4.5
14 421.548		14 416.609					14 410.354		14 406.600		2.5
	14 417.272					14 410.152					2.5
14 416.455				14 409.510			14 405.265				3.5
7 716.527	7 718.729					7 725.851	7 727.721	7 729.086	7 731.464	7 733.553	1.5
7 718.265		7 723.204		7 725.210		7 727.582	7 729.455		7 733.210		2.5
	7 720.607	7 723.344			7 727.368			7 730.958	7 733.355	7 735.425	0.5
7 720.1450	7 722.349				7 729.105	7 729.471	7 731.339		7 735.092	7 737.171	1.5
	7 723.481	7 726.216						7 733.831	7 736.224	7 738.301	0.5
		7 738.041			7 742.068				7 748.049	7 750.013	1.5
			7 738.783								0.5

Table 5.1: Diagram illustrating the energy levels with the observed transitions of the J=$\frac{3}{2}$(e)-$\frac{1}{2}$(e) and J=$\frac{5}{2}$(e)-$\frac{3}{2}$(e), showing the connections between the states. The J=$\frac{1}{2}$(e) and the J=$\frac{5}{2}$(e) levels are spaced vertically as the 7GHz and 14GHz groups respectively. The J=$\frac{3}{2}$(e) levels are spaced horizontally. The quantum number in the margin is the total angular momentum, F

unless some additional data can be provided. Double resonance experiments generate the required information because it allows the determination of common energy levels between pairs of transitions. It is convenient that these two rotational transitions among the e-states share a common energy level, the J=$\frac{3}{2}$(e).

The double resonance experiments were carried out with a coaxial to waveguide converter mounted perpendicular to the axis of the Fabry-Perot cavity to act as a horn antenna. A transition would then be selected and the spectrometer would be optimized to detect that signal. Spectra of a transition at one frequency would be taken while continuous microwave radiation corresponding to an observed transition, in the other group of transitions, was being applied via the double resonance antenna. If the signal being monitored by the spectrometer were in the 14GHz group then the applied continuous radiation would correspond to a transition in the 7GHz group and vice versa. Each of the known frequencies in the complementary group would be tried and if the observed signal was significantly diminished by the applied microwave radiation the two transitions thus share a common hyperfine level in the J=$\frac{3}{2}$(e) state. It is not possible to carry out double resonance within one group which would establish common levels within that group because the proximity of the double resonance radiation to the detected radiation. Indeed the presence of too much power even at a frequency 7GHz away could cause the low noise preamplifier to saturate giving spurious double resonance signals. Luckily such an eventuality could be detected by verifying the signal on the monitor oscilloscope.

By testing each transition in turn, diagrams of common levels could be constructed. The diagram for the e-states is shown in Table 5.1. The frequencies in the diagram all correspond to transitions that have been observed. The gaps are transitions that have not been seen, either because they are forbidden by the selection rules, are of too low intensity to observe or are obscured by stronger transitions. When collecting data the gaps in the diagram can be filled in because they represent transitions that have not been observed or they may have been seen but not tested for double resonance. In addition the predicted frequencies could be searched for. The

diagrams are a simple way to represent a considerable amount of interrelated data in a compact form.

Each diagram contains three sets of data, the hyperfine energy levels of the J=$\frac{1}{2}$, $\frac{3}{2}$ and $\frac{5}{2}$ fine structure states. The relative energy levels of the J=$\frac{1}{2}$ state are spaced vertically, when the page is viewed landscape, as the lower block of frequencies. Each frequency in the same row originates from the same energy level in the J=$\frac{1}{2}$ state. The energy levels of the J=$\frac{5}{2}$ state are also spaced vertically up the diagram as the upper block of frequencies with a row here constituting a common upper state for a transition.

The J=$\frac{3}{2}$ levels are represented by the columns. The lowest level being on the left and the highest on the right. In one column the frequencies for the J=$\frac{1}{2}$ state increase down the column because the lower energy levels move further away from the J=$\frac{3}{2}$ level represented by the column. The J=$\frac{5}{2}$ frequencies in a column decrease down the column because the lower energy levels are closer in energy to the level that the column represents. In the rows, for a J=$\frac{1}{2}$ level the frequencies increase left to right because the higher a J=$\frac{3}{2}$ is in energy the further away from the J=$\frac{1}{2}$ level. A row decreases for J=$\frac{5}{2}$ from left to right because the J=$\frac{3}{2}$ levels increase in energy and move closer to the J=$\frac{5}{2}$ level.

The double resonance provided the energy level spacings for the e-states but it still did not contain sufficient information for a complete assignment to take place. Most of the levels could have a total angular momentum quantum number, F, assigned using the Zeeman patterns, but it did not help with assigning the intermediate quantum numbers. It became clear that there was extensive mixing of the states so that the hyperfine levels were no longer of dominantly one state. The only levels which could be definitively be assigned were those of maximum quantum number, $F = J + I_N + I_H + I_F = J + 2$. The maximum F levels are unique and are not perturbed by other levels. In this situation things like the relative intensity information becomes less effective because of intensity borrowing from other levels. The Zeeman patterns become highly perturbed so their spacings may not be used. Essentially the coupling scheme that was

used for the f-states is no longer appropriate and another method was needed.

Using all this information an energy level pattern for the e-states could be built up, accounting for all the observed transitions, see Figure 5.8

5.3.3 18.9GHz; J=$\frac{5}{2}$(f)-$\frac{3}{2}$(f) Transitions

The energy levels for this state were the simplest to determine because the J=$\frac{3}{2}$(f)-$\frac{1}{2}$(f) had already been assigned. The spectra were measured and at the same time double resonances were established to give the Table 5.2 and the energy level diagram in Figure 5.9. The assignment was a simple progression of the assignment of the other two f-states based on selection rules. There is no Zeeman information on the 18.9GHz transitions because the antenna used cannot be orientated easily parallel to Earth's magnetic field so that any observed patterns would be a mixture of the $\Delta M_F = 0$ and $\Delta M_F = \pm 1$, and too complicated to analyse.

5.4 Independent Hyperfine Fitting

It has become apparent that in order to understand the spectrum of NO-HF something more than has been presented so far is required. The structure of the spectrum for the e-states conspires against us to hide much of the information that could be used to determine the assignment. The key to understanding the disposition of the energy levels came by simplifying the problem and considering each of the fine structure states to be independent of the others.

If the hyperfine structure of each fine structure level is considered independently of all the others then the hyperfine matrix elements, found in Appendix B, reveal that the expressions are determined by a factor which depends on the coupling of angular momenta, and a term containing the physical interactions. The first part consists of Wigner 6-j symbols and other terms in

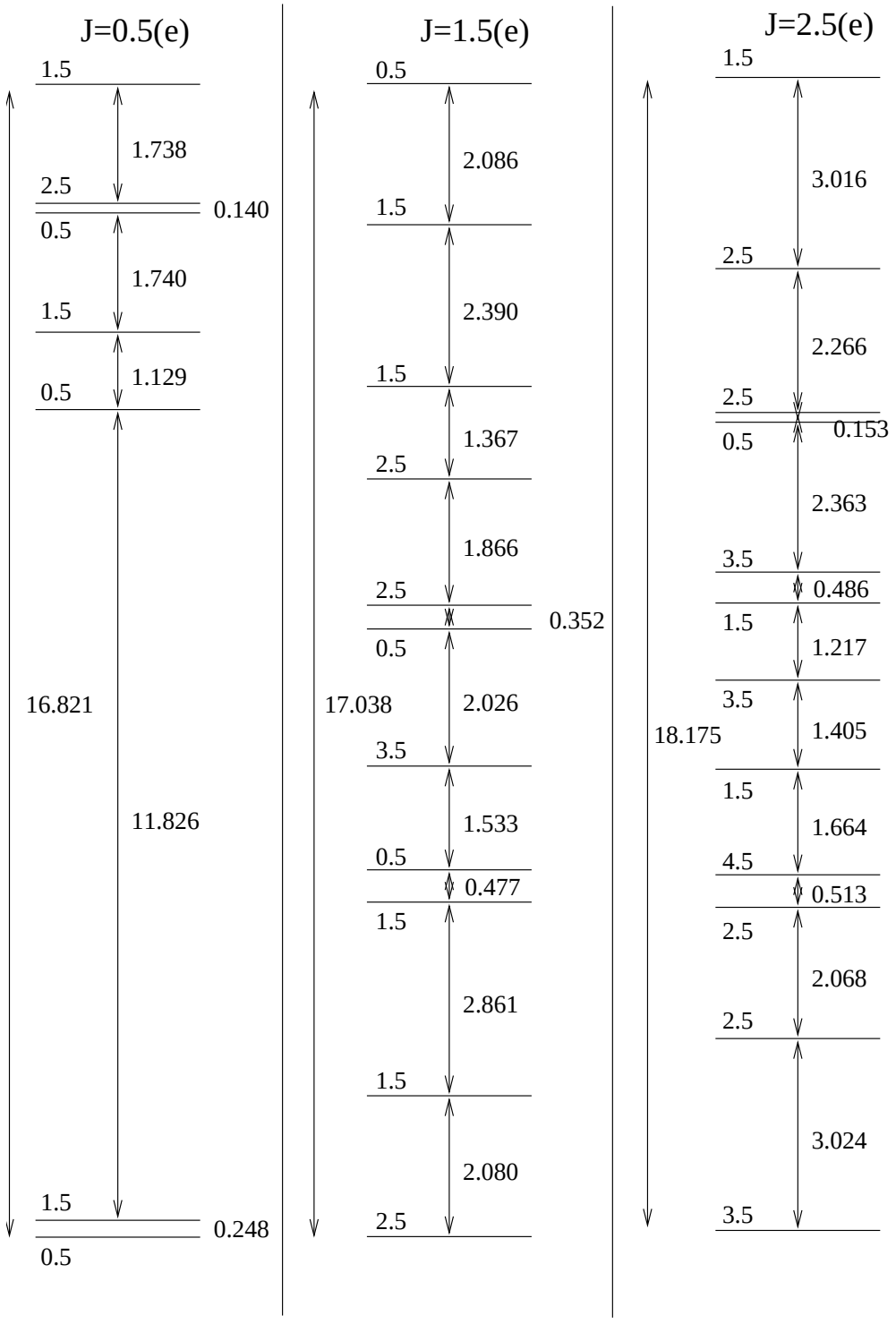

Figure 5.8: Energy Level Diagram for the e-states of NO-HF. The levels are marked with the total angular momentum quantum number, F. The spacings are in MHz and each column of fine structure levels is individually scaled.

$\frac{1}{2},0,\frac{1}{2}$	$\frac{1}{2},1,\frac{1}{2}$	$\frac{1}{2},1,\frac{3}{2}$	$\frac{3}{2},1,\frac{1}{2}$	$\frac{3}{2},1,\frac{3}{2}$	$\frac{3}{2},2,\frac{3}{2}$	$\frac{3}{2},2,\frac{5}{2}$	$\frac{5}{2},2,\frac{3}{2}$	$\frac{5}{2},2,\frac{5}{2}$	$\frac{5}{2},3,\frac{5}{2}$	$\frac{5}{2},3,\frac{7}{2}$	$\frac{7}{2},4,\frac{7}{2}$
									18 940.452		$\frac{7}{2},4,\frac{9}{2}$
										18 939.320	$\frac{7}{2},4,\frac{5}{2}$
							18 940.814	18 940.092	18 935.871		$\frac{7}{2},3,\frac{5}{2}$
								18 939.649		18 934.649	$\frac{7}{2},3,\frac{7}{2}$
					18 943.932	18 943.357	18 921.984		18 917.035		$\frac{5}{2},3,\frac{5}{2}$
						18 943.025		18 920.928		18 915.933	$\frac{5}{2},3,\frac{7}{2}$
			18 943.549				18 917.865				$\frac{5}{2},2,\frac{3}{2}$
				18 942.463				18 916.744		18 911.743	$\frac{5}{2},2,\frac{5}{2}$
	18 943.743				18 928.887	18 928.307					$\frac{3}{2},2,\frac{3}{2}$
		18 942.992		18 931.604		18 927.982					$\frac{3}{2},2,\frac{5}{2}$
			18 928.237								$\frac{3}{2},1,\frac{1}{2}$
				18 927.137		18 923.514					$\frac{3}{2},1,\frac{3}{2}$
		12 243.440		12 254.831	12 257.874	12 258.455	12 279.822	12 280.552	12 284.774	12 285.551	$\frac{3}{2},2,\frac{5}{2}$
	12 246.431	12 246.858	12 257.555	12 258.246	12 261.298	12 261.879	12 283.238	12 283.967	12 288.189		$\frac{3}{2},2,\frac{3}{2}$
12 244.779		12 249.271	12 259.969		12 263.702	12 264.283	12 285.651	12 286.381			$\frac{3}{2},1,\frac{3}{2}$
12 248.527	12 252.598	12 253.020	12 263.716	12 264.400	12 267.454		12 289.399				$\frac{3}{2},1,\frac{1}{2}$
12 288.156	12 292.221	12 292.648	12 303.346	12 304.037	12 307.082						$\frac{1}{2},1,\frac{3}{2}$
12 290.558	12 294.629	12 295.051		12 306.440	12 309.485						$\frac{1}{2},1,\frac{1}{2}$
12 292.374	12 296.440	12 296.867	12 307.561	12 308.255	12 311.298	12 311.879					$\frac{1}{2},0,\frac{1}{2}$

Table 5.2: Diagram illustrating the energy levels with the observed transitions of the J=$\frac{3}{2}$(f)-$\frac{1}{2}$(f) and J=$\frac{5}{2}$(f)-$\frac{3}{2}$(f), showing the connections between the states. The J=$\frac{1}{2}$(f) and the J=$\frac{5}{2}$(f) levels are spaced vertically as the 12GHz and 18GHz groups respectively. The J=$\frac{3}{2}$(f) levels are spaced horizontally. The quantum numbers in the margins are the quantum numbers F_N,F_F,F

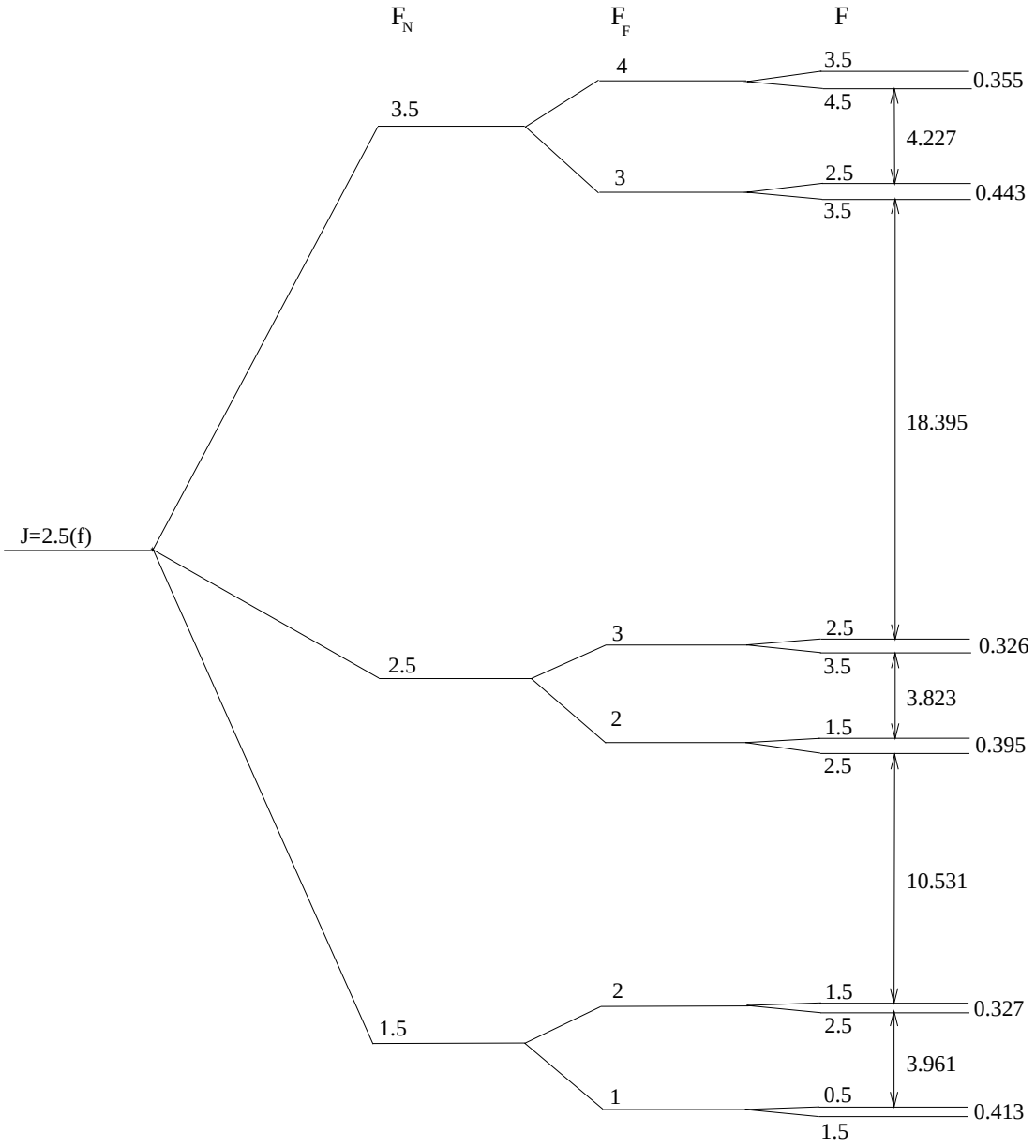

Figure 5.9: Energy Level Diagram of the J=$\frac{5}{2}$(f) State of NO-HF. The splittings are in MHz.

the various total angular momenta, for example, the nitrogen matrix elements are determined by

$$(-1)^{J'+I_N+F_N}\left\{(2J'+1)(2J+1)\right\}^{\frac{1}{2}}\left\{I_N(I_N+1)(2I_N+1)\right\}^{\frac{1}{2}}\begin{Bmatrix} F_N & I_N & J \\ 1 & J' & I_N \end{Bmatrix} \tag{5.4}$$

which can all be explicitly evaluated for a given hyperfine level of a fine structure state. The other part is a linear combination of the matrix elements of the hyperfine interaction in the fine structure basis involving the eigenvectors of the fine structure as the coefficients. This factor will be a constant for a given fine structure level.

By taking the calculated coefficients of the hyperfine matrix elements it is possible to fit the observed hyperfine levels in a given fine structure state with four constants that represent the effect of the nitrogen, hydrogen and fluorine nuclei. Nitrogen having two constants, one for the magnetic hyperfine and the other for the electric quadrupole these having different functional forms, except in the J=$\frac{1}{2}$ states which have no quadrupole. The fitted constants are given in Table 5.3 and constants for the magnetic hyperfine include an extra $\sqrt{\frac{2J(2J+2)}{2J+1}}$ from the 3-j symbol $\begin{pmatrix} J & 1 & J' \\ -K_a & q & K'_a \end{pmatrix}$ in the matrix element, see Equation 4.15. The quadrupolar constant is multiplied by a J-dependent value derived from $(-1)^{J-K_a}(2J+1)\begin{pmatrix} J & 2 & J' \\ -K_a & q & K'_a \end{pmatrix}$. It should be stressed that the labelling of the columns of constants for hydrogen and fluorine is based upon the global fit and the reasoning behind this assignment is detailed in Section 5.9.2

The table includes the constants for all the observed fine structure levels because although initially the states are treated as independent they are related. This relationship derives in two ways. The first and most important part is the parallel(q=0) and perpendicular(q=$\pm$1) components of the tensor operator $T^1_q(\boldsymbol{X})$, explained in more detail in Section 5.5 which are manifested as the $\Delta K_a = 0$ and the $\Delta K_a = \pm 1$ parts of the hyperfine matrix elements respectively. They differ in the Wigner 3-j symbol mentioned above which when evaluated shows that for $\Delta K_a = 0$ is proportional to K_a whereas the $\Delta K_a = \pm 1$ is proportional to $(J + \frac{1}{2})$, having eliminated any

J(e/f)	Nitrogen	Fluorine	Hydrogen	Quadrupole	σ(kHz)
$\frac{5}{2}$(e)	-63.0153	-26.6296	41.0719	-7.0580	16.33
$\frac{3}{2}$(e)	31.6169	-15.5553	35.5350	-2.8723	14.17
$\frac{1}{2}$(e)	8.0131	-4.5568	26.0241	-	20.98
$\frac{1}{2}$(f)	117.0701	16.2080	11.2358	-	23.70
$\frac{3}{2}$(f)	188.6846	25.9773	4.0056	-2.7726	14.87
$\frac{5}{2}$(f)	273.8187	34.9267	-3.0487	-6.7188	24.28

Table 5.3: The constants obtained by fitting the hyperfine pattern of each fine structure level independently in MHz.

common terms. The perpendicular components thus have an extra $(J+\frac{1}{2})$ dependence over the parallel components with $-(J+\frac{1}{2})$ for the e-states and $+(J+\frac{1}{2})$ for the f-states. The $(J+\frac{1}{2})$ dependence is illustrated in the Figures 5.10 and 5.11. The expectation is that the constants derived for the different nuclei can be expressed as an equation linear in $(J+\frac{1}{2})$ where the constant is the parallel component and the coefficient of $(J+\frac{1}{2})$ is the perpendicular component. However it turns out that the fine structure coefficients themselves can be well represented by

$$c_j = c_j^0 \pm c_j^1 \left(J+\frac{1}{2}\right) + c_j^2 \left(J+\frac{1}{2}\right)^2 + \cdots \tag{5.5}$$

As each hyperfine parameter in Table 5.3 is actually a linear combination of terms consisting of each hyperfine basis function multiplied by the eigenvector coefficients from the fine structure matrix. The dependence of these coefficients on J is illustrated in Figure 5.12 using the values of the eigenvector coefficients from Table 5.4.

The constants from the individual fine structure state fitting can thus be related with a power series in $(J+\frac{1}{2})$

$$a \pm \left(J+\frac{1}{2}\right) b + \left(J+\frac{1}{2}\right)^2 c \pm \left(J+\frac{1}{2}\right)^3 d \tag{5.6}$$

where the $\pm$ is the difference between the e and f parity states, - for e-states and + for f-states.

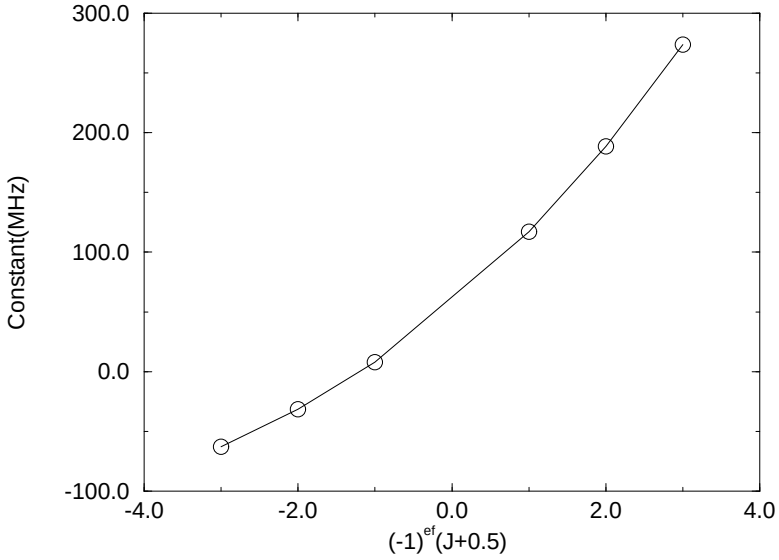

Figure 5.10: Graph illustrating the dependence of the nitrogen magnetic hyperfine parameter for the individual rotational levels on (J+$\frac{1}{2}$)

The use of this equation relies on the fact that the J dependence of the fine structure states is not very strong. This can be confirmed by examining the table of eigenvector coefficients from the fitting program, in Table 5.4. There are two important points that the table illustrates. Firstly the coefficients for the fine structure states do not change significantly with the rotational angular momentum, J. Secondly it illustrates the effect of the quenching of the orbital motion because the first row for each state contains coefficients for the $\Omega = \frac{1}{2}$ basis functions and the second row contains the coefficients for the $\Omega = \frac{3}{2}$ basis functions. Comparing these for the first two basis functions in the J=$\frac{1}{2}$(e) state it is clear that the components almost entirely cancel, 0.32 versus 0.34. In the second two basis functions this is not the case, 0.48 versus 0.22, so there will be a reduction in the net magnetic moment due to the orbital motion of the electron. The point at which the coefficients of the $\Omega = \frac{1}{2}$ and $\Omega = \frac{3}{2}$ states are equal is when the electron resides in either a Π_x or Π_y orbital.

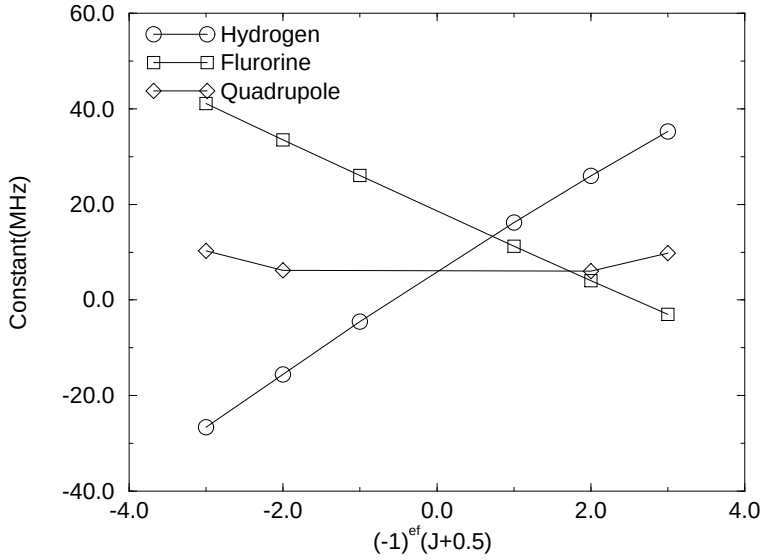

Figure 5.11: Graph illustrating the dependence of the hydrogen and fluorine parameters fitted for individual rotational levels on (J+$\frac{1}{2}$)

At this point one important factor became apparent which influences the view on the fits. There is no way in the fitting process to distinguish between the splittings due to the hydrogen and fluorine nuclei. This is a useful tool for testing the validity of the program because if the assignments of the hydrogen and fluorine quantum numbers are reversed the same fit is obtained. The result must be the same because they rely on the coupling of a nuclear spin of the same magnitude to the total angular momentum. In the final result the provenance of the constants can only be distinguished by physical arguments about the positions of the nuclei in the complex. It raises the question about the assignment of the 12GHz lines whether the splittings attributed to hydrogen and fluorine are in that order. The attribution of the constants obtained here to hydrogen and fluorine will be explained later from the values of the constants from the fitting of the complete data set.

Initially it was only possible to fit constants to the hyperfine energy levels of the two fine

J	Parity	$\|\frac{1}{2},\frac{1}{2}\rangle$	$\|-\frac{1}{2},-\frac{1}{2}>$	$\|\frac{1}{2},-\frac{1}{2}\rangle$	$\|-\frac{1}{2},\frac{1}{2}\rangle$
		$\|\frac{1}{2},\frac{3}{2}\rangle$	$\|-\frac{1}{2},-\frac{3}{2}>$	$\|\frac{1}{2},-\frac{3}{2}\rangle$	$\|-\frac{1}{2},\frac{3}{2}\rangle$
0.5	e	0.32176	0.32176	0.48263	-0.48263
		-0.33724	0.33724	-0.22319	-0.22319
0.5	f	0.33504	-0.33504	0.47393	0.47393
		-0.33073	-0.33073	-0.23185	0.23185
1.5	e	-0.31568	-0.31568	-0.48639	0.48639
		0.34007	-0.34007	0.21925	0.21925
1.5	f	-0.34228	0.34228	-0.46891	-0.46891
		0.32699	0.32699	0.23658	-0.23658
2.5	e	0.30996	0.30996	0.48981	-0.48981
		-0.34265	0.34265	-0.21555	-0.21555
2.5	f	-0.34992	0.34992	-0.46337	-0.46337
		0.32288	0.32288	0.24158	-0.24158

Table 5.4: Coefficients of observed fine structure states $|K_a, \Omega\rangle$ from the eigenvectors of the fine structure matrix at an angle of 40° with a Renner-Teller parameter of -9400.0GHz.

structure states that had been assigned, the $\frac{3}{2}$(f) and $\frac{1}{2}$(f) which illustrated the use of this model in the assignments. A simple linear dependence of $(J + \frac{1}{2})$ was assumed from which it was possible to predict the constants for the $\frac{1}{2}$(e) state. By simulating the energy levels for the $\frac{1}{2}$(e) state using the predicted constants it was apparent that the disposition of the levels correlated well with the observed energy level diagram constructed by double resonance experiments. The matching up between the energy level diagram then allowed the assignment of the $\frac{1}{2}$(e) state total angular momentum F quantum numbers. It is worth noting that in the J=$\frac{1}{2}$(e) state the parallel and perpendicular contributions almost cancel for nitrogen giving a small splitting. Initially fitting for the e-states was attempted using the intermediate quantum number labelling scheme which had worked well for the f-states. However when attempts were made to then fit the assigned levels they failed miserably. On examination of the output from the fitting it was clear that the intermediate quantum numbers associated with the levels were no longer good. The

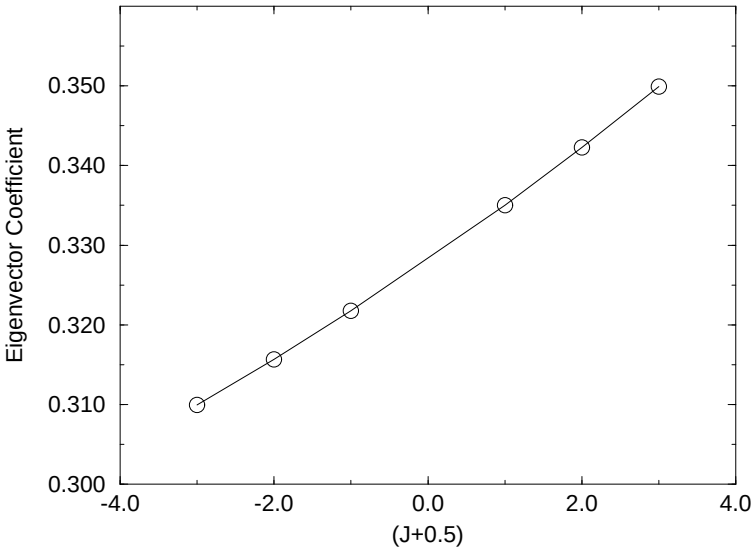

Figure 5.12: A graph illustrating the dependence of the eigenvector coefficients for the fine structure state $\langle K_a = \frac{1}{2}, \Omega = \frac{1}{2}|$ on (J+$\frac{1}{2}$).

algorithm in the program was using the level with the largest coefficient in the eigenvector to label the level. When the levels are close to being evenly mixed it is possible for the dominant state to change as the constant is altered during fitting swapping the labelling of the state and preventing the fit from working. The program was changed to order the energy levels using only their total angular momentum, F, and their frequency shift from the lowest energy level. The fitting was now effective and the constants could be added to those already obtained.

The interesting thing here is that the ratios of the couplings due to the various nuclei within the molecule is changing as a function of the rotational fine structure state. The cause of the change in the coupling is not easy to see but it really depends on the difference between the parallel and perpendicular terms. Examining the first two rows of the Table 5.5 which essentially contain the parallel and perpendicular interactions. The nitrogen constants illustrate that for the $\frac{1}{2}$(e) state the effect of the nitrogen hyperfine will be very small because the two constants are of

Constant	Nitrogen	Fluorine	Hydrogen	Quadrupole
a	57.1497	5.9983	18.5811	2.9634
b	54.2665	10.4213	-7.4029	-0.07369
c	5.3592	-0.1900	0.0478	0.7869
d	0.2077	-0.0122	0.0055	-

Table 5.5: The parameters obtained when the constants from fitting the hyperfine levels are modelled by powers of $(J + \frac{1}{2})$.

similar sign and magnitude and cancel each other out. The hydrogen terms also largely cancel but for fluorine the terms are of opposing sign so in the $\frac{1}{2}$(e) state they reinforce creating a large splitting. It is difficult to see how the relationship between the constants could be predicted before measuring them.

Finally the constants for the remaining states were predicted. Again these were put into the individual fine structure fitting program and allowed to predict the hyperfine energy level diagram. These calculated energy levels correlated well with the energy level diagrams obtained from double resonance. There was close correspondence between the levels and where the total angular momentum quantum numbers were known there was a match. In the cases where the total angular momentum quantum numbers, F, were not certain it was noticed that the selection rule $\Delta F = 0, \pm 1$ could be applied from which the total angular momentum quantum numbers could be assigned. The results were then put into the fitting program and the results were fitted to yield a complete set of constants listed in Table 5.3.

5.5 Parallel and Perpendicular Components

The magnetic hyperfine interaction can be broken down into two parts, a parallel and perpendicular interaction of a nuclear magnetic moment with the magnetic field arising from the unpaired

electron on NO. The magnetic field due to the unpaired electron is based around the NO internuclear axis and is projected from there onto the a-axis of the complex, see Figure 5.13. The projections are a linear combination of the parallel and perpendicular components of the magnetic moment on the NO axis. The projections being determined by the structural angle between the complex a-axis and the NO internuclear axis.

The physical manifestation of the magnetic field is determined by the constants. The parallel contribution arising from the matrix elements of the hyperfine interactions which are diagonal in the K_a quantum number and the perpendicular contribution from the matrix elements which are off-diagonal in K_a. The interactions are then effectively separated in the independent J state fitting, the values of the contributions there reflecting the combination of the hyperfine constants via the fine structure eigenvectors that make up the state. The J dependence of the fine structure states is small making the identification of the parallel and perpendicular components easier.

5.6 The unusual energy level pattern of the $\frac{1}{2}$(e) State

The really perplexing nature of the e-state levels took a long time to understand. The problem is that to have some chance of assigning the energy levels a coupling scheme has to be assumed but the assumed coupling scheme will prejudice any perceptions about the distribution of energy levels. This prejudice then makes an assignment impossible as an unsuitable coupling scheme is forced onto the energy levels.

The coupling scheme which was being initially used was that which fitted the f-states with a large nitrogen coupling, a smaller splitting initially attributed to the hydrogen and the smallest splitting initially attributed to the fluorine. A nitrogen splitting which is much larger that the other splittings tends to create an energy level pattern which can be broken down into a two blocks, for a J=$\frac{1}{2}$ state, one containing four levels and the other containing three levels. However the observed $\frac{1}{2}$(e) diagram from double resonance had five levels in a block and then one level

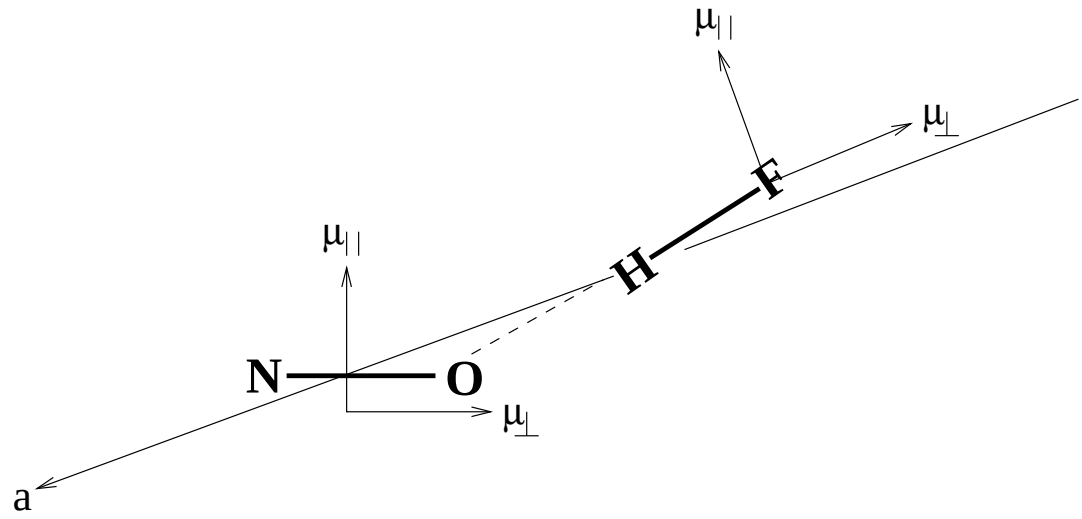

Figure 5.13: Illustration of the parallel and perpendicular fields at a nucleus.

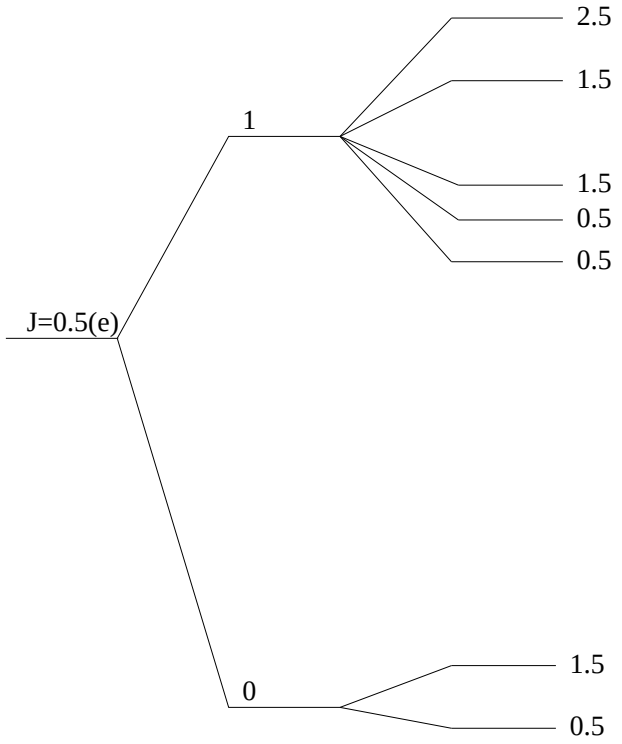

Figure 5.14: Coupling Diagram for the $\frac{1}{2}$(e) Fine Structure State with a large interaction for one I=$\frac{1}{2}$ nucleus and a small splitting for the I=$\frac{1}{2}$ and I=1 nuclei which have coupled to create a resultant angular momentum.

situated 11MHz away, the position of the final level having not been tied down at this point. The confusion was how the coupling scheme in use for the f-states could hope to produce an energy level diagram with such a structure. The only explanation would be a completely different coupling scheme.

A scheme with such a pattern can be created by taking the interaction of one of the spin $\frac{1}{2}$ nuclei as being large compared to the other nuclei and coupling that first, to J, to split the fine structure into two, The other two nuclear spins are then coupled to one another with a similar interaction energy to create a resultant nuclear spin which is added onto the other splitting. This resultant has two allowed values of $\frac{1}{2}$, and $\frac{3}{2}$ which splits the intermediate level of F=1 into five components and the intermediate level of F=0 into two. An assignment based on this structure was tested with one of the lower two levels missing which fitted the observed spectrum. This coupling scheme was evidently valid for this fine structure state. The position of the remaining line could then be predicted and was subsequently observed.

5.7 The Least Squares Fitting Program

The theory that was described in Chapters 3 and 4 has all been implemented in a global fitting program, which consists of some eight thousand lines of Fortran and C code. The program in fact consists of two separate programs, one written in C and one in Fortran. The C program exists purely to parse the input file and convert it into a form suitable for the Fortran program. The decision to do this is a reflection of the weakness of Fortran at string operations. It allows the use of a more verbose input file which is easier to understand. The parser incorporates some error checking to reduce the chance of a mis-entered line affecting the fit. The output from this program is then passed to the main program.

The Fortran program can be divided into two basic parts, initialisation routines and the routine that reside in the fitting loop. The initialisation routines are all called once at the commence-

ment of execution and fill in a set of matrices containing the matrix of the fine structure basis functions for each parameter. The results are all stored in a contiguous block of memory so that to increase the highest rotational level available only one header file has to be changed. The initial 6-j terms of the hyperfine interaction are calculated at this point.

The fitting cycle is started by creating the complete fine structure matrix which is then diagonalised, the eigenvalues and eigenvectors begin stored for later use. The hyperfine matrix for each interacting nucleus is filled and the matrices for a given total F are constructed and diagonalised. The eigenvalues and eigenvectors are again stored for use later. The non-linear least squares routine is now started and it requires the calculated transition frequencies and the derivatives of the transition frequencies with respect to the parameters using the saved eigenvalues and eigenvectors. These are then passed to a fitting routine based on the Levenberg-Marquardt algorithm[11] which produces optimised parameters. The fitting cycle is then repeated until either a maximum iteration count is reached or the χ^2 converges to an acceptable level.

The program was designed with the fine and hyperfine structure separated with the hyperfine added to the fine structure as a perturbation. The fine structure states, ϕ_i, exist as a linear combination of the fine structure basis functions

$$\phi_i = \sum_k c_k |\eta\Lambda; S\Sigma; JK_a\rangle_k \tag{5.7}$$

The peturbation due to the hyperfine interaction of an unperturbed state is then given by

$$E^{(1)} = Y_{hf} \sum_k \sum_l c_k c_l \langle \eta\Lambda; S\Sigma; JK_a|_k T^1_q(\boldsymbol{X})|\eta\Lambda; S\Sigma; JK_a\rangle_l \tag{5.8}$$

where Y_{hf} is a numerical factor that depends on the hyperfine energy level and contains 6-j symbols and numerical factors in the various total angular momenta. $T^1_q(\boldsymbol{X})$ is as defined in Equation 4.1. The hyperfine interaction is then calculated as a series of small matrices, two 1×1, two 3×3 and a 4×4, each of which has the same total angular momentum. These matrices are diagonalised to give the hyperfine perturbations for a particular fine structure state which can be added to the fine structure energy to create the overall energy levels.

It would be perfectly possible to construct a matrix containing both the fine and hyperfine structure and diagonalise that. However it leads to significantly larger matrices and as the diagonalisation procedures scale as n^3, where n is the dimension of the matrix, the process would be about 1500 times slower, as normal execution takes about two minutes this would become prohibitive. The implementation of the separated hyperfine interaction is more difficult but the gains do justify the extra complexity in the program code.

The use of one particular coupling scheme within the program is not a problem because all the coupling schemes are equivalent in calculating the energies. The coupling schemes are normally chosen to minimise the magnitude of any off-diagonal elements. The program was written when the 12GHz lines had been discovered so it makes use of the coupling scheme for those levels but it could equally well be written to use the coupling scheme which is optimal for the J=0.5(e) state. In the final analysis the program was changed to use ordering of the energy levels of the same total angular momentum, F, instead of the intermediate quantum numbers, F_N/F_H. This removes any ambiguity over the intermediate quantum numbers which are not well defined in the e-states.

5.8 Results of the Least Squares Fitting

Now that an assignment of all of the hyperfine levels for all the observed J states is available, with the indication from the capability to fit the individual hyperfine levels that it is possible, a global fit of all the data is required. Modifications to the fitting program were necessary to change the handling of the assignment of quantum numbers to the e-states, to rely only on the total angular momentum quantum number and the order in which the levels occur. The complete data set consisted of the 157 lines measured in the microwave and ten lines derived from the infrared spectrum[6] with reduced weights.

The initial fits were made by floating the rotational constants A, $\frac{1}{2}(B + C)$, the Renner-

Teller parameter ϵ_2, the nitrogen hyperfine constants a, d and eQq_0, and the first of the dipolar constants for hydrogen and fluorine. The dipolar constant used is derived in Section 4.6 with the matrix elements being given in Appendix B.3. The standard deviations from these fits were approximately 3MHz indicating that there was a systematic problem, which could be attributed to a deficiency in the model for the hyperfine. The first candidate for inclusion was the addition of a Fermi-Contact parameter for the hydrogen and fluorine nuclei. The justification being that the Fermi-Contact parameter in hydrogen is 1.4228GHz,[10] if only a few percent of electron transfer takes place to the hydrogen from the nitric oxide the parameter will still be on the order of a few megahertz.

On adding a Fermi contact parameter to each of the hydrogen and fluorine nuclei the fitting improved substantially to yield a standard deviation of about 40kHz. The simple independent fine structure state fitting of the hyperfine levels gave standard deviations between 14 and 24kHz, see Table 5.3. Any fit relying on constants which use hyperfine theory giving matrix elements preceeded by the same products of terms in the various total angular momenta can be expected to do no better than these standard deviations and given that all the levels are being fitted simultaneously a much worse result could be expected. At this juncture various additional constants were added to the analysis in an attempt to improve the fit. These were the terms off-diagonal in Λ by ± 2 from the dipolar term for hydrogen and fluorine, and the off-diagonal term in the spatial relationship operator where q=± 1,± 2, see Appendix B.3. None of these terms caused any improvement in the fits. The next term to be added was the nuclear spin-spin term between hydrogen and fluorine, which in hydrogen fluoride is 143.375kHz.[12] As a potential term to correct the errors in the fit this had the greatest likelihood of being effective because it uses different theory to the other terms and is not prefaced by the same series of coupling coefficients. However its inclusion did not result in any improvement in the quality of the fits.

The final implication is that the fit has attained the optimum level. It is possible to test many other parameters for their effect on the quality of the fit in the hope that the standard deviation

may be reduced, for example the nuclear spin rotation terms could be added. However the constants that are being added become less and less physically significant. It may be that there is insufficient information contained within the data to support another constant.

The fits are controlled by the energy level spacings within each of the fine structure states and these separations can be very well represented by just four constants. In the f-states the nitrogen splitting has at most two splittings that can be measured which means that most of the observed hyperfine transitions are not giving any new data on the nitrogen hyperfine. The number of determinable parameters for a nucleus is therefore limited. The fact that the hyperfine in each of the states can be fitted by three or four constants indicates there is very little extra data above that already determined which can be extracted. The global fit can make use of the differences between the rotational states which gives the separation into the parallel and perpendicular components of the interaction.

This is well illustrated in NO where once the fits achieve a certain quality the number of parameters used increases rapidly, for example, Meerts and Dymanus fit the spectrum of this linear molecule with thirteen constants.[13] It is possible to include many terms in the fine structure arising from the interaction of the Π states with excited electronic states of Σ and Δ form.

5.8.1 Angular Fitting

The angle which is used throughout the fitting program describing the angle between the NO axis and the a-axis of the complex is not a parameter that can easily be fitted. The other parameters are essentially linear in their effect being multiplied by a matrix of fixed values. However the angle is a complicated function involving sines and cosines and would require some form of numerical method to determine the rate of change of a transition with respect to the angle, which is a difficult term to calculate. The simplest method would be a tangent method by calculating the matrices at slightly different angles and comparing the results, to get the gradient, a slow and computationally intensive method.

The determination of the optimum angle was carried out by using a script, written in Perl, to produce data files iterated over all the angles in a particular range. The fitting program was run on these files so that the other parameters were fitted using least squares optimisation at fixed angle θ. The standard deviations from the optimisation were then extracted by the program from the output files and the best angle was selected using on the minimum standard deviation.

In addition to the angle that is used throughout the theory describing the relationship between the a-axis of the complex and the NO internuclear axis, a second angle is used as a partial replacement for the lack of centrifugal distortion in the fine structure Hamiltonian. The centrifugal distortion was left out of the fine structure Hamiltonian to simplify an already complex system with an awareness that only the lowest angular momentum levels would be measured and that to these levels the centrifugal distortion would only have a small effect. Once the fitting attained a certain quality it becomes an issue as to whether the inclusion of some term to model the centrifugal distortion is required. Instead of calculating the full interaction an angular momentum dependent angular distortion term was added. This term changes θ to $\theta - \Delta\theta J(J+1)$. This is justified because as the complex rotates faster it will tend towards a linear configuration reducing the observed angle. The $\Delta\theta$ parameter was optimised in the same way as the other angle by iterating until the lowest standard deviation was located.

5.9 Discussion of Fitted Constants

5.9.1 Fine Structure

The fine structure constants determined in the fitting consist of the rotational constants A and $\frac{1}{2}$(B+C), the Renner-Teller parameter ϵ_2, and the angle between the NO-axis and the complex a-axis. The third rotational constant $\frac{1}{2}$(B-C) is not floated because it is not well determined by the observed transitions so its value is fixed at a reasonable figure. The ability to float the A constant is unusual for the set of data that is observed. In a conventional asymmetric top the observed

Constant	Value(GHz)
$\frac{1}{2}(B-C)$	0.055
ζ	3687.44
$< A^{+} >$	352.958
$< B^{+} >$	10.70751
$< C^{+} >$	10.364
$< \zeta^{+} >$	9212.254357
$E_{\Sigma-\Pi}$	$3.954175581 \times 10^{6}$

Table 5.6: Fine structure constants used as fixed values during the fitting of the microwave spectrum of the open shell van der Waals complex NO-HF.

transitions would be categorised as a-type using the component of the electric dipole moment aligned along the a-axis, μ_a, to cause the transition with the selection rule that $\Delta K_a = 0$. These levels are spaced by approximately (B+C)(N+1) and do not directly determine the value of the A constant. NO-HF is not a simple asymmetric top when the effect of all the electronic angular momenta are included there are a number of deviations from the simple asymmetric top. An examination of the symmetrised fine structure matrix in Table 3.2 shows that there is a term in A on the diagonal which will have a constant effect throughout the J states. There are also terms in A situated on the off-diagonal which will have different effects in the different rotational states and provide the necessary data on A. If the quality of fit for A is compared to $\frac{1}{2}$(B+C) it is not as good because it is only determined from the indirect effect.

The ability to fit the rotational constant A is important particularly when varying the angle, θ because the value of the A constant is directly related to the angle being largest at small angles.

The angle together with the rotational constants and the assumption that the complex is planar should allow estimation of the structure of the complex, primarily the distance between the center of masses of the two monomers, assuming that the bond lengths of the monomers remain

Constant	Best Fit	N constant
	Value	Value
A (GHz)	72.23(1)	89.3(4)
$\frac{1}{2}$(B+C) (GHz)	3.364566(5)	3.3448(3)
ϵ_2 (GHz)	-10 449.32(4)	-9 741.0(7)
θ(°)	49.0	36.9
$\Delta\theta$ (°)	0.0	0.02
σ (kHz)	39.41	1101.71

Table 5.7: Fine structure constants from the fitting of the microwave spectrum of the open shell van der Waals complex NO-HF. The best fit is when the nitrogen hyperfine constants are floated and the other fit is when they are held fixed.

unchanged. This leaves one remaining degree of freedom in the position of the hydrogen atom because it does not have to lie on the line connecting the oxygen and fluorine nuclei. However because of the small mass of the hydrogen atom changing the position has little influence on the rotational constants, making the absolute position difficult to determine.

There are two sets of fitted constants in the Table 5.7 one of which corresponds the optimum fit discussed above and the other to the fit that is obtained when the nitrogen hyperfine constants are fixed at their values in the monomer. The reasons for the two approaches are explained in the next section. The main concern here is that the two different approaches give widely different values for the structural angle in the complex and therefore very different structures.

The fine structure angle obtained, from the fully optimised fit, is 49° while that from the fits with the fixed nitrogen hyperfine parameters is 36.9°. There is now a split as to which of the two sets of values is closest to the true set of data. The problem is probably being caused by an incomplete Hamiltonian. The code is correct because it can fit the NO monomer spectra to ∼50kHz. The poor value for the fit is because of the lack of centrifugal distortion in the

Hamiltonian.

The structure of NO-HF is at the moment still very open to debate because there are many other possible combinations of the components that will satisfy the observed rotational constants. The orientation of the hydrogen fluoride unit at the oxygen of the NO is not proved and it would require isotopic substitution to determine a rigorous structure. An avenue that has been considered are the three available nuclei for isotopic substitution with convenient alternative isotopes. These are the hydrogen with D(I=1), nitrogen with ^{15}N(I=$\frac{1}{2}$) and oxygen with ^{18}O(I=0). The trouble is that one of these nuclei, Deuterium, would further complicate the spectra by increasing the number of hyperfine levels and requiring the evaluation of the electric quadrupole on additional nuclei.

The Renner-Teller parameter indicates the relative energy of the in plane A' orbital and out of plane A'' orbital. Fawzy et al[6] could not determine the sign of the Renner-Teller parameter because the fine structure energy levels seen in the infrared spectrum only differ in parity when the sign of the constant is changed. They assumed that the interaction between the monomers was dominated by an attractive electrostatic interaction and so anticipated a positive value for the Renner-Teller parameter. Note that their Renner-Teller parameter is defined with the opposite sign to ours. The sign of the Renner-Teller parameter can be determined from the microwave spectrum because of its effect on the ordering of the hyperfine energy levels. The constant is very large and negative so the in plane configuration is significantly stabilised with respect to the out of plane configuration. The presence of the HF is acting to stabilise the in plane orbital because it places the maximum amount of electron density into the hydrogen bond between the monomers.

Legon et al[14] have studied the nature of hydrogen bonds extensively and have formulated a basic rules for the gas phase structure of dimers involving the hydrogen halides, B-HX.

1. the axis of the HX molecule coincides with the supposed axis of a non-bonding pair as conventionally envisaged,

or, if B has no non-bonding pairs but has π-bonding pairs,

2. the axis of the HX molecule intersects the internuclear axis of the atoms forming the π-bond and is perpendicular to the plane of symmetry of the π-orbital.

Rule 1. is definitive when B has both non-bonding and π-bonding electrons.

The basis of the rules seems to be that the hydrogen moving to place itself close to the regions of highest electron density. By these arguments the hydrogen fluoride molecule in NO-HF should align itself along the axis of the π^* orbital confirms the observation. This is also compatible with the A', in plane orbital being the ground state and agrees with the conventional theories of hydrogen bonding. In Ar-NO because there is no electrostatic effect to favour the presence of the unpaired electron in the plane of the complex the repulsive effects dominate[15] so there is a slight preference for the electron to be in the out of plane A'' orbital.

The substantial value of the Renner-Teller parameter, ϵ_2, of $\sim -300\text{cm}^{-1}$ indicates that there is a significant interaction between the monomers. It can be expected that the actual binding energy of the complex will be much greater than the value of ϵ_2.

5.9.2 Hyperfine Constants

Nitrogen Constants

In Table 5.8 are the values of the three nitrogen hyperfine constants that were varied in the fitting of NO-HF. Only three of the six available constants are floated in the fits because there is only a limited amount of data available on the nitrogen hyperfine in the observed data. Several of the constants have similar functional forms, notably the nuclear spin-orbit term, the Fermi contact term and the spin-spin dipolar term diagonal in electronic state. They therefore cannot be distinguished from one another so only the Fermi contact parameter was varied. The parameters are changed only slightly by the effects of complexation with the exception of the spin-spin d constant which connects the states that differ in orbital state. This is changed from 112.6125MHz in

Constant	Best Fit
	Value(MHz)
b_F	22.86(1)
d	70.46(3)
eQq_2	17.4(2)

Table 5.8: The nitrogen hyperfine constants from the fitting of the microwave spectra of the complex NO-HF at an angle of 49.0° with a $\Delta\theta$ of 0.0°.

the monomer, see Table 5.9, to 70.46MHz in the complex. The expectation for the nitrogen con-

Constant	Value(MHz)	Constant	Value(MHz)
a	84.2755	eQq_0	-1.8728
b_F	20.0330	eQq_2	23.2145
c	-58.4277		
d	112.6125		

Table 5.9: The hyperfine constants for the free NO molecule from Mills et al. These values were used if the value of a nitrogen hyperfine constant was not floated during the fits.[3]

stants is that they remain virtually unchanged because although there will be some perturbation of the electronic structure of the NO monomer it should not be that great. The hydrogen fluoride rests close to the charge cloud of the π^* orbital of the NO in the model used where it will perturb the electron density in that region. The perturbed electron density is a relatively long way from the nitrogen nucleus and will therefore be down weighted in its effect on the constants by the $\frac{1}{r^3}$ relationship in the definition of the constants. The values of the constants are dominated by the electron density closer to the nucleus which is held more strongly by the electrostatic field of the nucleus and should not be perturbed on complexation. The change in the value of the d

Constant	Best Fit	N constant
	Value(MHz)	Value(MHz)
Hydrogen		
Dipolar	5.2(1)	6.3(2)
Fermi Contact	15.5(2)	15.5(4)
Fluorine		
Dipolar	3.730(8)	5.3(3)
Fermi Contact	-2.71(2)	-1.8(7)

Table 5.10: The hyperfine constants for the hydrogen and fluorine nuclei from the fitting of the microwave spectra of the complex NO-HF at an angle of 49.0° with a $\Delta\theta$ of 0.0°.

constant from 112 MHz in the monomer to 70 MHz in the complex is thus much larger than we would anticipate. The cause is probably the incomplete nature of the Hamiltonian for the complex there being many other interactions that could be added into the Hamiltonian.

A measure employed to try to compensate for this anomaly was to attempt fitting when the values of the nitrogen hyperfine constants were fixed at their values for the NO monomer. The results of both fits are presented in the appendices Sections D.1 and D.2.

The small change in the quadrupole constant is unsurprising as a molecule with a large dipole moment has been placed in close proximity to the NO subunit. The electric field gradient at the nitrogen nucleus will be changed slightly modifying the value of the constant. In N_2-HF[16] the quadrupole constants are changed by about 10% from value in the nitrogen molecule, with the two nitrogen coupling constants no longer being equivalent.

Hydrogen and Fluorine Constants

There are two constants fitted for each of the hydrogen and fluorine nuclei, one probes the dipolar interaction between the electron and nuclear magnetic moments and the other is the Fermi

contact interaction. The Fermi-contact parameter is of extreme interest because it measures the transfer of unpaired electron density from the anti-bonding orbital on nitric oxide to the hydrogen atom. The method for attributing the interaction to each of the nuclei has so far been based purely on the magnitude of the splittings which is incorrect. The actual values of the fitted constants indicate which nucleus is which. The hydrogen nucleus should have the large positive value for the Fermi-contact parameter because it is closed to the nitric oxide and can have electron density transferred to it. The small negative Fermi-contact parameter is thus associated with fluorine nucleus because it is further away and the Fermi-contact interaction is transmitted by polarisation which changes the sign of the Fermi-contact parameter.[17] The dipolar constants should then scale as $\frac{1}{r^3}$, where r is the distance of the nucleus in question from the unpaired electron. The expectation is that the value for the hydrogen be larger than that of the fluorine.

The determination and attribution of the measured hyperfine splittings to the hydrogen and fluorine nuclei is an arduous task. It is easy to place their orders based on the values of the constants from the global fits but then how do the constants relate back to the splittings observed. The splittings are highly dependent on the linear combination of states. The only way to do this is to fit the calculated energy levels for each individual fine structure state, using only one of the two sets of constants at a time. The results of this are given in Table 5.11.

By comparing these values with those of the individual fine structure fitting in Table 5.3 the source of each of the splittings can be identified and attributed to hydrogen and fluorine. The larger constants which are due to hydrogen cause the small splittings in the f-states. The large splitting in the f-states are then caused by the fluorine nucleus. This is the reverse of the situation that was initially assumed when the interaction of the parallel and perpendicular components of the hyperfine was not fully appreciated. It is still assumed that the stronger interaction is due to hydrogen although in the f-states the hydrogen splittings happen to be small.

State	Fluorine		Hydrogen	
	Nitrogen	Value(MHz)	Nitrogen	Value(MHz)
2.5(e)	-63.9672	-26.0406	-63.9878	41.1018
1.5(e)	-31.5639	-15.1833	-31.5641	33.6528
0.5(e)	8.4905	-4.4946	8.4908	26.1528
0.5(f)	116.9856	16.0972	116.9857	11.1043
1.5(f)	188.5736	25.9747	188.5740	3.6460
2.5(f)	274.0265	34.8893	274.0267	-3.6656

Table 5.11: The hyperfine constants for the individual fine structure states obtained from fitting the energy levels produced by simulating the spectrum with either the assumed hydrogen or fluorine constants from the global fit.

5.10 Charge Transfer Effects

The issue of charge transfer between the monomers in van der Waals complexes and hydrogen bonds is one of great debate. There have been times when charge transfer is thought to have been proved but later refuted. The rare gas hydrogen halide complexes are an example where initially the observed values of the field gradients at the nucleus extracted from the quadrupole constants were attributed to charge transfer. In Kr-HF[8] about half of the observed field gradient at the ^{83}Kr nucleus is attributed to charge transfer from the HF molecule, where 0.5% of an electron in a 4p orbital on krypton is transferred to the HF. Later for the same effect in Xe-HF/Cl[9, 18] the field gradient at the ^{131}Xe nucleus is largely due to the Sternheimer effect.[19–23] There are two Sternheimer effects. The shielding effect where the presence of the nuclear quadrupole distorts the inner electron density to form an opposing quadrupole reducing the observed quadrupole and the antishielding effect where the field gradient due to the hydrogen halide induces a quadrupole moment in the electronic distribution of the rare gas atom increasing the observed quadrupole.

The overall result is that in Xe-HCl at most 0.04% of an electron is transferred to the hydrogen chloride, a value so small that charge transfer is playing a very minor role in the complex.

The other approach is to try to prove charge transfer by ab-initio methods. Stone et al[24] argue that there is no evidence of charge transfer affecting the properties of van der Waals complexes. There is a well established method of analysis for the calculation of the structures of complexes using an expansion of multipoles placed at strategic locations in the monomers.[25–28] These monopoles are then allowed to interact with one another in the presence of a crude hard sphere atom-atom repulsion. The procedure is successful in predicting structures because the electrostatic interaction is strongly orientation dependent. The ability of this to predict structures is argued to not require charge transfer in its models.

Alternatively the interaction can be broken down into its components. The main scheme for doing this is that of Morokuma.[29, 30] The scheme works by calculating the energies of the complexes using differing methods and then deriving from those the various terms in the interaction.

1. taking a simple product of the monomer wavefunctions to give the electrostatic interaction of the complex.

2. taking a product basis with antisymmetrization of the monomer wavefunctions with respect to permutations of electrons within the monomers but not between the monomers. This is optimised with all the integrals that contain overlap of the basis functions between the monomers from which can be extracted the induction energy.

3. taking an antisymmetrized product of the unperturbed wavefunctions to give the exchange repulsion as an extra term.

4. finally taking a fully optimized antisymmetrized product which gives an energy that includes a term due to charge transfer as well.

The charge transfer term that arises from these calculations can be significant particularly for hydrogen-bonded species,[31] although these calculations may be biased by basis set superposition

error which particularly influences the charge transfer terms.[30] The presence of charge transfer in van der Waals complexes is difficult to prove and until now there has been no experimental evidence of it.

The results from the microwave spectrum of NO-HF do show that charge transfer is indeed occuring. The value of the Fermi contact term for the hydrogen nucleus is direct proof that electron density has been transferred into an s-type orbital on the hydrogen so that the unpaired electron has a non-zero probability of being found at the hydrogen nucleus. The value of the Fermi contact parameter in a hydrogen atom is 1.4228GHz.[10] The value in the complex is 15.5MHz, implying that approximately 1.0% of an electron has been transferred into a hydrogen s orbital.

The effect of the Fermi contact at the fluorine is more complex. The negative value of the parameter shows that there is "negative spin density" at the nucleus. In order to get a negative Fermi-contact the interaction has to be transmitted by polarisation rather than directly. The unpaired electron density interacts with the electron in the sp-hybrid based on the fluorine. Due to exchange effects one orientation of the electron will be preferred polarising the electron spins in the bond slightly and creating a slight negative spin density in the fluorine 1s orbital giving a negative Fermi contact term. The effect is explained in Carrington et McLachlan.[17] In fact there will be competing effects with a minimal presence of electron density from the unpaired electron competing with the polarisation effect with the polarisation effect being stronger.

5.11 Ab-Initio

The problem of NO-HF is a difficult one and in the process of trying to understanding the microwave spectra it was felt that ab-initio calculations might help to provide some insight into the structure and properties of the complex.

Ab-initio calculations were carried out on an Intel Pentium desktop computer using the Linux

Basis Set	Method	Angle(°)	Length(Å)	Rotational Constants(GHz)		
				A	$\frac{1}{2}$(B+C)	$\frac{1}{2}$(B-C)
6-31G	HF	27.9	3.39	213.259	3.432	0.028
6-31G(d,p)	HF	49.4	3.36	88.642	3.546	0.071
6-31G(2d,2p)	HF	51.5	3.30	84.998	3.606	0.077
6-311G	HF	31.4	3.36	169.512	3.492	0.036
6-311G(d,p)	HF	38.69	3.40	132.079	3.445	0.045
6-311G(2d,2p)	HF	49.2	3.35	91.134	3.561	0.070
6-31G	MP2	17.9	3.48	517.189	3.252	0.01
6-31G(d,p)	MP2	41.4	2.15	113.581	3.448	0.052
6-31G(2d,2p)	MP2	50.7	3.22	83.92	3.833	0.088
6-311G	MP2	17.1	3.46	568.486	3.293	0.010
6-311G(d,p)	MP2	37.9	3.39	132.377	3.450	0.045
6-311G(2d,2p)	MP2	48.7	3.28	89.528	3.705	0.077

Table 5.12: Optimised structures for the complex NO-HF, in the A' ground state, using different basis sets and methods. The angle is that between the NO axis and the a-axis of the complex and the length is the distance between the centre of masses of the monomers.

operating system and Gaussian 94.[32] A series of calculations were carried out in an attempt to predict the ground state structure of the complex. Basis sets from the 6-31G/6-311G series were used with differing numbers of polarization functions at either Hartree-Fock or Møller-Plesset level 2 with the results being presented in Table 5.11. The table shows a wide variation in the structure of the complex with the number of polarization wavefunctions included. It is the case that a large contribution to the energy of interaction of van der Waals complexes comes from polarization. The evaluation of a correct structure would therefore require the presence of the extra polarisation wavefunctions. The difference between the two methods of calculation is

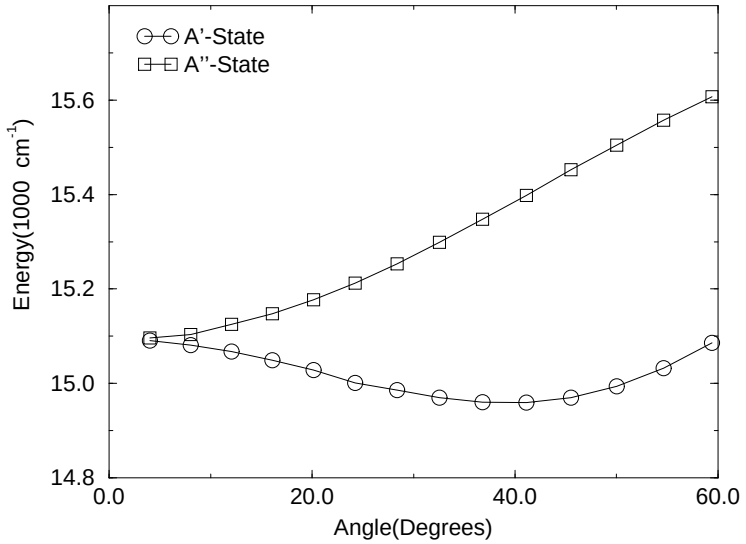

Figure 5.15: Calculated potential energy of the A' and A'' states for the van der Waals complex NO-HF at angles between 0 and 60° using a 6-311G(d,p) basis set, at Hartree-Fock level optimising the oxygen-hydrogen distance.

less clear and for the basis sets with the largest number of polarization functions the difference is not significant. The angle of the optimised geometry increases rapidly with the number of polarisation wavefunctions. The results show that the complex is substantially bent and correctly predicts the ground state of the complex to be the A' state. The rotational constants are close to those observed in the complex shown in Table 5.7 with $\frac{1}{2}(B + C)$ being very similar to the experimental value of 3.365GHz. The results above do not indicate the position of the hydrogen atom in the complex which does vary substantially dependent on the basis and does not necessarily lie on the line connecting oxygen and fluorine. The small mass of hydrogen means that large variations in its postion does not affect the values of the rotational constants greatly.

The results agree with those of Davis et al[5] who carried out ab-initio calculations as part of their study of NO-HF and with a 6-31G basis set found that the optimum geometry of 30°

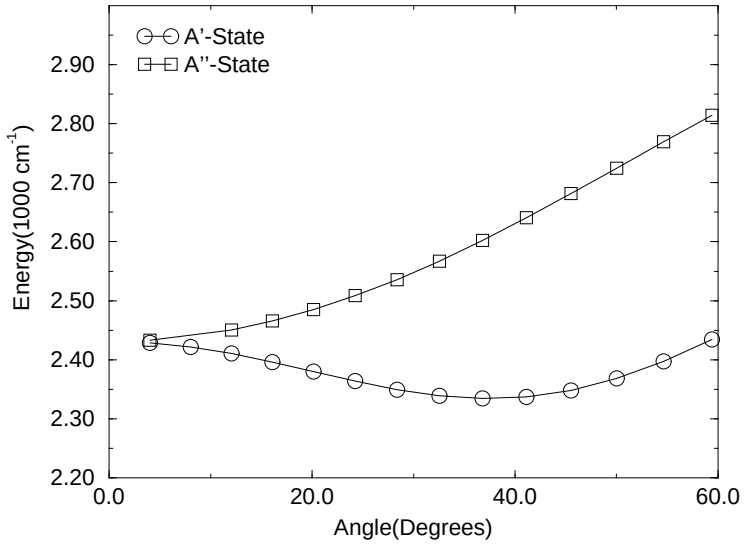

Figure 5.16: Calculated potential energy of the A' and A'' states for the van der Waals complex NO-HF at angles between 0 and 60° using a 6-311G(d,p) basis set, at Møeller-Plesset level 2 optimising the oxygen-hydrogen distance

between the NO and HF axes which correlates with the value of ∼27° between the NO axis and the complex a-axis in our calculations. A series of calculations were also carried out where the angle between the NO and HF monomer axis was varied between 5 and 60° with the everything fixed except the oxygen hydrogen bond length. The calculation was then rerun with an electron shifted into the A'', out of plane orbital so that the change in energy of the configurations with the unpaired electron in plane and out of plane could be plotted. These calculations used a 6-311G(d,p) basis set and are plotted in Figures 5.15 and 5.16. The angle plotted is the usual NO axis complex a-axis angle converted from the output Cartesian coordinates. The difference in the energy of the two electronic configurations at about 40° is ∼400cm^{-1} for the Hartree-Fock method and ∼300cm^{-1} for the Møeller-Plesset method. The experimental value of the Renner-Teller parameter is about -300cm^{-1} which shows very good agreement.

The calculations show that the structure of the complex is determined by the location of the

unpaired electron. If the ground state were the out of plane orbital then the complex would be linear. The reduction in the energy of the in plane orbital shows that the interaction with this orbital is dominated by attractive forces. Comparing this to Ar-NO where the Renner-Teller parameter is positive show a repulsive interaction dominating.

5.12 Conclusion

The microwave spectrum of the van der Waals complex NO-HF has been measured. The spectra with their rich hyperfine structure from the coupling of the nuclei of nitrogen, hydrogen and fluorine have been assigned and fitted. The parameters obtained from the fits show that the structure is not completely determined because of correlation between the angle and other parameters. The structure will not be certain until other fine structure states have been measured.

The hyperfine constants show that there is a dipolar interaction between the magnetic moment due to the unpaired electron on the NO and the hydrogen and fluorine nuclei. There are also Fermi-contact contributions to the hyperfine indicating that there has been electron transfer to the hydrogen.

References

[1] C. M. Western, P. R. R. Landridge-Smith, B. J. Howard, S. E. Novick. *Mol. Phys.*, **44**, 145, (1981).

[2] S. E. Novick, P. B. Davies, T. R. Dyke, W. Klemperer. *J. Am. Chem. Soc.*, **95**, 8547, (1973).

[3] P. D. A. Mills, C. M. Western, B. J. Howard. *J. Phys. Chem.*, **90**, 2991, (1986).

[4] M. Iida, Y. Ohsima. Y. Endo. *J. Chem. Phys.*, **94**, 6989, (1991).

[5] S. R. Davis, L. Andrews, C. O. Trindle. *J. Chem. Phys.*, **86**, 6027, (1987).

[6] W. M. Fawzy, G. T. Frazer, J. T. Hougen. *J. Chem. Phys*, **93**, 2992, (1990).

[7] K. J. Rensberger, J. T. Blair, F. Weinhold, F. F. Crim. *J. Chem. Phys.*, **91**, 1688, (1989).

[8] E. J. Campbell, M. R. Keenan, L. W. Buxton, T. J. Balle, P. D. Soper, A. C. Legon, W. H. Flygare. *Chem. Phys. Lett.*, **70**, 420, (1980).

[9] M. R. Keenan, L. W. Buxton, E. J. Campbell, T. J. Balle, W. H. Flygare. *J. Chem. Phys.*, **73**, 3523, (1980).

[10] P. W. Atkins. *Molecular Quantum Mechanics*. Oxford University Press, Oxford, (1986).

[11] W. H. Press, S. A. Teukolsky, W. T. Vetterling, B. P. Flannery. *Numerical Recipies in C*. Cambridge University Press, Cambridge, (1992).

[12] M. Mizushima. *The Theory of Rotating Diatomic Molecules*. Wiley-Interscience, New York, (1975).

[13] W. L. Meerts, A. Dymanus. *J. Mol. Spec.*, **44**, 320, (1972).

[14] A. C. Legon, D. J. Millen. *Faraday Disc. Chem. Soc.*, **73**, 71, (1982).

[15] P. D. A. Mills, C. M. Western, B. J. Howard. *J. Phys. Chem.*, **90**, 4961, (1986).

[16] P. D. Soper, A. C. Legon, W. G. Read, W. H. Flygare. *J. Chem. Phys.*, **76**, 292, (1982).

[17] A. Carrington, A. D. McLachlan. *Introduction to Magnetic Resonance with applications to chemistry chemical physics*. Harper and Row, New York, (1967).

[18] F. A. Baiocchi, T. A. Dixon, C. H. Joyner, W. H. Flygare. *J. Chem. Phys.*, **75**, 2041, (1981).

[19] R. Sternheimer. *Phys. Rev.*, **80**, 102, (1950).

[20] R. M. Sternheimer, H. M. Foley. *Phys. Rev.*, **92**, 1460, (1953).

[21] R. M. Sternheimer. *Phys. Rev.*, **95**, 736, (1954).

[22] R. M. Sternheimer. *Phys. Rev.*, **105**, 158, (1956).

[23] S. Engström, H. Wennerström, B. Jönsson, G. Karlström. *Mol. Phys.*, **34**, 813, (1977).

[24] A.J. Stone, A. D. Buckingham, P. W. Fowler. *J. Chem. Phys.*, **107**, 1030, (1997).

[25] A. J. Stone. *Chem. Phys. Lett.*, **83**, 233, (1981).

[26] Price, A. J. Stone. *Chem. Phys. Lett.*, **98**, 419, (1983).

[27] A. D. Buckingham, P. W. Fowler. *J. Chem. Phys.*, **79**, 6426, (1983).

[28] A. J. Stone, Alderton. *Mol. Phys.*, **56**, 1047, (1985).

[29] K. Morokuma. *J. Chem. Phys.*, **55**, 1236, (1971).

[30] A. J. Stone. *The Theory Intermolecular Forces*. Oxford University Press, Oxford, (1996).

[31] H. Umeyama, K. Morokuma. *J. A. Chem. Soc.*, **99**, 1316, (1977).

[32] M. J. Frisch, G. W. Trucks, H. B. Schlegel, P. M. W. Gill, B. G. Johnson, M. A. Robb, J. R. Cheeseman, T. Keith, G. A. Petersson, J. A. Montgomery, K. Raghavachari, M. A. Al-Laham, V. G. Zakrzewski, J. V. Ortiz, J. B. Foresman, J. Cioslowski, B. B. Stefanov, A. Nanayakkara, M. Challacombe, C. Y. Peng, P. Y. Ayala, W. Chen, M. W. Wong, J. L. Andres, E. S. Replogle, R. Gomperts, R. L. Martin, D. J. Fox, J. S. Binkley, D. J. Defrees, J. Baker, J. P. Stewart, M. Head-Gordon, C. Gonzalez, J. A. Pople. *Gaussian 94 Revision D.4*. Gaussian Inc., Pittsburgh PA, (1995).

Appendix A

Fine Structure Matrix Elements

A.1 Rotational and Spin-Orbit Hamiltonian

A.1.1 Diagonal in Electronic State

$$\langle JK_a\Lambda\Sigma|H|JK_a'\Lambda'\Sigma'\rangle = \delta_{K_a,K_a'}\delta_{\Lambda,\Lambda'}\delta_{\Sigma,\Sigma'}\begin{bmatrix}\{A-\frac{1}{2}(B+C)K_a'^2\\ +\frac{1}{2}(B+C)J(J+1)\\ -2A\cos(\theta)K_a'(\Lambda'+\Sigma')\\ +(2A\cos^2(\theta)+2B\sin^2(\theta)+\zeta)\Lambda'\Sigma'\end{bmatrix}$$

$$\langle JK_a\pm1\Lambda\Sigma|H|JK_a'\Lambda'\Sigma'\rangle = -B\sin(\theta)(\Lambda'+\Sigma')\{(J\mp K_a')(J\pm K_a'+1)\}^{\frac{1}{2}}$$

$$\langle JK_a\pm2\Lambda\Sigma|H|JK_a'\Lambda'\Sigma'\rangle =$$
$$\frac{1}{4}(B-C)\{(J\mp K_a')(J\pm K_a'+1)(J\mp K_a')(J\pm K_a'+1)\}^{\frac{1}{2}}$$

$$\langle JK_a\Lambda\Sigma\pm1|H|JK_a'\Lambda'\Sigma'\rangle =$$
$$\{AK_a'\sin(\theta)+(B-A)\sin(\theta)\cos(\theta)\Lambda\}\{(S\mp\Sigma')(S\pm\Sigma'+1)\}^{\frac{1}{2}}$$

$$\langle JK_a\pm1\Lambda\Sigma\pm1|H|JK_a'\Lambda'\Sigma'\rangle =$$
$$-\frac{1}{2}(B\cos(\theta)+C)\{(J\mp K_a')(J\pm K_a'+1)(S\mp\Sigma')(S\pm\Sigma'+1)\}^{\frac{1}{2}}$$

$$\langle JK_a\pm1\Lambda\Sigma\mp1|H|JK_a'\Lambda'\Sigma'\rangle =$$
$$-\frac{1}{2}(B\cos(\theta)-C)\{(J\mp K_a')(J\pm K_a'+1)(S\pm\Sigma')(S\mp\Sigma'+1)\}^{\frac{1}{2}}$$

$$\langle JK_a\Lambda=\mp1\Sigma|H|JK_a'\Lambda'=\pm1\Sigma'\rangle =$$
$$\frac{1}{4}(A\sin^2(\theta)+B\cos^2(\theta)-C)\{L(L+1)-(\Lambda'\mp1)(\Lambda'\mp2)\}^{\frac{1}{2}}\{L(L+1)-\Lambda'(\Lambda'\mp1)\}^{\frac{1}{2}}$$

$$\langle JK_a\Lambda=\pm1\Sigma|H|JK_a'\Lambda'=\mp1\Sigma'\rangle = -\frac{1}{2}\epsilon_2$$

A.1.2 Off-Diagonal in Electronic State

$$\langle JK_a\Lambda = 1\Sigma|H|JK'_a\Lambda = 0\Sigma'\rangle =$$
$$(\langle B+\rangle - \langle A+\rangle)\sin(\theta)\cos(\theta)(\Sigma' + \frac{1}{2}) + \langle A+\rangle K_a \sin(\theta)$$
$$\langle JK_a\Lambda = -1\Sigma|H|JK'_a\Lambda = 0\Sigma'\rangle =$$
$$(-1)^S(\langle B+\rangle - \langle A+\rangle)\sin(\theta)\cos(\theta)(\Sigma' - \frac{1}{2}) + (-1)^S\langle A+\rangle K_a \sin(\theta)$$
$$\langle JK_a \pm 1\Lambda = 1\Sigma|H|JK'_a\Lambda = 0\Sigma'\rangle =$$
$$\frac{1}{2}\{(J \mp K'_a)(J \pm K'_a + 1)\}^{\frac{1}{2}}(-\langle B+\rangle\cos(\theta) \mp \langle C+\rangle)$$
$$\langle JK_a \pm 1\Lambda = -1\Sigma|H|JK'_a\Lambda = 0\Sigma'\rangle =$$
$$\frac{1}{2}\{(J \mp K'_a)(J \pm K'_a + 1)\}^{\frac{1}{2}}(-1)^S(-\langle B+\rangle\cos(\theta) \pm \langle C+\rangle)$$
$$\langle JK_a\Lambda = 1\Sigma \pm \frac{1}{2}|H|JK'_a\Lambda = 0\Sigma' \mp \frac{1}{2}\rangle =$$
$$\frac{1}{2}(\frac{1}{2}\langle\zeta+\rangle \mp \frac{1}{2}\langle\zeta+\rangle) + \frac{1}{2}(\langle A+\rangle\sin^2(\theta) + \langle B+\rangle\cos^2(\theta) \mp \langle C+\rangle)$$
$$\langle JK_a\Lambda = -1\Sigma \pm \frac{1}{2}|H|JK'_a\Lambda = 0\Sigma' \mp \frac{1}{2}\rangle =$$
$$\frac{1}{2}(-1)^S(\frac{1}{2}\langle\zeta+\rangle \pm \frac{1}{2}\langle\zeta+\rangle) + \frac{1}{2}(-1)^S(\langle A+\rangle\sin^2(\theta) + \langle B+\rangle\cos^2(\theta) \pm \langle C+\rangle)$$

Appendix B

Hyperfine Matrix Elements

B.1 Magnetic Hyperfine

$$\langle \eta\Lambda; S\Sigma; JK_a; I_N F_N | H_{mag} | \eta\Lambda'; S\Sigma'; J'K'_a; I'_N F'_N \rangle = (-1)^{J'+I_N+F_N} \left\{(2J'+1)(2J+1)\right\}^{\frac{1}{2}}$$
$$\left\{I_N(I_N+1)(2I_N+1)\right\}^{\frac{1}{2}} \begin{Bmatrix} F_N & I_N & J \\ I & J' & I_N \end{Bmatrix} \sum_r (-1)^{J-K_a} \begin{pmatrix} J & 1 & J' \\ -K_a & q & K'_a \end{pmatrix}$$
$$\left\{ \begin{array}{l} \delta_{\Lambda,\Lambda'}\delta_{\Sigma,\Sigma'} a\Lambda \begin{Bmatrix} \frac{1}{\sqrt{2}}\sin\theta\,\delta_{q,-1} \\ +\cos\theta\,\delta_{q,0} \\ -\frac{1}{\sqrt{2}}\sin\theta\,\delta_{q,1} \end{Bmatrix} \\ \delta_{\Lambda,\Lambda'} b_F \left\{S(S+1)(2S+1)\right\}^{\frac{1}{2}} (-1)^{S-\Sigma} \left[\begin{array}{l} \begin{Bmatrix} \cos^2\frac{\theta}{2} \begin{pmatrix} S & 1 & S \\ -\Sigma & -1 & \Sigma' \end{pmatrix} \\ \frac{1}{\sqrt{2}}\sin\theta \begin{pmatrix} S & 1 & S \\ -\Sigma & 0 & \Sigma' \end{pmatrix} \\ \sin^2\frac{\theta}{2} \begin{pmatrix} S & 1 & S \\ -\Sigma & 1 & \Sigma' \end{pmatrix} \end{Bmatrix} \delta_{q,-1} \\ \begin{Bmatrix} -\frac{1}{\sqrt{2}}\sin\theta \begin{pmatrix} S & 1 & S \\ -\Sigma & -1 & \Sigma' \end{pmatrix} \\ \cos\theta \begin{pmatrix} S & 1 & S \\ -\Sigma & 0 & \Sigma' \end{pmatrix} \\ \frac{1}{\sqrt{2}}\sin\theta \begin{pmatrix} S & 1 & S \\ -\Sigma & 1 & \Sigma' \end{pmatrix} \end{Bmatrix} \delta_{q,0} \\ \begin{Bmatrix} \sin^2\frac{\theta}{2} \begin{pmatrix} S & 1 & S \\ -\Sigma & -1 & \Sigma' \end{pmatrix} \\ -\frac{1}{\sqrt{2}}\sin\theta \begin{pmatrix} S & 1 & S \\ -\Sigma & 0 & \Sigma' \end{pmatrix} \\ \cos^2\frac{\theta}{2} \begin{pmatrix} S & 1 & S \\ -\Sigma & 1 & \Sigma' \end{pmatrix} \end{Bmatrix} \delta_{q,1} \end{array} \right] \end{array} \right\}$$

$$
\left\{
\begin{array}{l}
\delta_{\Lambda,\Lambda'}\frac{c}{3}\big\{S(S+1)(2S+1)\big\}^{\frac{1}{2}}(-1)^{S-\Sigma}
\left[
\begin{array}{l}
\left\{
\begin{array}{c}
-\cos^2\frac{\theta}{2}\begin{pmatrix} S & 1 & S \\ -\Sigma & -1 & \Sigma' \end{pmatrix} \\
\sqrt{2}\sin\theta\begin{pmatrix} S & 1 & S \\ -\Sigma & 0 & \Sigma' \end{pmatrix} \\
-\sin^2\frac{\theta}{2}\begin{pmatrix} S & 1 & S \\ -\Sigma & 1 & \Sigma' \end{pmatrix}
\end{array}
\right\}\delta_{q,-1} \\
\left\{
\begin{array}{c}
\frac{1}{\sqrt{2}}\sin\theta\begin{pmatrix} S & 1 & S \\ -\Sigma & -1 & \Sigma' \end{pmatrix} \\
2\cos\theta\begin{pmatrix} S & 1 & S \\ -\Sigma & 0 & \Sigma' \end{pmatrix} \\
-\frac{1}{\sqrt{2}}\sin\theta\begin{pmatrix} S & 1 & S \\ -\Sigma & 1 & \Sigma' \end{pmatrix}
\end{array}
\right\}\delta_{q,0} \\
\left\{
\begin{array}{c}
-\sin^2\frac{\theta}{2}\begin{pmatrix} S & 1 & S \\ -\Sigma & -1 & \Sigma' \end{pmatrix} \\
-\sqrt{2}\sin\theta\begin{pmatrix} S & 1 & S \\ -\Sigma & 0 & \Sigma' \end{pmatrix} \\
-\cos^2\frac{\theta}{2}\begin{pmatrix} S & 1 & S \\ -\Sigma & 1 & \Sigma' \end{pmatrix}
\end{array}
\right\}\delta_{q,1}
\end{array}
\right] \\
\delta_{\Lambda,\Lambda'+2}d\big\{S(S+1)(2S+1)\big\}^{\frac{1}{2}}(-1)^{S-\Sigma}
\left\{
\begin{array}{c}
\sin^2\frac{\theta}{2}\begin{pmatrix} S & 1 & S \\ -\Sigma & -1 & \Sigma' \end{pmatrix}\delta_{q,-1} \\
+\frac{1}{\sqrt{2}}\sin\theta\begin{pmatrix} S & 1 & S \\ -\Sigma & -1 & \Sigma' \end{pmatrix}\delta_{q,0} \\
\cos^2\frac{\theta}{2}\begin{pmatrix} S & 1 & S \\ -\Sigma & -1 & \Sigma' \end{pmatrix}\delta_{q,1}
\end{array}
\right\} \\
\delta_{\Lambda,\Lambda'-2}d\big\{S(S+1)(2S+1)\big\}^{\frac{1}{2}}(-1)^{S-\Sigma}
\left\{
\begin{array}{c}
\cos^2\frac{\theta}{2}\begin{pmatrix} S & 1 & S \\ -\Sigma & 1 & \Sigma' \end{pmatrix}\delta_{q,-1} \\
-\frac{1}{\sqrt{2}}\sin\theta\begin{pmatrix} S & 1 & S \\ -\Sigma & 1 & \Sigma' \end{pmatrix}\delta_{q,0} \\
\sin^2\frac{\theta}{2}\begin{pmatrix} S & 1 & S \\ -\Sigma & 1 & \Sigma' \end{pmatrix}\delta_{q,1}
\end{array}
\right\}
\end{array}
\right\}
$$

B.2 Electric Quadrupole

$$
\begin{aligned}
&\langle \eta\Lambda; s\Sigma; J, K_a; I_N, F_N, M_{F_N} | H_{quad} | \eta\Lambda'; s\Sigma'; J', K'_a; I_N, F'_N, M_{F'_N} \rangle \\
&= \delta_{F_N,F'_N} \delta_{M_{F_N},M'_{F_N}} \delta_{\Sigma,\Sigma'} (-1)^{J'+I_N+F_N} \begin{Bmatrix} J & I_N & F_N \\ I_N & J' & 2 \end{Bmatrix} \\
&\quad \frac{1}{2} \left[\frac{(2I_N+3)(2I_N+2)(2I_N+1)}{2I_N(2I_N-1)} \right]^{\frac{1}{2}} \left[(2J+1)(2J'+1) \right]^{\frac{1}{2}} \\
&\quad \sum_q (-1)^{J-K_a} \begin{pmatrix} J & 2 & J' \\ -K_a & q & K'_a \end{pmatrix} \left\{ \begin{array}{c}
\delta_{q,-2} \begin{pmatrix} \delta_{\Lambda,\Lambda'} \sqrt{\frac{3}{8}} \sin^2(\theta) \frac{1}{2} eQq_0 \\ \delta_{\Lambda,\Lambda'+2} \sin^4(\frac{\theta}{2}) \frac{1}{2\sqrt{6}} eQq_2 \\ \delta_{\Lambda,\Lambda'-2} \cos^4(\frac{\theta}{2}) \frac{1}{2\sqrt{6}} eQq_2 \end{pmatrix} \\
\delta_{q,-1} \begin{pmatrix} \delta_{\Lambda,\Lambda'} \sqrt{\frac{3}{2}} \sin(\theta)\cos(\theta) \frac{1}{2} eQq_0 \\ -\delta_{\Lambda,\Lambda'+2} \frac{1}{2} \sin(\theta)(\cos(\theta)-1) \frac{1}{2\sqrt{6}} eQq_2 \\ -\delta_{\Lambda,\Lambda'-2} \frac{1}{2} \sin(\theta)(\cos(\theta)+1) \frac{1}{2\sqrt{6}} eQq_2 \end{pmatrix} \\
\delta_{q,0} \begin{pmatrix} \delta_{\Lambda,\Lambda'} \frac{1}{2} (3\cos^2(\theta)-1) \frac{1}{2} eQq_0 \\ \delta_{\Lambda,\Lambda'+2} \sqrt{\frac{3}{8}} \sin^2(\theta) \frac{1}{2\sqrt{6}} eQq_2 \\ \delta_{\Lambda,\Lambda'-2} \sqrt{\frac{3}{8}} \sin^2(\theta) \frac{1}{2\sqrt{6}} eQq_2 \end{pmatrix} \\
\delta_{q,1} \begin{pmatrix} -\delta_{\Lambda,\Lambda'} \sqrt{\frac{3}{2}} \sin(\theta)\cos(\theta) \frac{1}{2} eQq_0 \\ \delta_{\Lambda,\Lambda'+2} \frac{1}{2} \sin(\theta)(\cos(\theta)+1) \frac{1}{2\sqrt{6}} eQq_2 \\ \delta_{\Lambda,\Lambda'-2} \frac{1}{2} \sin(\theta)(\cos(\theta)-1) \frac{1}{2\sqrt{6}} eQq_2 \end{pmatrix} \\
\delta_{q,2} \begin{pmatrix} \delta_{\Lambda,\Lambda'} \sqrt{\frac{3}{8}} \sin^2(\theta) \frac{1}{2} eQq_0 \\ \delta_{\Lambda,\Lambda'+2} \cos^4(\frac{\theta}{2}) \frac{1}{2\sqrt{6}} eQq_2 \\ \delta_{\Lambda,\Lambda'-2} \sin^4(\frac{\theta}{2}) \frac{1}{2\sqrt{6}} eQq_2 \end{pmatrix}
\end{array} \right\}
\end{aligned}
$$

B.3 Matrix Elements for Hydrogen and Fluorine

B.3.1 $q_2 = 0$, $\delta_{\Lambda,\Lambda'}$

$$
\begin{aligned}
&\langle \eta\Lambda; S\Sigma; JK_a; I_N F_N; I_H F_H | H_{hf,H} | \eta\Lambda'; S\Sigma'; J'K'_a; I_N F'_N; I_H F'_H \rangle \\
&\quad = \delta_{F_H,F'_H} (-1)^{2F'_N+I_N+I_H+F_H+J+1} \begin{Bmatrix} F_N & I_H & F_H \\ I_H & F'_N & 1 \end{Bmatrix} \begin{Bmatrix} J & F_N & I_N \\ F'_N & J' & 1 \end{Bmatrix} \\
&\qquad [I_H(I_H+1)(2I_H+1)]^{\frac{1}{2}} [(2F'_N+1)(2F_N+1)]^{\frac{1}{2}} \\
&\qquad \sum_q (-1)^{J-K_a} [(2J'+1)(2J+1)]^{\frac{1}{2}} \begin{pmatrix} J & 1 & J' \\ -K_a & q & K'_a \end{pmatrix} \delta_{\Lambda,\Lambda'} A < \eta\Lambda | C_0^2(\theta_i,\phi_i) | \eta'\Lambda' > \\
&\qquad \left[\begin{array}{l}
\delta_{q,0} \left\{ \begin{array}{c} 2\delta_{\Sigma,\Sigma'}\Lambda' \cos\theta \\ +g_e(-1)^{S-\Sigma}\sqrt{S(S+1)(2S+1)} \begin{pmatrix} 2\cos\theta \begin{pmatrix} S & 1 & S \\ -\Sigma & 0 & \Sigma' \end{pmatrix} \\ \sqrt{2}\sin\theta \begin{pmatrix} S & 1 & S \\ -\Sigma & 1 & \Sigma' \end{pmatrix} \\ -\sqrt{2}\sin\theta \begin{pmatrix} S & 1 & S \\ -\Sigma & -1 & \Sigma' \end{pmatrix} \end{pmatrix} \end{array} \right\} \\
\delta_{q,1} \left\{ \begin{array}{c} +\frac{1}{\sqrt{2}}\delta_{\Sigma,\Sigma'}\Lambda' \sin\theta \\ +g_e(-1)^{S-\Sigma}\sqrt{S(S+1)(2S+1)} \begin{pmatrix} +\frac{1}{\sqrt{2}}\sin\theta \begin{pmatrix} S & 1 & S \\ -\Sigma & 0 & \Sigma' \end{pmatrix} \\ -\cos^2\frac{\theta}{2} \begin{pmatrix} S & 1 & S \\ -\Sigma & 1 & \Sigma' \end{pmatrix} \\ -\sin^2\frac{\theta}{2} \begin{pmatrix} S & 1 & S \\ -\Sigma & -1 & \Sigma' \end{pmatrix} \end{pmatrix} \end{array} \right\} \\
\delta_{q,-1} \left\{ \begin{array}{c} -\frac{1}{\sqrt{2}}\delta_{\Sigma,\Sigma'}\Lambda' \sin\theta \\ -g_e(-1)^{S-\Sigma}\sqrt{S(S+1)(2S+1)} \begin{pmatrix} +\frac{1}{\sqrt{2}}\sin\theta \begin{pmatrix} S & 1 & S \\ -\Sigma & 0 & \Sigma' \end{pmatrix} \\ -\sin^2\frac{\theta}{2} \begin{pmatrix} S & 1 & S \\ -\Sigma & 1 & \Sigma' \end{pmatrix} \\ -\cos^2\frac{\theta}{2} \begin{pmatrix} S & 1 & S \\ -\Sigma & -1 & \Sigma' \end{pmatrix} \end{pmatrix} \end{array} \right\}
\end{array} \right]
\end{aligned}
$$

B.3.2 $q_2 = 0$, $\delta_{\Lambda,\Lambda'\pm 2}$

$$
\begin{aligned}
&\langle \eta\Lambda; S\Sigma; JK_a; I_N F_N; I_H F_H | H_{hf,H} | \eta\Lambda'; S\Sigma'; J'K'_a; I_N F'_N; I_H F'_H \rangle \\
&\quad = \delta_{F_H,F'_H} (-1)^{2F'_N + I_N + I_H + F_H + J + 1} \begin{Bmatrix} F_N & I_H & F_H \\ I_H & F'_N & 1 \end{Bmatrix} \begin{Bmatrix} J & F_N & I_N \\ F'_N & J' & 1 \end{Bmatrix} \\
&\qquad [I_H(I_H+1)(2I_H+1)]^{\frac{1}{2}} [(2F'_N+1)(2F_N+1)]^{\frac{1}{2}} \\
&\qquad \sum_q (-1)^{J-K_a} [(2J'+1)(2J+1)]^{\frac{1}{2}} \begin{pmatrix} J & 1 & J' \\ -K_a & q & K'_a \end{pmatrix} \delta_{\Lambda,\Lambda''\pm 2} A' < \eta\Lambda | C_0^2(\theta_i,\phi_i) | \eta'\Lambda'' > \\
&\qquad \left[\begin{array}{l}
\delta_{q,0} \left\{ g_e (-1)^{S-\Sigma} \sqrt{S(S+1)(2S+1)} \begin{pmatrix} 2\cos\theta \begin{pmatrix} S & 1 & S \\ -\Sigma & 0 & \Sigma' \end{pmatrix} \\ \sqrt{2}\sin\theta \begin{pmatrix} S & 1 & S \\ -\Sigma & 1 & \Sigma' \end{pmatrix} \\ -\sqrt{2}\sin\theta \begin{pmatrix} S & 1 & S \\ -\Sigma & -1 & \Sigma' \end{pmatrix} \end{pmatrix} \right\} \\
\delta_{q,1} \left\{ g_e (-1)^{S-\Sigma} \sqrt{S(S+1)(2S+1)} \begin{pmatrix} +\frac{1}{\sqrt{2}}\sin\theta \begin{pmatrix} S & 1 & S \\ -\Sigma & 0 & \Sigma' \end{pmatrix} \\ -\cos^2\frac{\theta}{2} \begin{pmatrix} S & 1 & S \\ -\Sigma & 1 & \Sigma' \end{pmatrix} \\ -\sin^2\frac{\theta}{2} \begin{pmatrix} S & 1 & S \\ -\Sigma & -1 & \Sigma' \end{pmatrix} \end{pmatrix} \right\} \\
\delta_{q,-1} \left\{ g_e (-1)^{S-\Sigma} \sqrt{S(S+1)(2S+1)} \begin{pmatrix} -\frac{1}{\sqrt{2}}\sin\theta \begin{pmatrix} S & 1 & S \\ -\Sigma & 0 & \Sigma' \end{pmatrix} \\ -\sin^2\frac{\theta}{2} \begin{pmatrix} S & 1 & S \\ -\Sigma & 1 & \Sigma' \end{pmatrix} \\ -\cos^2\frac{\theta}{2} \begin{pmatrix} S & 1 & S \\ -\Sigma & -1 & \Sigma' \end{pmatrix} \end{pmatrix} \right\}
\end{array} \right]
\end{aligned}
$$

B.3.3 Perpendicular

For $q_2 = \pm 1$

$$
\begin{aligned}
&\langle \eta\Lambda; S\Sigma; JK_a; I_N F_N; I_H F_H | H_{hf,H} | \eta\Lambda'; S\Sigma'; J'K'_a; I_N F'_N; I_H F'_H \rangle \\
&\quad = \delta_{F_H,F'_H} (-1)^{2F'_N + I_N + I_H + F_H + J + 1} \begin{Bmatrix} F_N & I_H & F_H \\ I_H & F'_N & 1 \end{Bmatrix} \begin{Bmatrix} J & F_N & I_N \\ F'_N & J' & 1 \end{Bmatrix} \\
&\qquad [I_H(I_H+1)(2I_H+1)]^{\frac{1}{2}} [(2F'_N+1)(2F_N+1)]^{\frac{1}{2}} \\
&\qquad \sum_q (-1)^{J-K_a} [(2J'+1)(2J+1)]^{\frac{1}{2}} \begin{pmatrix} J & 1 & J' \\ -K_a & q & K'_a \end{pmatrix} (-1)\sqrt{3} A \delta_{\Lambda,\Lambda'} \langle \eta\Lambda | C^2_{\pm 1}(\theta,\phi) | \eta\Lambda' \rangle \\
&\qquad \begin{pmatrix} -\delta_{q,0} g_e (-1)^{S-\Sigma} [S(S+1)(2S+1)]^{\frac{1}{2}} \begin{bmatrix} \begin{pmatrix} S & 1 & S \\ -\Sigma & 1 & \Sigma' \end{pmatrix} \\ \begin{pmatrix} S & 1 & S \\ -\Sigma & -1 & \Sigma' \end{pmatrix} \end{bmatrix} \\ \delta_{q,-1} \begin{bmatrix} -\cos\theta \Lambda' \delta_{\Sigma,\Sigma'} \\ (-1)^{S-\Sigma} g_e [S(S+1(2S+1)]^{\frac{1}{2}} \begin{pmatrix} -\cos\theta \begin{pmatrix} S & 1 & S \\ -\Sigma & 0 & \Sigma' \end{pmatrix} \\ -\frac{1}{\sqrt{2}} \sin\theta \begin{pmatrix} S & 1 & S \\ -\Sigma & 1 & \Sigma' \end{pmatrix} \\ +\frac{1}{\sqrt{2}} \sin\theta \begin{pmatrix} S & 1 & S \\ -\Sigma & -1 & \Sigma' \end{pmatrix} \end{pmatrix} \end{bmatrix} \\ \delta_{q,1} \begin{bmatrix} -\cos\theta \Lambda' \delta_{\Sigma,\Sigma'} \\ (-1)^{S-\Sigma} g_e [S(S+1(2S+1)]^{\frac{1}{2}} \begin{pmatrix} -\cos\theta \begin{pmatrix} S & 1 & S \\ -\Sigma & 0 & \Sigma' \end{pmatrix} \\ -\frac{1}{\sqrt{2}} \sin\theta \begin{pmatrix} S & 1 & S \\ -\Sigma & 1 & \Sigma' \end{pmatrix} \\ +\frac{1}{\sqrt{2}} \sin\theta \begin{pmatrix} S & 1 & S \\ -\Sigma & -1 & \Sigma' \end{pmatrix} \end{pmatrix} \end{bmatrix} \end{pmatrix}
\end{aligned}
$$

B.3.4 $q_2 = \pm 2$

$$
\begin{aligned}
&\langle \eta\Lambda; S\Sigma; JK_a; I_1F_1; I_2F_2 | H_{hf,H} | \eta\Lambda'; S\Sigma'; J'K'_a; I'_1F'_1; I'_2F'_2 \rangle \\
&\quad = \delta_{F_2,F'_2} (-1)^{2F'_1+I_1+I_2+F_2+J+1} \begin{Bmatrix} F_1 & I_2 & F_2 \\ I_2 & F'_1 & 1 \end{Bmatrix} \begin{Bmatrix} J & F_1 & I_1 \\ F'_1 & J' & 1 \end{Bmatrix} \\
&\qquad [I_2(I_2+1)(2I_2+1)]^{\frac{1}{2}} [(2F'_1+1)(2F_1+1)]^{\frac{1}{2}} \\
&\qquad \sum_q (-1)^{J-K_a} [(2J'+1)(2J+1)]^{\frac{1}{2}} \begin{pmatrix} J & 1 & J' \\ -K_a & q & K'_a \end{pmatrix} (-1)\sqrt{3} A \langle \nu | C^2_{\pm 2}(\theta,\phi) | \nu \rangle \\
&\qquad \begin{pmatrix} \delta_{q,-1} \begin{bmatrix} -\frac{1}{\sqrt{2}} \sin\theta \Lambda' \delta_{\Sigma,\Sigma'} \\ (-)^{S-\Sigma} g_e [S(S+1(2S+1)]^{\frac{1}{2}} \begin{pmatrix} -\frac{1}{\sqrt{2}} \sin\theta \begin{pmatrix} S & 1 & S \\ -\Sigma & 0 & \Sigma' \end{pmatrix} \\ \cos^2\frac{\theta}{2} \begin{pmatrix} S & 1 & S \\ -\Sigma & 1 & \Sigma' \end{pmatrix} \\ \sin^2\frac{\theta}{2} \begin{pmatrix} S & 1 & S \\ -\Sigma & -1 & \Sigma' \end{pmatrix} \end{pmatrix} \end{bmatrix} \\ \delta_{q,1} \begin{bmatrix} \frac{1}{\sqrt{2}} \sin\theta \Lambda' \delta_{\Sigma,\Sigma'} \\ (-)^{S-\Sigma} g_e [S(S+1(2S+1)]^{\frac{1}{2}} \begin{pmatrix} \frac{1}{\sqrt{2}} \sin\theta \begin{pmatrix} S & 1 & S \\ -\Sigma & 0 & \Sigma' \end{pmatrix} \\ \sin^2\frac{\theta}{2} \begin{pmatrix} S & 1 & S \\ -\Sigma & 1 & \Sigma' \end{pmatrix} \\ \cos^2\frac{\theta}{2} \begin{pmatrix} S & 1 & S \\ -\Sigma & -1 & \Sigma' \end{pmatrix} \end{pmatrix} \end{bmatrix} \end{pmatrix}
\end{aligned}
$$

Appendix C

Standard Angular Momentum Transformations

These are transformations which are used in the derivation of the matrix elements of the hyperfine interaction.

C.0.5 Dot Product

T^k and U^k are tensor operators which act on j_1 and j_2 respectively.

$$\begin{aligned}&\langle \nu \& j_1 j_2 j m | T^k . U^k | \nu j_1' j_2' j' m' \rangle \\ &\quad = \delta_{j,j'} \delta_{m,m'} (-1)^{j_1'+j_2+j} \begin{Bmatrix} j_1 & j_2 & j \\ j_2' & j_1' & k \end{Bmatrix} \sum_{\nu''} \langle \nu j_1 || T^k || \nu'' j_1' \rangle \langle \nu'' j_2 || U^k || \nu' j_2' \rangle\end{aligned} \tag{C.1}$$

$$\begin{aligned}&\langle \nu j_1 j_2 j || T^{k_1} || \nu' j_1' j_2' j' \rangle \\ &\quad = \delta_{j_2,j_2'} (-1)^{j_1+j_2+j'+k_1} \sqrt{(2j'+1)(2j+1)} \begin{Bmatrix} j_1 & j & j_2 \\ j' & j_1' & k_1 \end{Bmatrix} \langle \nu j_1 || T^{k_1} || \nu' j_1' \rangle\end{aligned} \tag{C.2}$$

$$\begin{aligned}&\langle \nu j_1 j_2 j || U^{k_2} || \nu' j_1' j_2' j' \rangle \\ &\quad = \delta_{j_1,j_1'} (-1)^{j_1+j_2'+j+k_2} \sqrt{(2j'+1)(2j+1)} \begin{Bmatrix} j_2 & j & j_1 \\ j' & j_2' & k_2 \end{Bmatrix} \langle \nu j_2 || U^{k_2} || \nu' j_2' \rangle\end{aligned} \tag{C.3}$$

C.1 Wigner-Eckart Theorem

$$\langle \alpha' j' m' | T_q^k | \alpha j m \rangle = (-1)^{j'-m'} \begin{pmatrix} j' & k & j \\ -m' & q & m \end{pmatrix} \langle \alpha' j' || T^k || \alpha j \rangle \tag{C.4}$$

Appendix D

The Microwave Spectrum of NO-HF

The assigned transtions of the microwave spectrum of the van der Waals complex NO-HF. Note that the quantum numbers for the F states uses as labels F_N and F_F because it is the nitrogen and fluorine nuclei respectively that cause those splittings.

D.1 f-states

J′	e/f′	F'_N	F'_F	F′	J″	e/f″	F''_N	F''_F	F″	Obs(MHz)	Best Fit(MHz)		N constant(MHz)	
											Calc	Obs-Calc	Calc	Obs-Calc
$\frac{3}{2}$	f	$\frac{3}{2}$	2	$\frac{5}{2}$	$\frac{1}{2}$	f	$\frac{1}{2}$	1	$\frac{3}{2}$	12 311.879	12 311.845	0.034	12 312.952	-1.073
$\frac{3}{2}$	f	$\frac{3}{2}$	2	$\frac{3}{2}$	$\frac{1}{2}$	f	$\frac{1}{2}$	1	$\frac{3}{2}$	12 311.298	12 311.288	0.010	12 311.751	-0.453
$\frac{3}{2}$	f	$\frac{3}{2}$	2	$\frac{3}{2}$	$\frac{1}{2}$	f	$\frac{1}{2}$	1	$\frac{1}{2}$	12 309 485.	12 309.496	-0.011	12 309.364	0.121
$\frac{3}{2}$	f	$\frac{3}{2}$	1	$\frac{3}{2}$	$\frac{1}{2}$	f	$\frac{1}{2}$	1	$\frac{3}{2}$	12 308.255	12 308.232	0.023	12 308.694	-0.439
$\frac{3}{2}$	f	$\frac{3}{2}$	1	$\frac{1}{2}$	$\frac{1}{2}$	f	$\frac{1}{2}$	1	$\frac{3}{2}$	12 307.561	12 307.569	0.008	12 307.209	0.352
$\frac{3}{2}$	f	$\frac{3}{2}$	2	$\frac{3}{2}$	$\frac{1}{2}$	f	$\frac{1}{2}$	0	$\frac{1}{2}$	12 307.082	12 307.089	0.007	12 306.408	0.674
$\frac{3}{2}$	f	$\frac{3}{2}$	1	$\frac{3}{2}$	$\frac{1}{2}$	f	$\frac{1}{2}$	0	$\frac{1}{2}$	12 306.440	12 306.430	0.01	12 306.306	0.134
$\frac{3}{2}$	f	$\frac{3}{2}$	1	$\frac{3}{2}$	$\frac{1}{2}$	f	$\frac{1}{2}$	0	$\frac{1}{2}$	12 304.037	12 304.033	0.004	12 303.351	0.686
$\frac{3}{2}$	f	$\frac{3}{2}$	1	$\frac{1}{2}$	$\frac{1}{2}$	f	$\frac{1}{2}$	0	$\frac{1}{2}$	12 303.346	12 303.370	0.024	12 301.866	1.480
$\frac{3}{2}$	f	$\frac{1}{2}$	1	$\frac{3}{2}$	$\frac{1}{2}$	f	$\frac{1}{2}$	1	$\frac{3}{2}$	12 296.867	12 296.839	0.028	12 296.724	0.143
$\frac{3}{2}$	f	$\frac{1}{2}$	1	$\frac{1}{2}$	$\frac{1}{2}$	f	$\frac{1}{2}$	1	$\frac{3}{2}$	12 296.440	12 296.430	0.010	12 295.929	0.511

J′	e/f′	F'_N	F'_F	F′	J″	e/f″	F''_N	F''_F	F″	Obs(MHz)	Best Fit(MHz)		N constant(MHz)	
											Calc	Obs-Calc	Calc	Obs-Calc
$\frac{3}{2}$	f	$\frac{1}{2}$	1	$\frac{3}{2}$	$\frac{1}{2}$	f	$\frac{1}{2}$	1	$\frac{1}{2}$	12 295.051	12 295.047	0.004	12 294.336	0.715
$\frac{3}{2}$	f	$\frac{1}{2}$	1	$\frac{1}{2}$	$\frac{1}{2}$	f	$\frac{1}{2}$	1	$\frac{1}{2}$	12 294.629	12 294.637	0.008	12 293.541	1.088
$\frac{3}{2}$	f	$\frac{1}{2}$	1	$\frac{3}{2}$	$\frac{1}{2}$	f	$\frac{1}{2}$	0	$\frac{1}{2}$	12 292.648	12 292.640	0.008	12 291.381	1.267
$\frac{3}{2}$	f	$\frac{1}{2}$	0	$\frac{1}{2}$	$\frac{1}{2}$	f	$\frac{1}{2}$	1	$\frac{3}{2}$	12 292.374	12 292.363	0.011	12 291.172	1.202
$\frac{3}{2}$	f	$\frac{1}{2}$	1	$\frac{1}{2}$	$\frac{1}{2}$	f	$\frac{1}{2}$	0	$\frac{1}{2}$	12 292.221	12 292.231	0.010	12 290.586	1.635
$\frac{3}{2}$	f	$\frac{1}{2}$	0	$\frac{1}{2}$	$\frac{1}{2}$	f	$\frac{1}{2}$	1	$\frac{1}{2}$	12 290.558	12 290.570	0.012	12 288.784	1.774
$\frac{3}{2}$	f	$\frac{1}{2}$	0	$\frac{1}{2}$	$\frac{1}{2}$	f	$\frac{1}{2}$	0	$\frac{1}{2}$	12 288.156	12 288.163	0.007	12 285.828	2.328
$\frac{3}{2}$	f	$\frac{5}{2}$	2	$\frac{3}{2}$	$\frac{1}{2}$	f	$\frac{3}{2}$	1	$\frac{1}{2}$	12 289.399	12 289.411	0.012	12 291.592	-2.193
$\frac{3}{2}$	f	$\frac{5}{2}$	3	$\frac{5}{2}$	$\frac{1}{2}$	f	$\frac{3}{2}$	2	$\frac{3}{2}$	12 288.189	12 288.215	0.026	12 290.060	-1.871
$\frac{3}{2}$	f	$\frac{5}{2}$	2	$\frac{5}{2}$	$\frac{1}{2}$	f	$\frac{3}{2}$	1	$\frac{3}{2}$	12 286.381	12 286.390	0.009	12 288.557	-2.176
$\frac{3}{2}$	f	$\frac{5}{2}$	2	$\frac{3}{2}$	$\frac{1}{2}$	f	$\frac{3}{2}$	1	$\frac{3}{2}$	12 285.651	12 285.633	0.018	12 286.878	-1.227
$\frac{3}{2}$	f	$\frac{5}{2}$	3	$\frac{7}{2}$	$\frac{1}{2}$	f	$\frac{3}{2}$	2	$\frac{5}{2}$	12 285.551	12 285.510	0.041	12 287.470	-1.919
$\frac{3}{2}$	f	$\frac{5}{2}$	3	$\frac{5}{2}$	$\frac{1}{2}$	f	$\frac{3}{2}$	2	$\frac{5}{2}$	12 284.774	12 284.769	0.005	12 285.833	-1.059
$\frac{3}{2}$	f	$\frac{5}{2}$	2	$\frac{5}{2}$	$\frac{1}{2}$	f	$\frac{3}{2}$	2	$\frac{3}{2}$	12 283.967	12 283.984	0.017	12 285.680	-1.713
$\frac{3}{2}$	f	$\frac{5}{2}$	2	$\frac{3}{2}$	$\frac{1}{2}$	f	$\frac{3}{2}$	2	$\frac{3}{2}$	12 283.238	12 283.227	0.011	12 284.001	-0.763
$\frac{3}{2}$	f	$\frac{5}{2}$	2	$\frac{5}{2}$	$\frac{1}{2}$	f	$\frac{3}{2}$	2	$\frac{5}{2}$	12 280.552	12 280.538	0.014	12 281.453	-0.901
$\frac{3}{2}$	f	$\frac{5}{2}$	2	$\frac{3}{2}$	$\frac{1}{2}$	f	$\frac{3}{2}$	2	$\frac{5}{2}$	12 279.822	12 279.781	0.041	12 279.774	0.048
$\frac{3}{2}$	f	$\frac{3}{2}$	2	$\frac{3}{2}$	$\frac{1}{2}$	f	$\frac{3}{2}$	1	$\frac{1}{2}$	12 267.454	12 267.483	0.029	12 269.025	-1.571
$\frac{3}{2}$	f	$\frac{3}{2}$	1	$\frac{3}{2}$	$\frac{1}{2}$	f	$\frac{3}{2}$	1	$\frac{1}{2}$	12 264.400	12 264.428	0.028	12 265.968	-1.568
$\frac{3}{2}$	f	$\frac{3}{2}$	2	$\frac{5}{2}$	$\frac{1}{2}$	f	$\frac{3}{2}$	1	$\frac{3}{2}$	12 264.283	12 264.263	0.020	12 265.513	-1.230
$\frac{3}{2}$	f	$\frac{3}{2}$	1	$\frac{1}{2}$	$\frac{1}{2}$	f	$\frac{3}{2}$	1	$\frac{1}{2}$	12 263.716	12 263.765	0.049	12 264.483	-0.767
$\frac{3}{2}$	f	$\frac{3}{2}$	2	$\frac{3}{2}$	$\frac{1}{2}$	f	$\frac{3}{2}$	1	$\frac{3}{2}$	12 263.702	12 263.706	0.004	12 264.312	-0.610
$\frac{3}{2}$	f	$\frac{3}{2}$	2	$\frac{5}{2}$	$\frac{1}{2}$	f	$\frac{3}{2}$	2	$\frac{3}{2}$	12 261.879	12 261.857	0.022	12 262.636	-0.757
$\frac{3}{2}$	f	$\frac{3}{2}$	2	$\frac{3}{2}$	$\frac{1}{2}$	f	$\frac{3}{2}$	2	$\frac{3}{2}$	12 261.298	12 261.300	0.002	12 261.435	-0.137
$\frac{3}{2}$	f	$\frac{3}{2}$	1	$\frac{1}{2}$	$\frac{1}{2}$	f	$\frac{3}{2}$	1	$\frac{3}{2}$	12 259.969	12 259.987	0.018	12 259.769	0.200

J′	e/f′	F'_N	F'_F	F′	J″	e/f″	F''_N	F''_F	F″	Obs(MHz)	Best Fit(MHz)		N constant(MHz)	
											Calc	Obs-Calc	Calc	Obs-Calc
$\frac{3}{2}$	f	$\frac{3}{2}$	2	$\frac{5}{2}$	$\frac{1}{2}$	f	$\frac{3}{2}$	2	$\frac{5}{2}$	12 258.455	12 258.411	0.044	12 258.409	0.046
$\frac{3}{2}$	f	$\frac{3}{2}$	1	$\frac{3}{2}$	$\frac{1}{2}$	f	$\frac{3}{2}$	2	$\frac{3}{2}$	12 258.246	12 258.244	0.002	12 258.377	-0.131
$\frac{3}{2}$	f	$\frac{3}{2}$	2	$\frac{3}{2}$	$\frac{1}{2}$	f	$\frac{3}{2}$	2	$\frac{5}{2}$	12 257.874	12 257.854	0.020	12 257.208	0.666
$\frac{3}{2}$	f	$\frac{3}{2}$	1	$\frac{1}{2}$	$\frac{1}{2}$	f	$\frac{3}{2}$	2	$\frac{3}{2}$	12 257.555	12 257.581	0.026	12 256.892	0.663
$\frac{3}{2}$	f	$\frac{3}{2}$	1	$\frac{3}{2}$	$\frac{1}{2}$	f	$\frac{3}{2}$	2	$\frac{5}{2}$	12 254.831	12 254.798	0.033	12 254.150	0.681
$\frac{3}{2}$	f	$\frac{1}{2}$	1	$\frac{3}{2}$	$\frac{1}{2}$	f	$\frac{3}{2}$	1	$\frac{1}{2}$	12 253.020	12 253.034	0.014	12 253.998	-0.978
$\frac{3}{2}$	f	$\frac{1}{2}$	1	$\frac{1}{2}$	$\frac{1}{2}$	f	$\frac{3}{2}$	1	$\frac{1}{2}$	12 252.598	12 252.625	0.027	12 253.203	-0.605
$\frac{3}{2}$	f	$\frac{1}{2}$	1	$\frac{3}{2}$	$\frac{1}{2}$	f	$\frac{3}{2}$	1	$\frac{3}{2}$	12 249.271	12 249.257	0.014	12 249.284	-0.013
$\frac{3}{2}$	f	$\frac{1}{2}$	0	$\frac{1}{2}$	$\frac{1}{2}$	f	$\frac{3}{2}$	1	$\frac{1}{2}$	12 248.527	12 248.558	0.031	12 248.446	0.081
$\frac{3}{2}$	f	$\frac{1}{2}$	1	$\frac{3}{2}$	$\frac{1}{2}$	f	$\frac{3}{2}$	2	$\frac{3}{2}$	12 246.858	12 246.851	0.007	12 246.407	0.451
$\frac{3}{2}$	f	$\frac{1}{2}$	1	$\frac{1}{2}$	$\frac{1}{2}$	f	$\frac{3}{2}$	2	$\frac{3}{2}$	12 246.431	12 246.442	0.011	12 245.613	0.818
$\frac{3}{2}$	f	$\frac{1}{2}$	0	$\frac{1}{2}$	$\frac{1}{2}$	f	$\frac{3}{2}$	1	$\frac{3}{2}$	12 244.779	12 244.780	0.001	12 243.732	1.047
$\frac{3}{2}$	f	$\frac{1}{2}$	1	$\frac{3}{2}$	$\frac{1}{2}$	f	$\frac{3}{2}$	2	$\frac{5}{2}$	12 243.440	12 243.405	0.035	12 242.181	1.259
$\frac{5}{2}$	f	$\frac{5}{2}$	3	$\frac{5}{2}$	$\frac{3}{2}$	f	$\frac{3}{2}$	2	$\frac{3}{2}$	18 943.932	18 943.962	0.030	18 944.646	-0.714
$\frac{5}{2}$	f	$\frac{3}{2}$	2	$\frac{3}{2}$	$\frac{3}{2}$	f	$\frac{1}{2}$	1	$\frac{1}{2}$	18 943.743	18 943.749	0.006	18 943.606	0.137
$\frac{5}{2}$	f	$\frac{5}{2}$	2	$\frac{3}{2}$	$\frac{3}{2}$	f	$\frac{3}{2}$	1	$\frac{1}{2}$	18 943.548	18 943.552	0.004	18 944.259	-0.711
$\frac{5}{2}$	f	$\frac{5}{2}$	3	$\frac{5}{2}$	$\frac{3}{2}$	f	$\frac{3}{2}$	2	$\frac{5}{2}$	18 943.357	18 943.405	0.048	18 943.445	-0.088
$\frac{5}{2}$	f	$\frac{5}{2}$	3	$\frac{7}{2}$	$\frac{3}{2}$	f	$\frac{3}{2}$	2	$\frac{5}{2}$	18 943.026	18 943.010	0.016	18 943.880	-0.854
$\frac{5}{2}$	f	$\frac{3}{2}$	2	$\frac{5}{2}$	$\frac{3}{2}$	f	$\frac{1}{2}$	1	$\frac{3}{2}$	18 942.991	18 942.944	0.047	18 943.242	-0.251
$\frac{5}{2}$	f	$\frac{5}{2}$	2	$\frac{5}{2}$	$\frac{3}{2}$	f	$\frac{3}{2}$	1	$\frac{3}{2}$	18 942.457	18 942.480	0.023	18 943.226	-0.769
$\frac{5}{2}$	f	$\frac{7}{2}$	3	$\frac{5}{2}$	$\frac{3}{2}$	f	$\frac{5}{2}$	2	$\frac{3}{2}$	18 940.813	18 940.844	0.031	18 942.606	-1.793
$\frac{5}{2}$	f	$\frac{7}{2}$	4	$\frac{7}{2}$	$\frac{3}{2}$	f	$\frac{5}{2}$	3	$\frac{5}{2}$	18 940.453	18 940.461	0.008	18 942.031	-1.578
$\frac{5}{2}$	f	$\frac{7}{2}$	3	$\frac{5}{2}$	$\frac{3}{2}$	f	$\frac{5}{2}$	2	$\frac{5}{2}$	18 940.088	18 940.087	0.001	18 940.927	-0.839
$\frac{5}{2}$	f	$\frac{7}{2}$	3	$\frac{7}{2}$	$\frac{3}{2}$	f	$\frac{5}{2}$	2	$\frac{5}{2}$	18 939.650	18 939.653	0.003	18 941.410	-1.760
$\frac{5}{2}$	f	$\frac{7}{2}$	4	$\frac{9}{2}$	$\frac{3}{2}$	f	$\frac{5}{2}$	3	$\frac{7}{2}$	18 939.320	18 939.288	0.032	18 940.873	-1.553

J′	e/f′	F'_N	F'_F	F′	J″	e/f″	F''_N	F''_F	F″	Obs(MHz)	Best Fit(MHz)		N constant(MHz)	
											Calc	Obs-Calc	Calc	Obs-Calc
$\frac{5}{2}$	f	$\frac{3}{2}$	1	$\frac{3}{2}$	$\frac{3}{2}$	f	$\frac{1}{2}$	1	$\frac{1}{2}$	18 938.950	18 938.935	0.015	18 938.751	0.199
$\frac{5}{2}$	f	$\frac{5}{2}$	2	$\frac{5}{2}$	$\frac{3}{2}$	f	$\frac{3}{2}$	2	$\frac{5}{2}$	18 938.841	18 938.868	0.027	18 938.967	-0.126
$\frac{5}{2}$	f	$\frac{3}{2}$	1	$\frac{3}{2}$	$\frac{3}{2}$	f	$\frac{1}{2}$	1	$\frac{3}{2}$	18 938.513	18 938.525	0.012	18 937.956	0.557
$\frac{5}{2}$	f	$\frac{7}{2}$	3	$\frac{5}{2}$	$\frac{3}{2}$	f	$\frac{5}{2}$	3	$\frac{5}{2}$	18 935.871	18 935.857	0.014	18 936.547	-0.676
$\frac{5}{2}$	f	$\frac{7}{2}$	3	$\frac{7}{2}$	$\frac{3}{2}$	f	$\frac{5}{2}$	3	$\frac{7}{2}$	18 934.649	18 934.681	0.032	18 935.393	-0.744
$\frac{5}{2}$	f	$\frac{3}{2}$	2	$\frac{5}{2}$	$\frac{3}{2}$	f	$\frac{3}{2}$	1	$\frac{3}{2}$	18 931.606	18 931.551	0.055	18 931.272	0.334
$\frac{5}{2}$	f	$\frac{3}{2}$	2	$\frac{3}{2}$	$\frac{3}{2}$	f	$\frac{3}{2}$	2	$\frac{3}{2}$	18 928.886	18 928.891	0.005	18 927.784	1.102
$\frac{5}{2}$	f	$\frac{3}{2}$	2	$\frac{3}{2}$	$\frac{3}{2}$	f	$\frac{3}{2}$	2	$\frac{5}{2}$	18 928.307	18 928.334	0.027	18 926.583	1.724
$\frac{5}{2}$	f	$\frac{3}{2}$	1	$\frac{1}{2}$	$\frac{3}{2}$	f	$\frac{3}{2}$	1	$\frac{1}{2}$	18 928.238	18 928.201	0.037	18 927.027	1.211
$\frac{5}{2}$	f	$\frac{3}{2}$	2	$\frac{5}{2}$	$\frac{3}{2}$	f	$\frac{3}{2}$	2	$\frac{5}{2}$	18 927.982	18 927.938	0.044	18 927.014	0.968
$\frac{5}{2}$	f	$\frac{3}{2}$	1	$\frac{3}{2}$	$\frac{3}{2}$	f	$\frac{3}{2}$	1	$\frac{3}{2}$	18 927.137	18 927.132	0.005	18 925.986	1.151
$\frac{5}{2}$	f	$\frac{3}{2}$	1	$\frac{3}{2}$	$\frac{3}{2}$	f	$\frac{3}{2}$	2	$\frac{5}{2}$	18 923.513	18 923.519	0.006	18 921.727	1.786
$\frac{5}{2}$	f	$\frac{5}{2}$	3	$\frac{5}{2}$	$\frac{3}{2}$	f	$\frac{5}{2}$	2	$\frac{3}{2}$	18 921.984	18 922.034	0.050	18 922.080	-0.096
$\frac{5}{2}$	f	$\frac{5}{2}$	3	$\frac{7}{2}$	$\frac{3}{2}$	f	$\frac{5}{2}$	2	$\frac{5}{2}$	18 920.927	18 920.882	0.045	18 920.836	0.091
$\frac{5}{2}$	f	$\frac{5}{2}$	2	$\frac{3}{2}$	$\frac{3}{2}$	f	$\frac{5}{2}$	2	$\frac{3}{2}$	18 917.868	18 917.905	0.037	18 917.150	0.718
$\frac{5}{2}$	f	$\frac{5}{2}$	3	$\frac{5}{2}$	$\frac{3}{2}$	f	$\frac{5}{2}$	3	$\frac{5}{2}$	18 917.034	18 917.046	0.012	18 916.021	1.013
$\frac{5}{2}$	f	$\frac{5}{2}$	2	$\frac{5}{2}$	$\frac{3}{2}$	f	$\frac{5}{2}$	2	$\frac{5}{2}$	18 916.744	18 916.740	0.004	18 915.923	0.821
$\frac{5}{2}$	f	$\frac{5}{2}$	3	$\frac{7}{2}$	$\frac{3}{2}$	f	$\frac{5}{2}$	3	$\frac{7}{2}$	18 915.934	18 915.910	0.024	18 914.818	1.116
$\frac{5}{2}$	f	$\frac{5}{2}$	2	$\frac{5}{2}$	$\frac{3}{2}$	f	$\frac{5}{2}$	3	$\frac{7}{2}$	18 911.743	18 911.768	0.025	18 909.906	1.837

Table D.1: The fitted frequencies of the f-states for the NO-HF complex at the position of minimum standard deviation. The frequencies are in MHz. The first set of calculated frequencies are for the best fit possible with all parameters optimised to give an angle of 49.0°. The second set are for a fit with the nitrogen constants fixed at their monomer values which is optimum at an angle of 36.0°

D.2 e-states

J′	e/f′	F′	index′	J″	e/f″	F″	index″	Obs(MHz)	Best Fit(MHz)		N constant(MHz)	
									Calc	Obs-Calc	Calc	Obs-Calc
$\frac{3}{2}$	e	$\frac{5}{2}$	(3)	$\frac{1}{2}$	e	$\frac{3}{2}$	(1)	7 716.527	7 716.526	0.001	7 717.392	-0.865
$\frac{3}{2}$	e	$\frac{5}{2}$	(3)	$\frac{1}{2}$	e	$\frac{5}{2}$		7 718.265	7 718.252	0.013	7 719.567	-1.302
$\frac{3}{2}$	e	$\frac{5}{2}$	(3)	$\frac{1}{2}$	e	$\frac{3}{2}$	(2)	7 720.145	7 720.154	0.009	7 718.744	1.401
$\frac{3}{2}$	e	$\frac{3}{2}$	(4)	$\frac{1}{2}$	e	$\frac{3}{2}$	(1)	7 718.729	7 718.706	0.023	7 720.019	-1.290
$\frac{3}{2}$	e	$\frac{3}{2}$	(4)	$\frac{1}{2}$	e	$\frac{1}{2}$	(1)	7 720.606	7 720.596	0.010	7 719.081	1.525
$\frac{3}{2}$	e	$\frac{3}{2}$	(4)	$\frac{1}{2}$	e	$\frac{3}{2}$	(2)	7 722.349	7 722.334	0.015	7 721.371	0.978
$\frac{3}{2}$	e	$\frac{3}{2}$	(4)	$\frac{1}{2}$	e	$\frac{1}{2}$	(2)	7 723.481	7 723.479	0.002	7 720.557	2.924
$\frac{3}{2}$	e	$\frac{3}{2}$	(3)	$\frac{1}{2}$	e	$\frac{5}{2}$		7 723.204	7 723.171	0.033	7 726.008	-2.804
$\frac{3}{2}$	e	$\frac{3}{2}$	(3)	$\frac{1}{2}$	e	$\frac{1}{2}$	(1)	7 723.344	7 723.336	0.008	7 722.895	0.449
$\frac{3}{2}$	e	$\frac{3}{2}$	(3)	$\frac{1}{2}$	e	$\frac{1}{2}$	(2)	7 726.216	7 726.219	0.003	7 724.371	1.845
$\frac{3}{2}$	e	$\frac{3}{2}$	(3)	$\frac{1}{2}$	e	$\frac{3}{2}$	(3)	7 738.041	7 738.025	0.016	7 737.982	0.059
$\frac{3}{2}$	e	$\frac{1}{2}$	(3)	$\frac{1}{2}$	e	$\frac{1}{2}$	(3)	7 738.783	7 738.819	0.036	7 738.858	-0.075
$\frac{3}{2}$	e	$\frac{7}{2}$		$\frac{1}{2}$	e	$\frac{5}{2}$		7 725.210	7 725.176	0.034	7 725.421	-0.211
$\frac{3}{2}$	e	$\frac{1}{2}$	(2)	$\frac{1}{2}$	e	$\frac{1}{2}$	(1)	7 727.368	7 727.383	0.015	7 728.148	-0.780
$\frac{3}{2}$	e	$\frac{1}{2}$	(2)	$\frac{1}{2}$	e	$\frac{3}{2}$	(2)	7 729.105	7 729.121	0.016	7 730.437	-1.332
$\frac{3}{2}$	e	$\frac{1}{2}$	(2)	$\frac{1}{2}$	e	$\frac{3}{2}$	(3)	7 742.067	7 742.072	0.005	7 743.235	-1.168
$\frac{3}{2}$	e	$\frac{5}{2}$	(2)	$\frac{1}{2}$	e	$\frac{3}{2}$	(1)	7 725.852	7 725.833	0.019	7 726.087	-0.235
$\frac{3}{2}$	e	$\frac{5}{2}$	(2)	$\frac{1}{2}$	e	$\frac{5}{2}$		7 727.582	7 727.559	0.023	7 728.262	-0.680
$\frac{3}{2}$	e	$\frac{5}{2}$	(2)	$\frac{1}{2}$	e	$\frac{3}{2}$	(2)	7 729.471	7 729.461	0.010	7 727.438	2.033
$\frac{3}{2}$	e	$\frac{5}{2}$	(1)	$\frac{1}{2}$	e	$\frac{3}{2}$	(1)	7 727.721	7 727.709	0.012	7 728.956	-1.235
$\frac{3}{2}$	e	$\frac{5}{2}$	(1)	$\frac{1}{2}$	e	$\frac{5}{2}$		7 729.455	7 729.435	0.020	7 731.131	-1.676
$\frac{3}{2}$	e	$\frac{5}{2}$	(1)	$\frac{1}{2}$	e	$\frac{3}{2}$	(2)	7 731.339	7 731.337	0.002	7 730.307	0.1032
$\frac{3}{2}$	e	$\frac{3}{2}$	(2)	$\frac{1}{2}$	e	$\frac{3}{2}$	(1)	7 729.086	7 729.060	0.026	7 730.794	-1.708

J′	e/f′	F′	index′	J″	e/f″	F″	index″	Obs(MHz)	Best Fit(MHz)		N constant(MHz)	
									Calc	Obs-Calc	Calc	Obs-Calc
$\frac{3}{2}$	e	$\frac{3}{2}$	(2)	$\frac{1}{2}$	e	$\frac{1}{2}$	(1)	7 730.958	7 730.950	0.008	7 729.856	1.102
$\frac{3}{2}$	e	$\frac{3}{2}$	(2)	$\frac{1}{2}$	e	$\frac{1}{2}$	(2)	7 733.830	7 733.834	0.004	7 731.332	2.498
$\frac{3}{2}$	e	$\frac{3}{2}$	(1)	$\frac{1}{2}$	e	$\frac{3}{2}$	(1)	7 731.464	7 731.466	0.002	7 733.961	-2.497
$\frac{3}{2}$	e	$\frac{3}{2}$	(1)	$\frac{1}{2}$	e	$\frac{5}{2}$		7 733.210	7 733.192	0.018	7 736.136	-2.926
$\frac{3}{2}$	e	$\frac{3}{2}$	(1)	$\frac{1}{2}$	e	$\frac{1}{2}$	(1)	7 733.355	7 733.357	0.002	7 733.023	0.332
$\frac{3}{2}$	e	$\frac{3}{2}$	(1)	$\frac{1}{2}$	e	$\frac{3}{2}$	(2)	7 735.092	7 735.095	0.003	7 735.313	-0.221
$\frac{3}{2}$	e	$\frac{3}{2}$	(1)	$\frac{1}{2}$	e	e$\frac{1}{2}$	(2)	7 736.224	7 736.240	0.016	7 734.500	1.724
$\frac{3}{2}$	e	$\frac{3}{2}$	(1)	$\frac{1}{2}$	e	$\frac{3}{2}$	(3)	7 748.049	7 748.046	0.003	7 748.111	-0.062
$\frac{3}{2}$	e	$\frac{1}{2}$	(1)	$\frac{1}{2}$	e	$\frac{3}{2}$	(1)	7 733.553	7 733.556	0.003	7 736.326	-2.773
$\frac{3}{2}$	e	$\frac{1}{2}$	(1)	$\frac{1}{2}$	e	$\frac{1}{2}$	(1)	7 735.425	7 735.446	0.021	7 735.388	0.037
$\frac{3}{2}$	e	$\frac{1}{2}$	(1)	$\frac{1}{2}$	e	$\frac{3}{2}$	(2)	7 737.171	7 737.184	0.013	7 737.677	-0.506
$\frac{3}{2}$	e	$\frac{1}{2}$	(1)	$\frac{1}{2}$	e	$\frac{1}{2}$	(2)	7 738.301	7 738.329	0.028	7 736.864	1.437
$\frac{3}{2}$	e	$\frac{1}{2}$	(1)	$\frac{1}{2}$	e	$\frac{3}{2}$	(3)	7 750.133	7 750.136	0.003	7 750.475	-0.342
$\frac{5}{2}$	e	$\frac{3}{2}$	(2)	$\frac{3}{2}$	e	$\frac{5}{2}$	(3)	14 426.355	14 426.374	0.019	14 427.837	-1.482
$\frac{5}{2}$	e	$\frac{5}{2}$	(3)	$\frac{3}{2}$	e	$\frac{5}{2}$	(3)	14 421.548	14 421.546	0.002	14 422.336	-0.788
$\frac{5}{2}$	e	$\frac{7}{2}$	(3)	$\frac{3}{2}$	e	$\frac{5}{2}$	(3)	14 416.455	14 416.466	0.011	14 416.506	-0.051
$\frac{5}{2}$	e	$\frac{3}{2}$	(2)	$\frac{3}{2}$	e	$\frac{3}{2}$	(4)	14 424.147	14 424.194	0.047	14 425.210	-1.063
$\frac{5}{2}$	e	$\frac{5}{2}$	(4)	$\frac{3}{2}$	e	$\frac{3}{2}$	(4)	14 417.272	14 417.276	0.004	14 417.299	-0.027
$\frac{5}{2}$	e	$\frac{1}{2}$		$\frac{3}{2}$	e	$\frac{3}{2}$	(3)	14 424.253	14 424.263	0.010	14 424.594	-0.341
$\frac{5}{2}$	e	$\frac{3}{2}$	(2)	$\frac{3}{2}$	e	$\frac{3}{2}$	(3)	14 421.414	14 421.455	0.041	14 421.396	0.018
$\frac{5}{2}$	e	$\frac{3}{2}$	(3)	$\frac{3}{2}$	e	$\frac{3}{2}$	(3)	14 418.806	14 418.819	0.013	14 418.438	0.368
$\frac{5}{2}$	e	$\frac{5}{2}$	(3)	$\frac{3}{2}$	e	$\frac{3}{2}$	(3)	14 416.609	14 416.627	0.018	14 415.895	0.714
$\frac{5}{2}$	e	$\frac{3}{2}$	(2)	$\frac{3}{2}$	e	$\frac{1}{2}$	(3)	14 420.936	14 420.936	0.000	14 420.379	0.557
$\frac{5}{2}$	e	$\frac{3}{2}$	(3)	$\frac{3}{2}$	e	$\frac{1}{2}$	(3)	14 418.312	14 418.300	0.012	14 417.421	0.891
$\frac{5}{2}$	e	$\frac{5}{2}$	(1)	$\frac{3}{2}$	e	$\frac{7}{2}$		14 424.669	14 424.667	0.002	14 426.194	-1.525

J′	e/f′	F′	index′	J″	e/f″	F″	index″	Obs(MHz)	Best Fit(MHz)		N constant(MHz)	
									Calc	Obs-Calc	Calc	Obs-Calc
$\frac{5}{2}$	e	$\frac{7}{2}$	(1)	$\frac{3}{2}$	e	$\frac{7}{2}$		14 419.886	14 419.873	0.013	14 420.730	-0.844
$\frac{5}{2}$	e	$\frac{9}{2}$		$\frac{3}{2}$	e	$\frac{7}{2}$		14 415.114	14 415.079	0.035	14 415.178	-0.064
$\frac{5}{2}$	e	$\frac{7}{2}$	(2)	$\frac{3}{2}$	e	$\frac{7}{2}$		14 409.510	14 409.542	0.032	14 410.653	-1.143
$\frac{5}{2}$	e	$\frac{1}{2}$		$\frac{3}{2}$	e	$\frac{1}{2}$	(2)	14 420.222	14 420.216	0.006	14 419.341	0.881
$\frac{5}{2}$	e	$\frac{3}{2}$	(2)	$\frac{3}{2}$	e	$\frac{1}{2}$	(2)	14 417.388	14 417.408	0.020	14 416.143	1.245
$\frac{5}{2}$	e	$\frac{5}{2}$	(2)	$\frac{3}{2}$	e	$\frac{5}{2}$	(2)	14 420.011	14 419.998	0.013	14 420.735	-0.724
$\frac{5}{2}$	e	$\frac{7}{2}$	(2)	$\frac{3}{2}$	e	$\frac{5}{2}$	(2)	14 415.805	14 415.783	0.022	14 415.850	-0.045
$\frac{5}{2}$	e	$\frac{5}{2}$	(4)	$\frac{3}{2}$	e	$\frac{5}{2}$	(2)	14 410.152	14 410.149	0.003	14 411.231	-1.079
$\frac{5}{2}$	e	$\frac{3}{2}$	(1)	$\frac{3}{2}$	e	$\frac{5}{2}$	(1)	14 423.427	14 423.434	0.007	14 423.891	-0.464
$\frac{5}{2}$	e	$\frac{5}{2}$	(1)	$\frac{3}{2}$	e	$\frac{5}{2}$	(1)	14 420.415	14 420.408	0.007	14 420.484	-0.069
$\frac{5}{2}$	e	$\frac{5}{2}$	(2)	$\frac{3}{2}$	e	$\frac{5}{2}$	(1)	14 418.145	14 418.122	0.023	14 417.866	0.279
$\frac{5}{2}$	e	$\frac{7}{2}$	(1)	$\frac{3}{2}$	e	$\frac{5}{2}$	(1)	14 415.638	14 415.614	0.024	14 415.019	0.619
$\frac{5}{2}$	e	$\frac{7}{2}$	(2)	$\frac{3}{2}$	e	$\frac{5}{2}$	(1)	14 413.935	14 413.907	0.028	14 412.981	0.954
$\frac{5}{2}$	e	$\frac{5}{2}$	(3)	$\frac{3}{2}$	e	$\frac{5}{2}$	(1)	14 410.354	14 410.363	0.009	14 410.772	-0.418
$\frac{5}{2}$	e	$\frac{7}{2}$	(3)	$\frac{3}{2}$	e	$\frac{5}{2}$	(1)	14 405.265	14 405.283	0.018	14 404.942	0.323
$\frac{5}{2}$	e	$\frac{3}{2}$	(1)	$\frac{3}{2}$	e	$\frac{3}{2}$	(2)	14 422.074	14 422.083	0.009	14 422.053	0.021
$\frac{5}{2}$	e	$\frac{5}{2}$	(1)	$\frac{3}{2}$	e	$\frac{3}{2}$	(2)	14 419.057	14 419.057	0.000	14 418.646	0.411
$\frac{5}{2}$	e	$\frac{5}{2}$	(2)	$\frac{3}{2}$	e	$\frac{3}{2}$	(2)	14 416.778	14 416.771	0.007	14 416.028	0.750
$\frac{5}{2}$	e	$\frac{3}{2}$	(3)	$\frac{3}{2}$	e	$\frac{3}{2}$	(2)	14 411.177	14 411.204	0.027	14 411.477	-0.300
$\frac{5}{2}$	e	$\frac{3}{2}$	(1)	$\frac{3}{2}$	e	$\frac{3}{2}$	(1)	14 419.679	14 419.677	0.002	14 418.885	0.794
$\frac{5}{2}$	e	$\frac{5}{2}$	(1)	$\frac{3}{2}$	e	$\frac{3}{2}$	(1)	14 416.667	14 416.651	0.016	14 415.479	1.188
$\frac{5}{2}$	e	$\frac{5}{2}$	(2)	$\frac{3}{2}$	e	$\frac{3}{2}$	(1)	14 414.388	14 414.365	0.023	14 412.860	1.528
$\frac{5}{2}$	e	$\frac{1}{2}$		$\frac{3}{2}$	e	$\frac{3}{2}$	(1)	14 414.248	14 414.242	0.006	14 414.465	-0.217
$\frac{5}{2}$	e	$\frac{3}{2}$	(2)	$\frac{3}{2}$	e	$\frac{3}{2}$	(1)	14 411.408	14 411.434	0.026	14 411.268	0.140
$\frac{5}{2}$	e	$\frac{5}{2}$	(3)	$\frac{3}{2}$	e	$\frac{3}{2}$	(1)	14 406.600	14 406.606	0.006	14 405.767	0.833

J′	e/f′	F′	index′	J″	e/f″	F″	index″	Obs(MHz)	Best Fit(MHz)		N constant(MHz)	
									Calc	Obs-Calc	Calc	Obs-Calc
$\frac{5}{2}$	e	$\frac{3}{2}$	(1)	$\frac{3}{2}$	e	$\frac{1}{2}$	(1)	14 417.594	14 417.588	0.006	14 416.521	1.073
$\frac{5}{2}$	e	$\frac{1}{2}$		$\frac{3}{2}$	e	$\frac{1}{2}$	(1)	14 412.168	14 412.153	0.015	14 412.101	0.067
$\frac{5}{2}$	e	$\frac{3}{2}$	(2)	$\frac{3}{2}$	e	$\frac{1}{2}$	(1)	14 409.326	14 409.345	0.019	14 408.904	0.422

Table D.2: The fitted frequencies of the e-states for the NO-HF complex at the position of miniumum standard deviation. The frequencies are in MHz. The first set of calculated frequencies are for the best fit possible with all parameters optimised to give an angle of 49.0°. The second set are for a fit with the nitrogen constants fixed at their monomer values which is optimum at an angle of 36.9°

D.3 Infrared Spectra

J′	e/f′	J″	e/f″	Obs(MHz)	Best Fit(MHz)		N constant(MHz)		Weight
					Calc	Obs-Calc	Calc	Obs-Calc	
$\frac{3}{2}$	1	$\frac{1}{2}$	2	3 165.800	3 156.253	9.547	3 154.979	10.821	10^{-6}
$\frac{5}{2}$	1	$\frac{1}{2}$	1	22 128.000	22 146.946	18.946	22 146.495	-18.495	10^{-6}
$\frac{7}{2}$	1	$\frac{3}{2}$	1	35 478.600	35 524.711	46.111	35 523.675	-45.075	10^{-6}
$\frac{9}{2}$	1	$\frac{5}{2}$	1	48 888.100	48 910.670	-22.570	48 908.016	-19.916	10^{-6}
$\frac{11}{2}$	1	$\frac{7}{2}$	1	62 311.001	62 302.831	8.170	62 297.251	13.750	10^{-6}
$\frac{13}{2}$	1	$\frac{9}{2}$	1	75 684.402	75 699.528	15.126	75 689.483	-5.081	10^{-6}
$\frac{3}{2}$	2	$\frac{1}{2}$	1	16 867.201	16 861.142	6.059	16 863.110	4.091	10^{-6}
$\frac{5}{2}$	2	$\frac{1}{2}$	2	31 222.500	31 226.459	3.959	31 228.151	-5.651	10^{-6}
$\frac{7}{2}$	2	$\frac{3}{2}$	2	44 548.302	44 516.361	31.941	44 517.485	30.817	10^{-6}
$\frac{9}{2}$	2	$\frac{5}{2}$	2	57 797.298	57 775.006	22.292	57 774.681	22.617	10^{-6}

Table D.3: The extra lines included in the fit derived from the infrared data of Fawzy et al.[1] The frequencies here are constructed from the observed transitions to be compatible with the fitting program and at reduced weight. All frequencies are in MHz.

Appendix E

Ar-OCS

These are transitions of the Ar-OCS complex that were measured as part of the calibration of the 18-26GHz microwave circuit. They do not comprise an essential part of the thesis but can be used to test the high frequency circuit. The results are given as a fit with the Ar-OCS data of Campbell et al.[2, 3]

J′ q	K_a'	K_c'	J″	K_a''	K_c''	Obs. MHz	Calc. MHz	Residuals MHz	Weight	New Line
1	1	0	1	0	1	5559.1580	5559.1561	.00192	1.0	
1	1	0	1	1	1	282.9940	282.9938	.00019	1.0	
1	1	1	0	0	0	8012.9382	8012.9352	.00301	0.8	
2	1	1	1	1	0	5756.0150	5756.0181	-.00313	0.8	
2	1	1	2	0	2	5852.9220	5852.9204	.00160	1.0	
2	1	1	2	1	2	848.8750	848.8749	.00014	1.0	
2	1	2	1	0	1	10466.3023	10466.2993	.00296	0.8	
2	2	0	2	2	1	11.0560	11.0550	.00104	1.0	
2	2	1	3	1	2	7198.7250	7198.7267	-.00172	1.0	

J′ q	K'_a	K'_c	J″	K''_a	K''_c	Obs. MHz	Calc. MHz	Residuals MHz	Weight	New Line
3	0	3	2	0	2	8165.2806	8165.2798	.00077	1.0	
3	1	3	2	0	2	12782.0610	12782.0593	.00174	1.0	*
3	1	2	3	0	3	6313.9390	6313.9403	-.00130	1.0	
3	2	1	2	2	0	8252.0660	8252.0686	-.00256	1.0	
3	2	1	3	2	2	55.1460	55.1453	.00065	1.0	
3	2	1	4	1	4	6801.3700	6801.3692	.00083	1.0	
3	2	2	3	1	3	17103.8632	17103.8658	-.00257	0.8	*
3	2	2	4	1	3	3919.7640	3919.7656	-.00155	1.0	
3	3	0	3	3	1	.2690	.2690	.00002	1.0	
4	0	4	3	0	3	10835.2809	10835.2793	.00157	1.0	
4	1	4	3	0	3	14974.4204	14974.4214	-.00098	1.0	
4	1	3	4	0	4	6965.6000	6965.6003	-.00032	1.0	
4	2	2	3	2	1	11043.8520	11043.8537	-.00173	1.0	
4	2	2	4	1	3	15018.7625	15018.7646	-.00212	1.0	*
4	2	3	4	1	4	17680.6365	17680.6428	-.00633	0.6	*
4	3	1	3	3	0	10963.2870	10963.2902	-.00319	0.8	
4	3	1	4	3	2	1.8810	1.8802	.00081	1.0	
5	0	5	4	0	4	13463.3197	13463.3202	-.00045	1.0	*
5	0	5	4	1	4	9324.1778	9324.1781	-.00031	1.0	
5	1	5	4	0	4	17066.0344	17066.0330	.00144	1.0	*
5	1	5	4	1	4	12926.8908	12926.8909	-.00012	1.0	*
5	1	4	5	0	5	7836.3862	7836.3828	.00338	0.8	
5	1	4	4	1	3	14334.1028	14334.1027	.00014	1.0	*

J′ q	K'_a	K'_c	J″	K''_a	K''_c	Obs.	Calc.	Residuals	Weight	New Line
						MHz	MHz	MHz		
5	2	3	4	2	2	13868.4551	13868.4549	.00020	1.0	*
5	2	3	5	1	4	14553.1189	14553.1169	.00204	1.0	
5	2	4	4	2	3	13652.6995	13652.7002	-.00074	1.0	*
5	2	4	5	1	5	18406.4492	18406.4522	-.00296	0.7	*
5	3	2	4	3	1	13714.7028	13714.7033	-.00046	1.0	*
5	3	2	5	3	3	7.5040	7.5028	.00116	1.0	
5	3	3	4	3	2	13709.0798	13709.0806	-.00081	1.0	*
6	0	6	5	0	5	16043.7319	16043.7321	-.00016	1.0	*
6	0	6	5	1	5	12441.0161	12441.0193	-.00315	0.8	
6	1	5	5	1	4	17163.4215	17163.4227	-.00116	1.0	*
6	1	5	6	0	6	8956.0769	8956.0734	.00348	0.8	
6	1	5	6	1	6	5912.9840	5912.9724	.01156	0.3	
6	1	6	5	0	5	19086.8341	19086.8330	.00106	1.0	*
6	1	6	5	1	5	15484.1203	15484.1202	.00007	1.0	*
6	2	4	5	2	3	16729.2339	16729.2329	.00095	1.0	*
6	2	4	6	1	5	14118.9306	14118.9271	.00345	0.8	
6	2	4	6	2	5	748.7400	748.7353	.00471	0.8	
6	2	5	5	2	4	16360.8327	16360.8324	.00032	1.0	*
6	2	5	6	1	6	19283.1612	19283.1643	-.00310	0.8	*
6	3	3	6	3	4	22.4250	22.4240	.00100	1.0	
6	3	4	7	2	5	6887.3050	6887.3009	.00408	0.8	
7	0	7	6	0	6	18575.7774	18575.7773	.00012	0.7	*
7	0	7	6	1	6	15532.6795	15532.6763	.00320	0.8	*

J′ q	K'_a	K'_c	J″	K''_a	K''_c	Obs. MHz	Calc. MHz	Residuals MHz	Weight	New Line
7	1	6	6	1	5	19969.8895	19969.8902	-.00071	1.0	*
7	1	6	7	0	7	10350.1880	10350.1864	.00164	1.0	
7	1	7	6	1	6	18028.2462	18028.2455	.00074	1.0	*
7	2	5	6	2	4	19624.5679	19624.5668	.00107	1.0	*
7	2	5	7	1	6	13773.6058	13773.6038	.00204	1.0	*
7	2	6	7	1	7	20311.7997	20311.8024	-.00270	1.0	
7	2	6	6	2	5	19056.8848	19056.8836	.00124	1.0	*
7	3	5	6	3	4	19212.9862	19212.9859	.00025	1.0	*
7	3	4	6	3	3	19246.3080	19246.3059	.00207	1.0	*
8	0	8	7	1	7	18568.7876	18568.7895	-.00191	1.0	*
8	1	7	8	0	8	12033.6345	12033.6342	.00026	1.0	*
8	1	8	7	1	7	20558.7628	20558.7605	.00229	0.8	*
9	5	5	10	4	6	21057.9970	21057.9971	-.00012	1.0	*
10	1	9	9	2	8	17829.4325	17829.4328	-.00030	1.0	*
10	2	8	10	1	9	13797.7653	13797.7674	-.00210	1.0	*
11	1	10	11	0	11	18723.0635	18723.0631	.00041	0.7	*

Table E.2: Fitted Microwave Spectrum of the van der Waals complex Ar-OCS

Constant	Value	σ
Rotational Constants (MHz)		
A	6786.4161	(7)
B	1510.0732	(2)
C	1226.7391	(2)
Centrifugal Distortion Coefficients (kHz)		
Dj	9.875	(4)
Dk	235.2	(1)
Djk	57.73	(3)
d1	2.219	(1)
d2	80.63	(4)
Hj	-0.00034	(3)
Hjk	0.0010	(3)
Hkj	-0.073	(3)
Hk	0.138	(3)
h1	-0.000102	(7)

Table E.1: The rotational constants of the Ar-OCS complex.

References

[1] W. M. Fawzy, G. T. Frazer, J. T. Hougen. *J. Chem. Phys*, **93**, 2992, (1990).

[2] J. A. Shea, W. G. Read, E. J. Campbell. *J. Chem. Phys.*, **79**, 2559, (1983).

[3] S. J. Harris, K. C. Jandu, S. E. Novick, W. Klemperer. *J. Chem. Phys.*, **63**, 881, (1975).